CR-66148

NASA Contractor Report No. 66148

# FEASIBILITY STUDY FOR AN X-RAY BACKSCATTER FREE AIR DENSITY SENSOR

By David B. Hakewessell



Prepared under Contract No. NAS1-4349 by

GIANNINI CONTROLS CORPORATION
Control/Nucleonics Division
Duarte, Calif.

for

NATIONAL AERONAUTICS AND SPACE ADMINISTRATION

ABSTRACT

for

FEASIBILITY STUDY FOR AN X-RAY BACKSCATTER

FREE AIR DENSITY SENSOR

by

David B. Hakewessell

Gamma-ray scattering techniques for measuring atmospheric density from a high velocity vehicle have been experimentally demonstrated to 60 km altitude. Excessive background levels were found to limit the accuracy at altitudes above 60 km. The source of this high background is believed to be the result of multiple scatter of gamma-rays in the vehicle skin. Modified gamma-ray sources are recommended which will reduce this effect and improve accuracy at high altitudes.

TABLE OF CONTENTS

TABLE OF CONTENTS - Continued

# FEASIBILITY STUDY FOR AN X-RAY BACKSCATTER FREE AIR DENSITY SENSOR

By David B. Hakewessell

## SUMMARY

The feasibility of measuring atmospheric density at high altitudes from vehicles traveling at high velocities using an X-ray (or gamma ray) backscatter technique has been demonstrated. Hardware has been developed and air density soundings have been made from the Nike-Apache boost vehicle. The results of these soundings are in agreement with theories developed relating the gamma ray scattering principles to the air density measurement.

The high altitude capability of the air density measurement system is presently limited by a high background. This high background level is the result of multiple skin scatter of high energy gamma rays originating at the gamma ray source. This is a unique characteristic of the particular source material used and not a limitation of the gamma ray backscatter technique. Gamma and X-ray sources are available that do not exhibit this characteristic and may eventually prove the system capability to measure air density at 90 km altitude.

# INTRODUCTION

The measurement of atmospheric density at high altitude from vehicles traveling at high velocities is useful in several applications. These include measurement for determining the aerodynamic properties of high performance flight vehicles, and measurement of unknown atmospheres of planets other than Earth from space probes. A sensing technique, based on the principle that the intensity of backscattered gamma radiation is related to the density of the free air being measured, shows much promise of providing an accurate measure for such applications.

Figure 1 illustrates this measurement principle. Gamma radiation, emanating from a radioactive isotope source located in the vehicle, passes through the vehicle skin into the atmosphere whose density is to be measured. A portion of the gamma photons are scattered by the atmosphere at a rate proportional to the number of photons emitted and the density of the scattering media. A portion of these scattered photons reaches the detector and are sensed. The rate at which these photons are sensed is thus proportional to the atmospheric density.

Several programs have been conducted in recent years which have provided much information substantiating the feasibility of measuring air density using this gamma backscatter technique. These include a paper study of scattering and absorption techniques for air density measurement (ref. 1), an X-ray air scatter demonstration in a large altitude chamber (ref. 2),

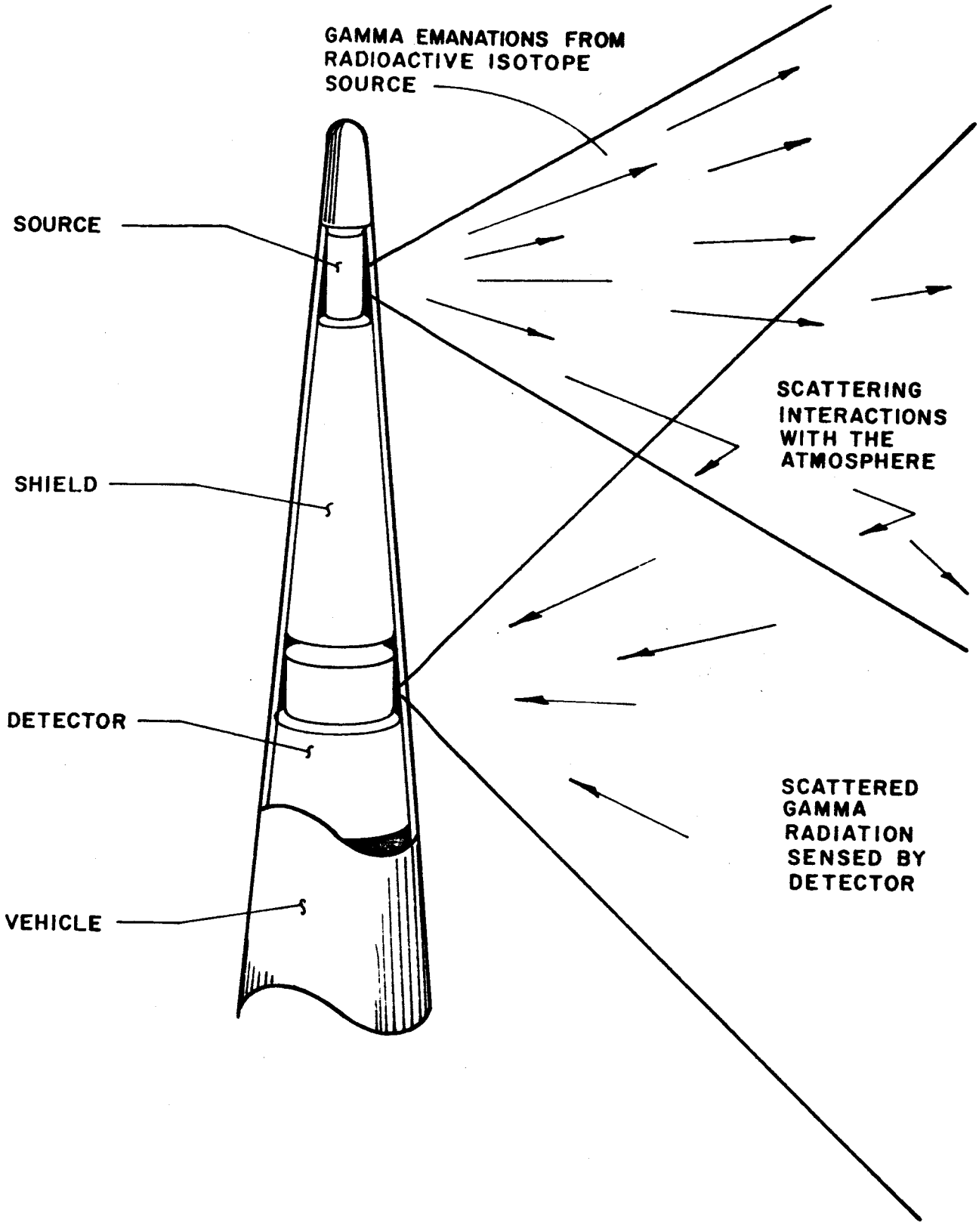


Figure 1 - Gamma Backscatter Air Density Sensing Technique Illustrated

three balloon experiments in which gamma backscatter techniques were employed to measure air density from ground level to 33 km altitude (data not yet published), and the forerunner of the present work in which a measurement of air density was made from the Nike-Apache vehicle over an altitude range of 20 to 70 km. The results of this first gamma backscatter air density measurement experiment from the Nike-Apache are shown in figure 2, giving the measured density as a function of altitude. The significant conclusion reached from this experiment was that the measurement technique is feasible using practical hardware and radioisotope sources of reasonable strength. It was also learned that the high altitude measurement capability of the flight apparatus was limited by a higher than anticipated level of background radiation.

The purpose of the present program was to extend the altitude range of the sensing apparatus to higher altitude. This was to be accomplished by increasing the strength of the gamma radiation source and providing a means to measure the ambient background radiation level.

The measurement system was designed, fabricated, and flight-tested jointly by Giannini Controls Corporation and NASA-Langley Research Center. Two complete systems were brought up to flight test readiness and one system was flight-tested. Giannini Controls Corporation provided the source, the detectors with their associated electronics, and the telemetry system. NASA-Langley Research Center provided the external structure, boost

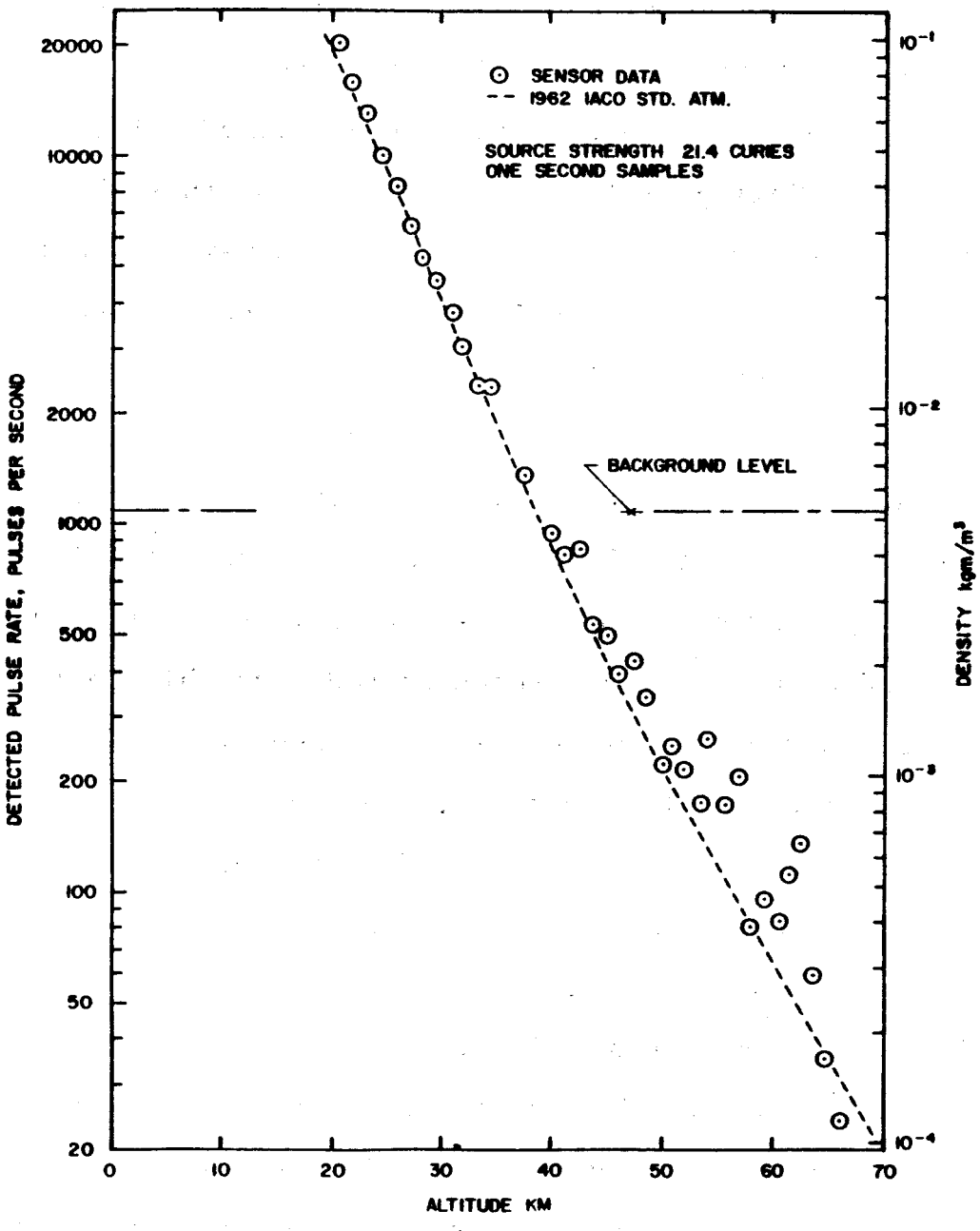


Figure 2 - Gamma Backscatter Air Density Measurement Data, Flight Test 17 December 1964

vehicles, and a mechanism to modulate the source by alternately exposing and shielding the source capsule. System checkout, calibration, and flight readiness testing were performed at Langley Research Center, using NASA facilities.

Flight testing of one system was performed using the NASA test range at Wallops Island. The results of this flight test are shown in figure 3 giving the measured density as a function of altitude. The background is again high and consequently the high altitude capability is not improved.

The significant conclusions reached by examination of the flight data is that multiple skin scattering of high energy gamma photons from the particular radioisotope source used is the cause of the unexpected high ambient radiation levels detected. Additional studies have shown methods of reducing this ambient level and provide direction for further experimental verification of the capabilities of the technique. The feasibility tests have provided a firm basis for the use of this measurement technique to applications such as the measurement of the atmospheric density profile to the planet Mars.

The work reported in this document includes a technical description of the sensing apparatus, a theoretical description of the sensor operation, an error analysis showing the measurement capabilities of the sensor, descriptions of the performance testing of the sensors prior to the flight test, a description of the system calibration procedures and results, a description of the flight and flight test results, analysis of the flight test data, and the final conclusions and recommendations resulting from

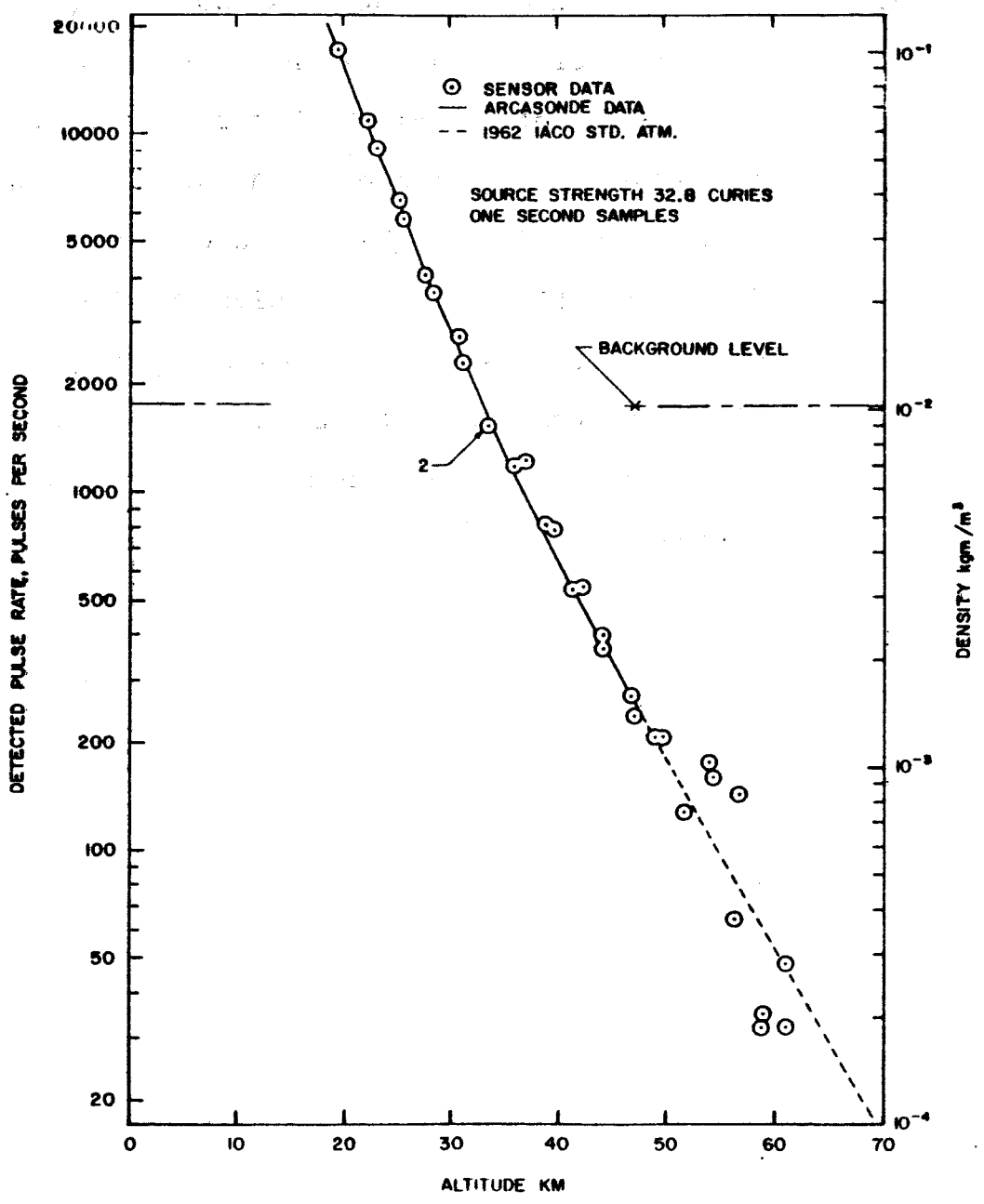


Figure 3 - Gamma Backscatter Air Density Measurement Data, Flight Test 20 January 1966

this program.

This work was a joint undertaking to a large extent between Giannini Controls Corporation and the NASA-Langley Research Center. Acknowledgment of the significant contributors is in order. Mr. John Olivero, of the Flight Instrumentation Division of Langley Research Center coordinated NASA participation and provided the interface between Langley Research Center and Giannini Controls Corporation as the technical monitor of the contracted work. Messrs. R. Gungle, C. Drummond, and R. Haynes were the significant contributors for NASA. Messrs. W. Mutschler and J. Brabec were the significant contributors for Giannini Controls Corporation.

## SYMBOLS AND UNITS

The International System of Units will be used throughout this report.

The symbols are defined below.

| | |
|---|---|
| A | atomic number |
| $A_d$ | detector area; $cm^2$ |
| a | gamma abundance |
| c | velocity of light |
| D | detector diameter, cm |
| D | dose buildup factor |
| E | particle energy, MeV |
| e | electronic charge |
| G | geometry factor |
| $G_o$ | detector geometry factor |
| $G_1$ | fraction of gammas reaching skin |
| $G_2$ | inverse square loss from first scatter to second scatter |
| $G_3$ | fraction of second scattered gammas reaching detector |
| $h_i$ | altitude at the i th data point, km |
| $h_o$ | altitude at the o th data point, km |
| $I_b$ | background radiation level, pulse/second |
| $I_c$ | detected radiation level with the shield closed, pulses/second |
| $I_d$ | detected radiation level, pulses/second |
| $I_o$ | detected radiation level with the shield open, pulses/second |
| $I_o$ | source strength, pulse/second |
| $I_{of}$ | flight source strength, curies |

SYMBOLS AND UNITS - Continued

$I_{ot}$ test source strength, curies

$I_{ss}$ skin scattered radiation to detector, pulses/second

$I_t$ photons transmitted from source to detector through shield, pulses/second

$I_w$ wall scattered radiation level in altitude sphere, pulses/second

K sensor calibration constant, pulses-$sec^{-1}$ - $kgm^{-1}$ - $m^3$ - $curie^{-1}$

$K_a$ fraction of source photons transmitted without absorption

$K_c$ sensor sensitivity with shield closed, pulses-$sec^{-1}$-$kgm^{-1}$-$m^3$

$K_d$ fraction of photons reaching skin transmitted to detector without absorption

$K_o$ sensor sensitivity with shield open, pulses-$sec^{-1}$-$kgm^{-1}$-$m^{-3}$

$K_1$ transmission of 2.18 MeV gammas through radiation shield

$K_2$ transmission of bremsstrahlung gammas through radiation shield

k sensor calibration constant measured in altitude sphere, pulses-$sec^{-1}$-kgm-$m^3$

L detector length, cm

$m_o$ electron mass

N Avogadros Number

$N_d$ number of detected counts, pulses

P pressure in calibration chamber, mm hg

$P_s$ standard pressure, mm hg

r distance from source to detector; cm

$S_d$ detector sensitivity

$S_s$ stability factor associated i th shock layer

s distance from source to scattering center, cm

T temperature in calibration chamber, °K

$T_s$ standard temperature, °K

t distance from detector to scattering center, cm

$v_i$ residual difference

x length of absorption path, cm

$x_1$ thickness of skin near source, cm

$x_2$ length of skin in vicinity of detector, cm

$x_c$ thickness of capsule wall, cm

$x_m$ thickness of modulating shield, cm

$x_s$ thickness of skin, cm

Z atomic weight

$\beta$ coefficient relating the exponential variation of density with altitude, $km^{-1}$

$\epsilon_o$ permittivity of vacuum

$\theta$ angle from source to scattering center with respect to centerline

$\mu$ mass absorption coefficient, $cm^2/gm$

$\mu_c$ capsule mass absorption coefficient, $cm^2/gm$

$\mu_s$ skin mass absorption coefficient, $cm^2/gm$

$\rho$ density, $gm/cm^3$, $kgm/m^3$

$\rho_c$ capsule density, $gm/cm^3$

$\rho_i$ density at the altitude of the i th data point, $kgm/m^3$

## SYMBOLS AND UNITS - Continued

$\rho_i'$ value of the i th data point, $kgm/m^3$

$\rho_m$ modulating shield density, $gm/cm^3$

$\rho_o$ density at the altitude of the o th data point, $kgm/m^3$

$\rho_s$ standard density, $kgm/m^3$

$\rho_s$ skin density, $gm/cm^3$

$\sigma_s$ mass scattering coefficient, $cm^2/gm$

$\tau$ counting time interval, seconds

$\varphi$ angle through which photon scatters

$\varphi$ angle about roll axis

$\psi$ angle from detector to scattering center with respect to centerline

$\frac{d_e\sigma}{\sigma\Omega}$ scattering cross section per electron per unit solid angle $cm^2/electron/radian$

$\frac{d\sigma}{d\Omega}$ mass scattering cross section per unit solid angle, $cm^2/gm/radian$

$h\nu$ quantum energy

## SENSOR TECHNICAL DESCRIPTION

### System Description

The block diagram of the air density sensing system is shown in figure 4. Low energy gamma photons, 134 keV, emitted from the radioactive isotope source scatter in the atmosphere. A portion of these scattered photons is sensed by a pair of scintillation detectors. The rate at which these photons reach the detectors is proportional to the air density. A tungsten shield is placed between the source and detectors to prevent radiation from reaching the detectors directly. A small tungsten modulating shield alternately covers and exposes the source with a two-second period. When the source is covered the output is attenuated and the air-scattered signal is reduced. The air density and background level are then obtained by solution of the following two equations:

$$I_o = K_o \rho + I_b \quad (1)$$

$$I_c = K_c \rho + I_b \quad (2)$$

where

$I_o$ = detected radiation level with the shield open

$I_c$ = detected radiation level with the shield closed

$\rho$ = density of air being measured

$K_o$ = sensitivity of air-scattered radiation with shield open

$K_c$ = sensitivity to air-scattered radiation with shield closed

$I_b$ = background radiation level

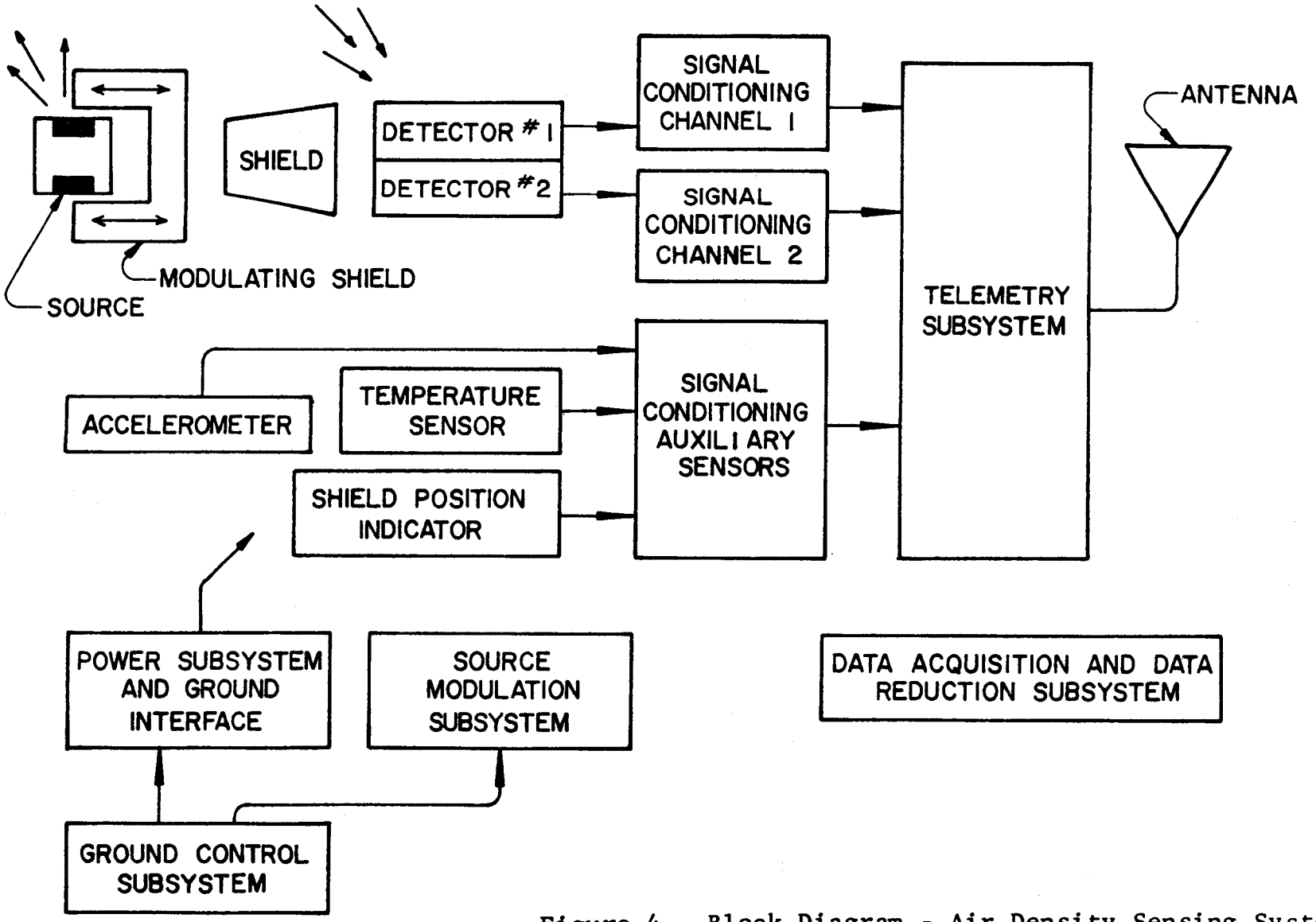


Figure 4 - Block Diagram - Air Density Sensing System

Solving for density gives

$$\rho = \frac{I_o - I_c}{K_o - K_c} \tag{3}$$

and solving for background gives

$$I_b = \frac{K_o I_c - K_c I_o}{K_o - K_c} \tag{4}$$

If the ratio $\frac{K_o}{K_c}$ is very large, these reduce to

$$\rho = \frac{I_o - I_c}{K_o} \tag{5}$$

and

$$I_b = I_c \tag{6}$$

When the shield is closed the detector is measuring background and when the shield is open the detector is measuring air-scattered radiation plus background.

Two detection channels are used to provide redundancy improving reliability. The detector output signals are modified by the signal conditioning circuitry to be compatible with an FM-FM telemetry subsystem.

The data from three auxiliary measurements is also transmitted by the telemetry subsystem. These auxiliary measurements are the longitudinal acceleration of the vehicle, the temperature of the sensor electronics, and a signal showing the position of the modulating shield.

The source modulation subsystem provides the power, motivation, timing, and position indication necessary for the operation of the modulating shield.

The power subsystem and ground interface provides the power necessary to operate the sensor and provides the interface with the ground control subsystem. The ground control subsystem provides, through umbilical cables, means for operating the system on external power, means for switching to internal power, means for charging batteries, and means for monitoring via hardline the sensor outputs.

The data acquisition and reduction subsystem are standard range equipment for receiving, recording, and reducing the telemetry data and radar altitude tracking data. The telemetry data provides the measure of air density and background as a function of time. The radar data provides the measure of altitude versus time. These sets are combined to give a measure of density versus altitude. This density-altitude profile is then compared with measurements made by Arcas Robin, Arcasonde, and radiosonde soundings and the standard atmosphere profile to evaluate performance of the measurement system.

The sensor is carried to altitude by the two-stage Nike-Apache boost system. Figure 5 illustrates the mechanical arrangement of the various elements of the system. Figure 6 illustrates the sensor relationship

## Source and Shielding

The radioactive isotope source and shielding are located in the vehicle nose cone in the configuration shown in figure 7. The source material is encapsulated in two sealed stainless

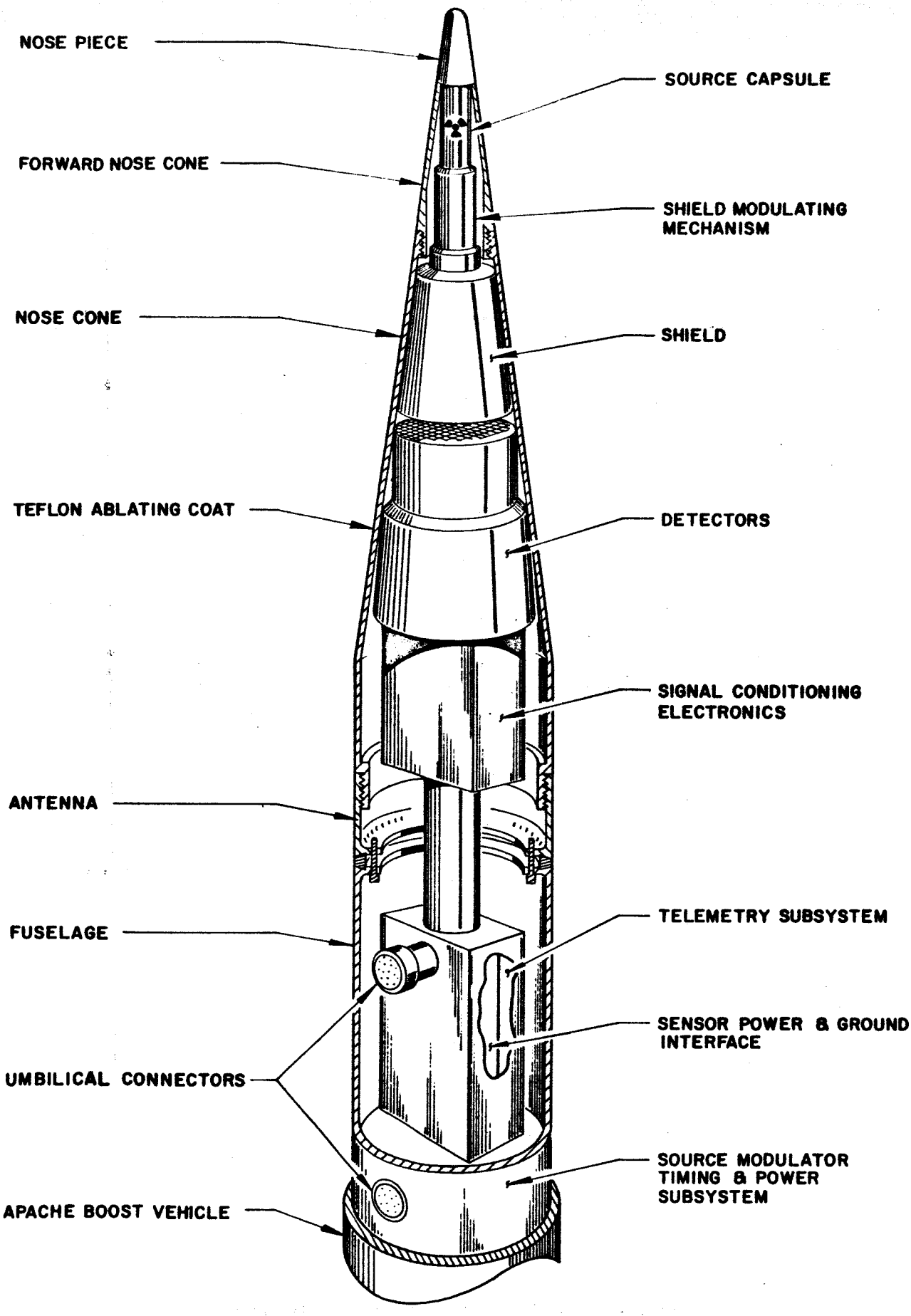


Figure 5 - Sensor Mechanical Configuration

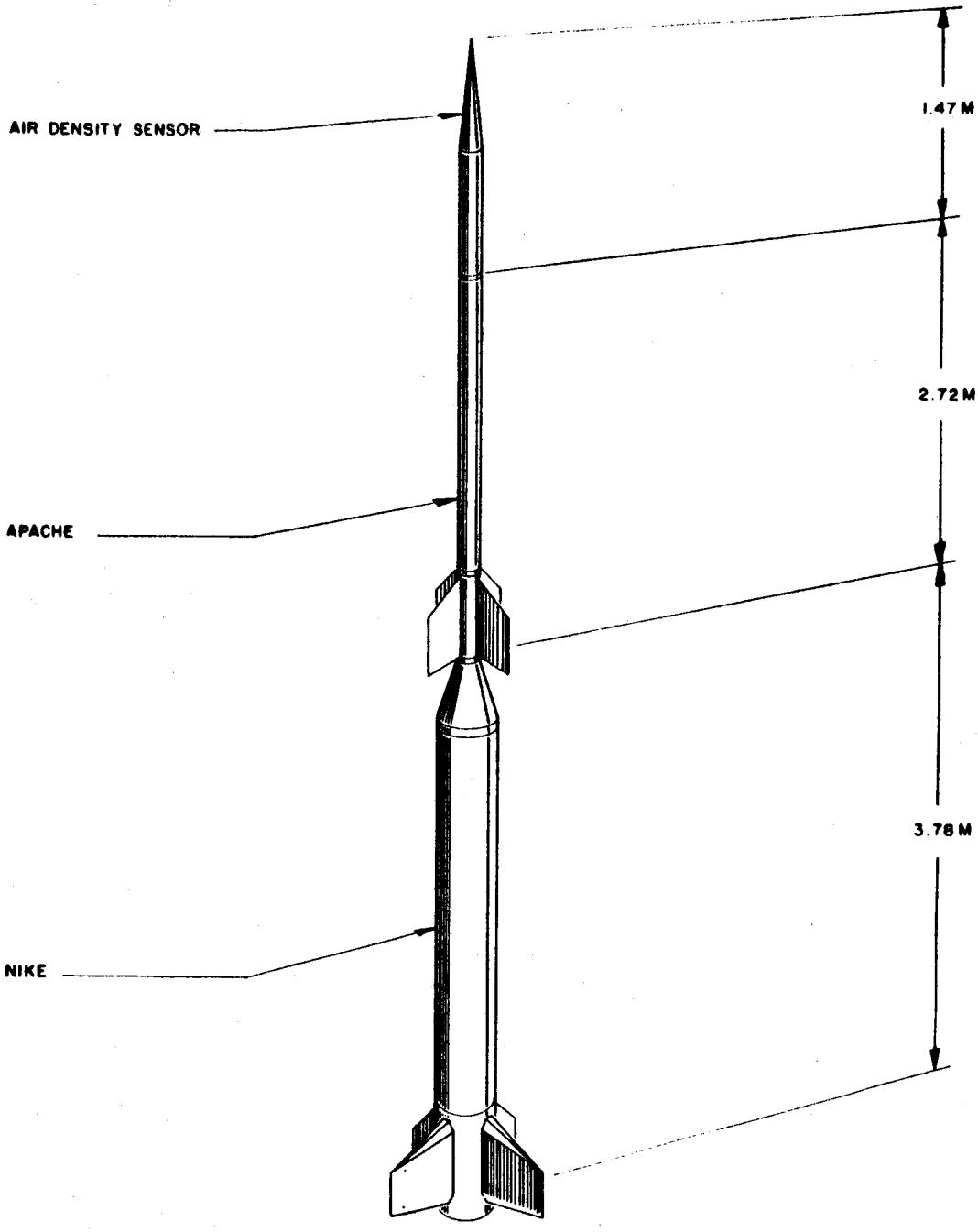


Figure 6 - Sensor and Boost Vehicle

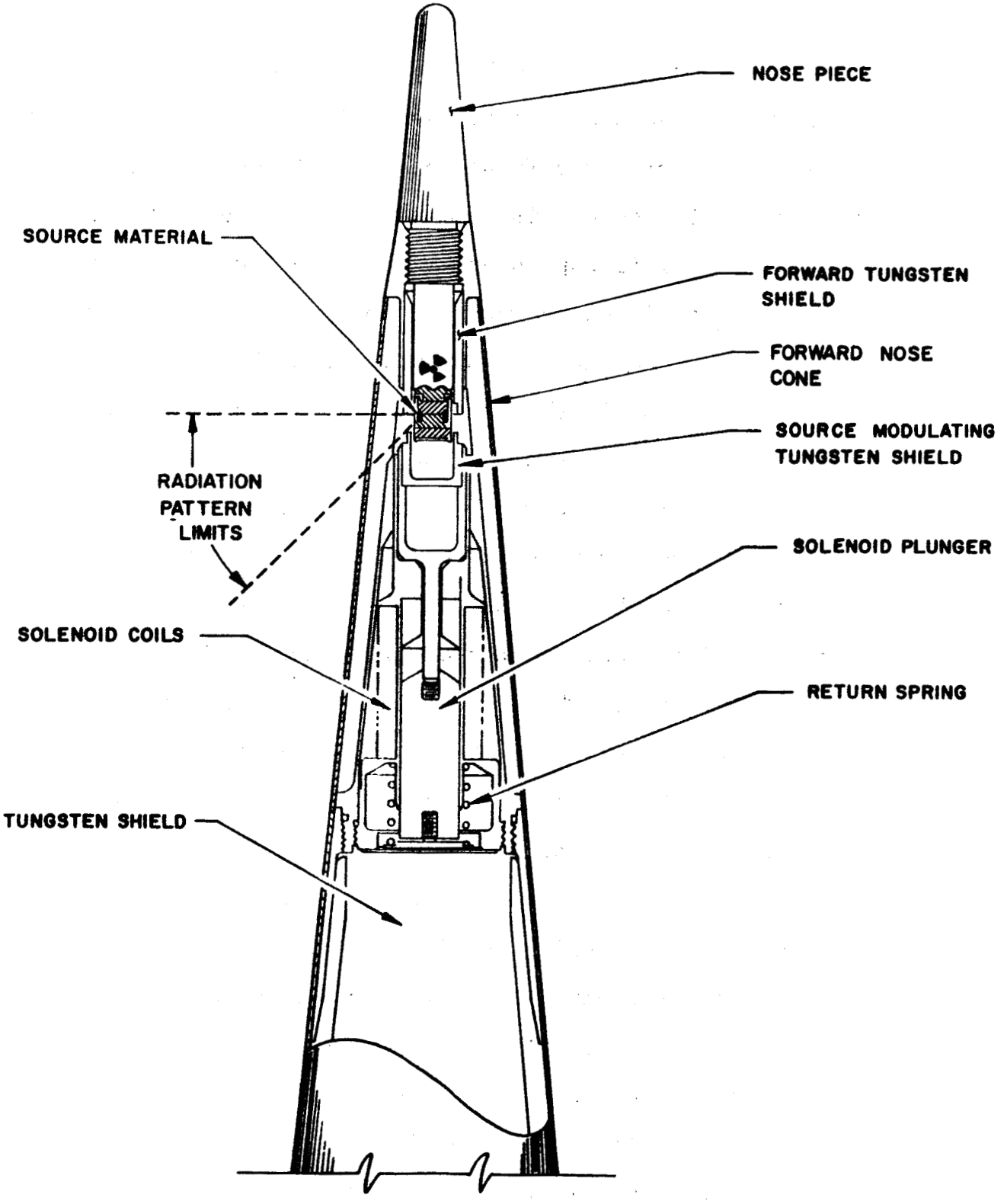


Figure 7 - Source and Shielding

steel containers, the outer one being an integral part of the nose piece. This nose piece/source assembly is screwed into the forward nose cone during the final phases of launch preparation. The source modulating shield is a small tungsten cup with 0.318 cm wall thickness. This cup covers the source when the solenoid is energized and is withdrawn when the solenoid is deenergized. The forward tungsten shield and carefully controlled solenoid stroke accurately maintain the source pattern when the shield is open. A truncated conical tungsten shield 23.1 cm in length protects the detector from direct transmission.

Source. - The source material used in this experiment is Cerium-144 and its daughter Praseodymium-144. The decay scheme, significant emissions, and abundance per disintegration are illustrated in figure 8. The 134 keV gammas are the photons useful for density measurement. Their energy is relatively low such that the air exhibits a high scattering cross section. This energy is also high enough so that self absorption and absorption by the vehicle skin is not severe. The few percent of high energy gammas is undesirable since it requires a thick shield to attenuate the direct transmission from the source to detector. The high energy betas are also undesirable since the bremsstrahlung radiation created by these betas as they pass through the capsule walls is a significant portion of the high energy gamma flux. The selection of Cerium-144, however, was based on the fact that for this experiment heavy shielding was

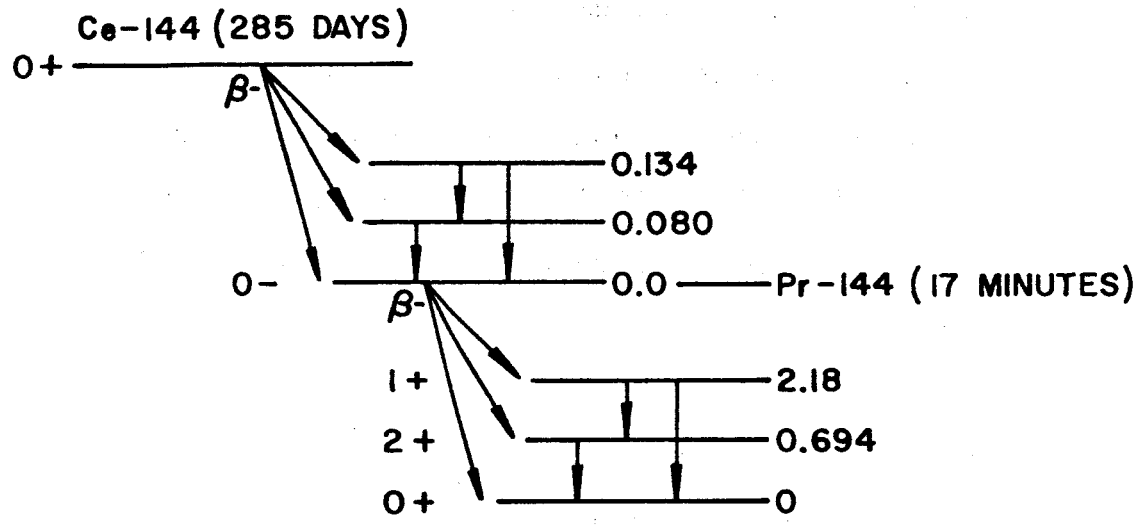


| SIGNIFICANT GAMMAS MeV | ABUNDANCE | SIGNIFICANT BETAS MeV | ABUNDANCE |
|---|---|---|---|
| 2.185 | 0.03 | 3.150 | 0.95 |
| 1.480 | 0.012 | 2.450 | 0.03 |
| 0.695 | 0.03 | 0.900 | 0.02 |
| 0.134 | 0.30 | 0.320 | 0.60 |
| 0.080 | 0.10 | 0.245 | 0.05 |
| 0.036 | 0.30 | 0.184 | 0.30 |

Figure 8 - Decay Scheme, Cerium-144/Praseodymium-144

less of a problem that obtaining a high strength source with no high energy flux.

The half life of Cerium-144 is 285 days. This is long enough so that once the source is fabricated long delays in flight test schedules do not cause intolerable weakening of the source strength. The half life of the Praseodymium-144 is 17 minutes. The daughter is thus shortly in equilibrium with the Cerium-144.

Three sources are used to calibrate and test the sensor. A 10 microcurie source is used to calibrate the detector electronics and is used to verify sensor operation during pre-launch activity. A half-curie test source is used to calibrate the sensor in a large altitude chamber. This source is fabricated in a configuration identical to the flight source. Cerium Oxide is mixed with the isotope such that the self absorption characteristics are the same. The ratio of strengths between the test source and flight source may then be used to modify the calibration obtained with the lower strength source. A 50 curie source is used for flight testing.

Cerium-144 is available with a very high specific activity, >200 curies/gm. This makes possible a nearly point source. The ring source of figure 7 is 0.075 $cm^3$ in volume. With a density of 6.0 $gm/cm^3$, this allows 0.45 gram of Cerium. A 50 curie source then requires source material having a specific activity of 110 curies/gram.

The dose rate constant for Cerium-144 is 2.0r $-2m^2$/mc-hr

(ref. 3). This is reduced considerably by absorption when encapsulated in the source container. For safety calculations the above value is used for conservative results.

Tungsten Shield. - The tungsten shield is 23.1 cm in length fabricated from a single piece of tungsten with a density of 17.7 $gm/cm^3$. The shield has a spiral groove machined down the side to aid in bonding the shield to the fiberglass skin. In addition, a longitudinal groove provides a path for the electrical cable to the source modulating mechanism.

Source Modulating Shield. - The source modulating shield and solenoid are located in the forward nose cone as seen in figure 7. The solenoid controller and batteries are located in the aft fuselage section. The block diagram of the source modulating subsystem is shown in figure 9. The modulating shield covers the source when the solenoid is activated and exposes the source when the solenoid is deactivated. The solenoid is controlled by the solenoid activation switch which provides power from the battery. The switch is controlled by the timer which provides the one-second open one-second closed sequence. The shield position indicating switch switches a zero and five-volt reference signal to the telemetry system as an indication of shield position. The ground interface switch and umbilical make possible remote operation of the shield modulator with ground power.

The shield mechanism is designed to operate under all conditions of acceleration expected, except the boost acceleration. Under boost, the shield remains open and the source remains ex-

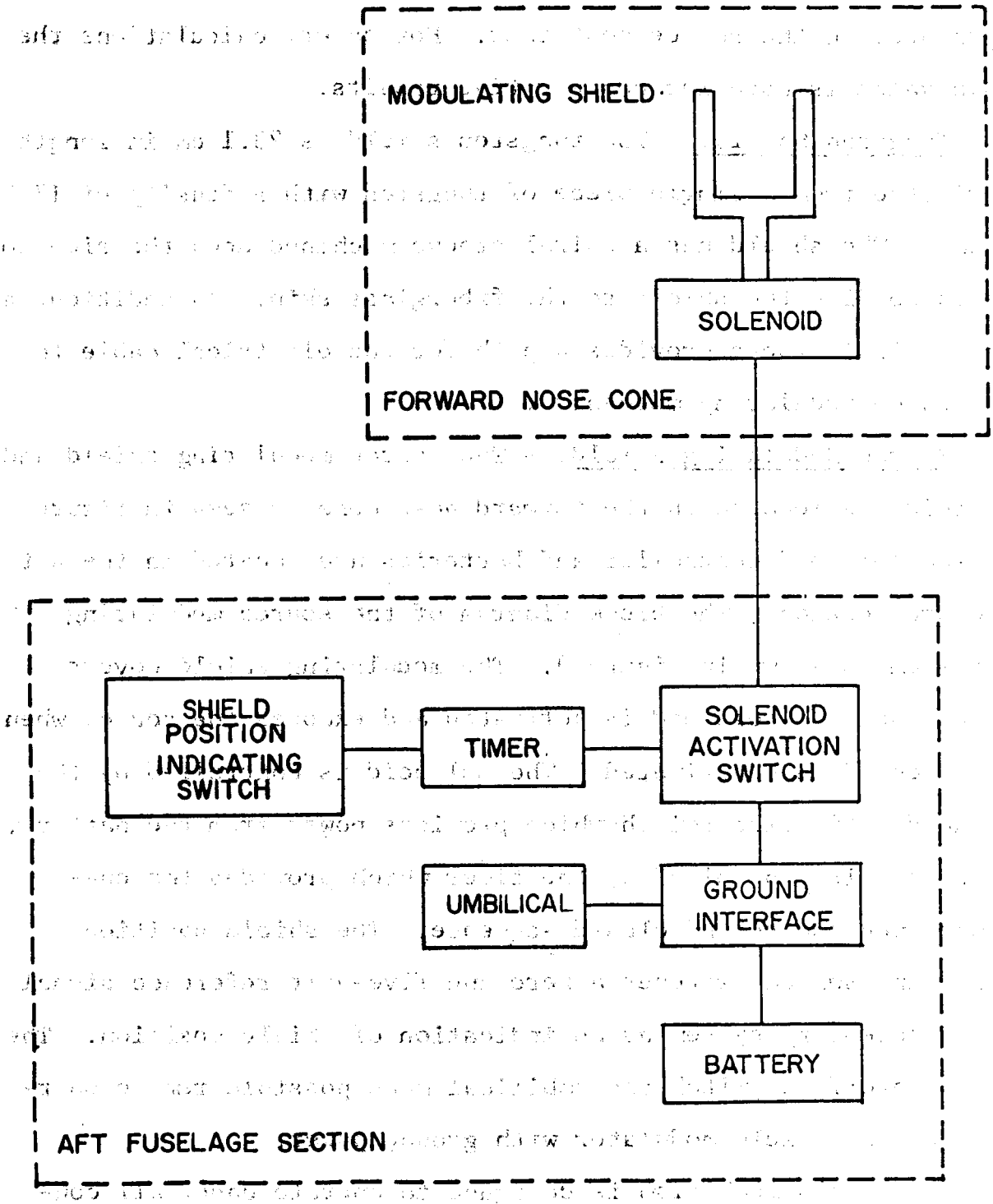


Figure 9 - Block Diagram, Source Modulating Subsystem

posed. Any failure of the source modulating subsystem will leave the source exposed such that the density measurement may still be made.

## Detector

The detector assembly is illustrated in figure 10. The gamma radiation is sensed by two thallium activated sodium iodide crystals. As the gamma photons are absorbed by the crystal, the energy is converted to light scintillations. The magnitude of the light scintillation is proportional to the energy absorbed by the crystal. The light passes through the optical coupling to the face of the photomultiplier tube. Here, the light ejects electrons from the photocathode which are multiplied as they avalanche down the string of dynodes. The output pulse at the photomultiplier tube anode is thus of measurable magnitude and proportional to the energy deposited in the crystal by the gamma photon.

Crystal Assembly. - The sodium iodide crystal assembly consists of two half-cylindrical crystals 4 cm thick by 8.5 cm diameter. These two crystals are separated by a thin tungsten shield so that they may operate independent of one another. The crystals are mounted in an aluminum housing, are coated with light reflective material, and cushioned in a shock-absorbing material. A glass window 2.5 cm in diameter is epoxied into position against each crystal. This whole assembly is of very rugged construction considering the usual fragility of large sodium iodide crystals.

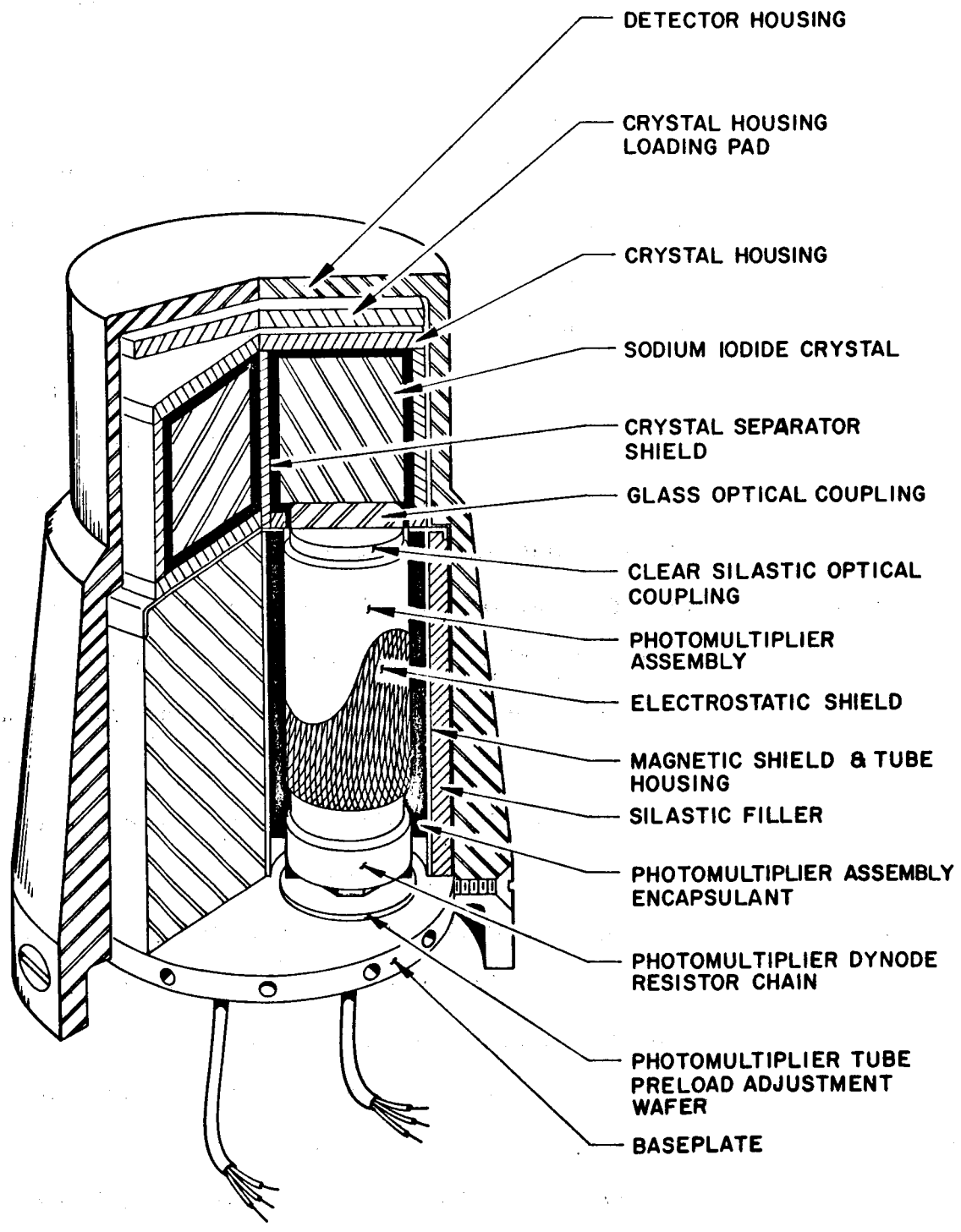


Figure 10 - Detector Assembly

Photomultiplier Tube Assembly. - The photomultiplier tubes are of rugged construction with a semitransparent photocathode and ten dynodes. The nominal accelerating voltage applied across the tube is 1,000 volts providing a gain of $6 \times 10^5$. The dynode resistor chain consists of ten 100k ohm resistors and one 200k ohm resistor between the cathode and dynode number one. Capacitors are connected to the last three dynodes to maintain voltage and gain at high pulse rates. These components are encapsulated in the photomultiplier tube assembly at the base of the tube. An electrostatic shield wrapped around the photomultiplier tube holds the tube envelope at the photocathode potential. The photomultiplier assembly is held in place by a hypernom tube which also serves as the magnetic shield.

Detector Housing. - The crystal assembly and photomultiplier tube assemblies are housed in an opaque fiberglass container. The crystal assembly is held in place by a 1000-pound preload applied by the crystal housing loading pad against the tube housing, silastic filler, and base-plate. This high preload was necessary to minimize vibration resonance of the crystal assembly in the detector. The photomultiplier tubes are held against the crystal assembly by a 20-pound preload. This prevents the photomultiplier tube from pulling away from the crystal assembly when subjected to the boost acceleration. This detector assembly is attached to the sensor internal structure by the base-plate.

Detector Output. - The detector output pulses, corresponding

to the 134 keV gammas detected, are approximately 30 millivolts high and 0.5 microsecond wide. The pulse height resolution of these detectors is quite poor, due to the peculiar geometry and small window area. The pulse height spectrum from the Cerium-144 source, as measured by this detector, is shown later in this report (see figure 23).

## Signal Conditioning

The signal conditioning electronics operate on the detector output to provide signals that are compatible with the FM-FM telemetry subsystem. This signal conditioning is illustrated in the block diagram of figure 11. The pulse outputs from the detector after amplification are selected on a pulse height basis by the level discriminators. Pulses above a certain threshold are selected, shaped, and passed on to the scaler. Two level discriminators are used with each detector. The levels are set above and below the pulse heights equivalent to the particular energy of interest. The difference in pulse rates from the low level discriminator minus the upper level discriminator is equivalent to the pulse rate of those pulses falling between the two levels. In this way, low level noise is rejected and high energy background is rejected. The scalers divide the pulse rate by 16 in order to lower the bandwidth requirement of the telemetry system and somewhat regularize the random time spacing of the pulses. The filters limit the high frequency component of the signals sent to the telemetry subsystem.

Discriminators. - The amplifier, low level discriminator,

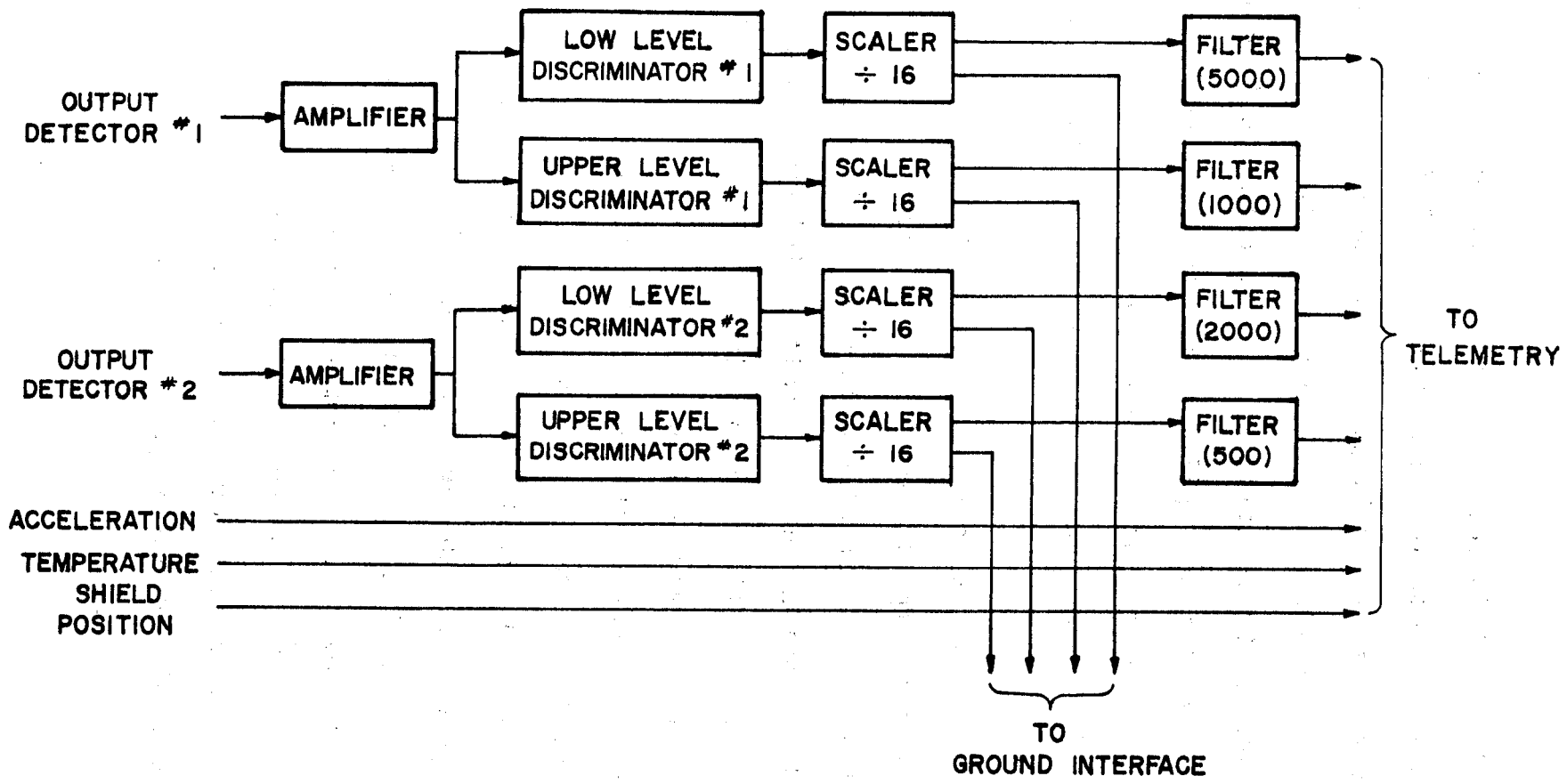


Figure 11 - Block Diagram, Signal Conditioning

and proper level discriminator for each detector channel are packaged into a single module. This module amplifies the photomultiplier tube output by a voltage gain variable from 20 to 70. The amplified signals are then selected, using tunnel diode triggering circuits. These circuits provide output pulses for all input pulses greater in amplitude than the desired base level.

The discriminator output pulses are 6 volts in height and 0.2 microsecond in width. The trigger circuitry operates up to $5 \times 10^5$ pulse per second rates.

Scaler. - The scalers consist of a series of four flip-flop modules. The fourth flip-flop modifies the output pulse for compatibility with the input requirements of the telemetry subsystem voltage-controlled oscillators. An emitter follower output is taken from this fourth flip-flop to drive signals through long monitoring cable of the ground interface.

Filters. - The output of the scalers is attenuated at high pulse repetition rates by low pass filters. The cutoff frequencies of these filters are 500, 1,000, 2,000, and 5,000 cps.

Auxiliary Sensors. - The vehicle longitudinal acceleration is measured by the accelerometer with a range of -10 to +40 g and a potentiometer output. The temperature of the sensor electronic circuitry is measured by a thermistor network. The regulated reference voltage for the accelerometer, thermistor networks, and shield position signal are obtained from a small sensor interface module.

The FM-FM telemetry used to transmit data to the ground station is illustrated in figure 12. The transmitter has a 2-watt output minimum and a carrier frequency of 244.3 megacycles per second.

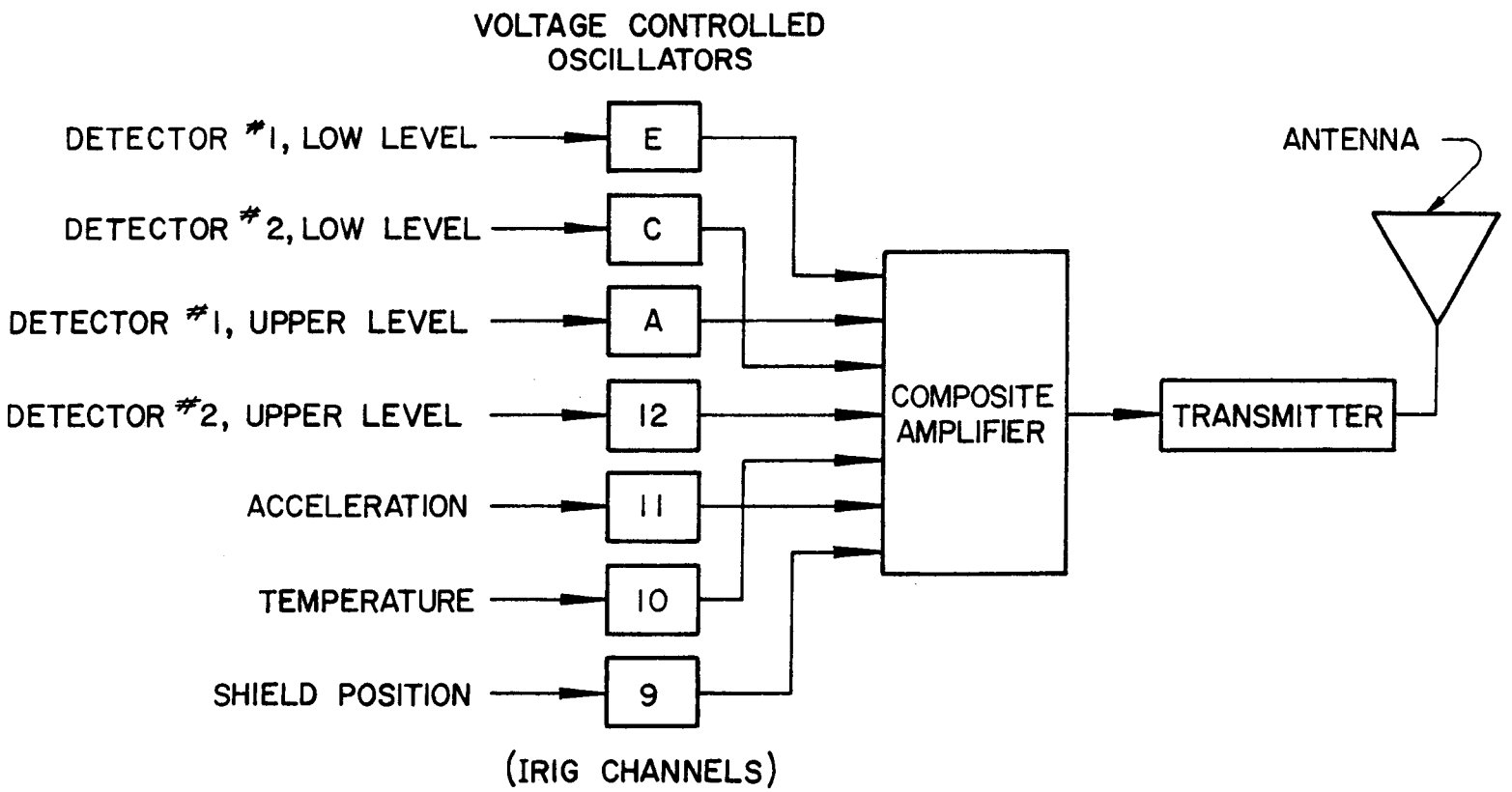


Figure 12 - Block Diagram, Telemetry Subsystem

Seven voltage controlled oscillators and a composite signal amplifier are used to modulate the transmitter. Standard IRIG subcarrier channels are used. Channels 9, 10, and 11 carry low bandwidth information; Channels 12, A, C, and E carry pulse data.

The antenna is constructed as part of the fuselage of the payload section. A forward ring segment of the fuselage is separated from the rest of the fuselage by an alumina insulator. This ring is excited by the transmitter output.

An RF shielding cover and gasket are placed over the entire telemetry section to minimize noise in the sensor. All electrical connections through this shielded section are made through low pass filters to minimize RF noise on power and signal lines.

## Power Subsystem

Primary power for the sensor is derived from a battery pack of 24 nickel cadmium rechargeable batteries. The total payload, not including the source modulating subsystem which contains its own power source, requires 1.1 amperes of 28 volts dc current.

Primary power is converted to several voltage levels by a dc/dc converter. Negative 1.5 volts, -1000 volts, +12 volts, +22 volts, and +28 volts are required by the sensor.

## Ground Interface

During calibration and checkout prior to launch, external power is supplied and sensor outputs are monitored via an

umbilical connector, cabling, and test set. Interlock circuitry is provided which prevents any voltage from being present on either connector until the two are properly mated. A set of six two-pole, double-throw, half-size crystal can, latching relays perform this deactivation of the umbilical in the payload as well as switch battery power to the sensor electronics and telemetry subsystem. Two relays are used in parallel to switch the power in order to improve the reliability of this critical function.

The functions of the test set are listed below:

1) Provide ground power to the sensor electronics and display current
2) Provide ground power to the telemetry subsystem and display current
3) Provide battery charging function and display charging current
4) Switch from ground power to battery power and vice versa
5) Measure and display elapsed time accumulated on battery power

## Structure

The mechanical structure can best be described by referring to figure 5. The Source Modulator Timing and Power Subsystem are mounted in a cylindrical aluminum housing attached to the head cap of the Apache boost vehicle.

The internal structure is volted to the top of this housing.

The internal structure consists of two aluminum H beam sections on which system components are mounted. The lower beam section is welded to a thick base plate which also serves as a heat sink to slow the heat transfer from the external skin. A cylindrical section connects the lower and upper beam sections and provides electrical clearance for the antenna flanges. The detector is bolted to a plate welded to the forward end of the upper beam section.

The external structure consists of a stainless steel fuselage, separated longitudinally into two sections which are insulated from one another by a ring of alumina; a fiberglass nose cone containing the tungsten shield; a fiberglass forward nose cone containing the shield modulating mechanism; and a stainless steel nose piece supporting the source capsule. These sections are threaded together. The joints between the fuselage and nose cone and the nose cone and forward nose cone are breach lock.

The weight summary is given below:

| | |
|---|---|
| Shield timing assembly | 6.4 kgm |
| Sensor assembly | 14.3 kgm |
| Fuselage and nose cones | 38.0 kgm |
| Total - | 58.7 kgm |

# THEORY OF OPERATION

A theoretical treatment of the air density sensing system operation is given in this section. The physics of scattering is discussed and the characteristics of the source and detector are outlined.

## Physics of Scattering

Many modes of interaction of gamma rays with matter are possible. Compton scattering, photoelectric absorption, and pair production dominate strongly for the gamma ray energies to be considered. Effects of other processes are negligible. The three significant processes are described below.

Compton Scattering. - A gamma ray scatters from a single electron which is in an orbit about a nucleus. This electron absorbs some of the gamma ray energy and is freed from its orbit. The energy of the scattered gamma ray depends upon its original energy, the energy required to free the electron, and the angles of scattering.

Photoelectric Absorption. - The gamma ray energy is completely transferred to an orbiting electron which then leaves its orbit.

Pair Production. - The gamma ray interacts with the electric field about a nucleus or an electron and is converted into a positron and an electron. A minimum gamma ray energy of 1.02 MeV is necessary.

Of these three interaction processes, pair production is small since there are few gamma photons with energies greater

than 1.02 MeV, and photoelectric absorption creates electrons which have a negligible chance of being counted. The Compton scattering is the most significant process.

The Compton scattering process has been described theoretically by Klein and Nishina showing that the differential cross section for the number of photons scattered into unit solid angle at angle $\varphi$ per electron of material is given by

$$\frac{d_e\sigma}{d\Omega} = \frac{e^4}{32\pi^2 \epsilon_o^2 (m_o c^2)^2} \left(\frac{1}{1 + \alpha \text{ vers } \varphi}\right)^2 \left(1 + \cos^2 \varphi + \frac{\alpha^2 \text{ vers}^2 \varphi}{1 + \alpha \text{ vers } \varphi}\right) \quad (7)$$

where

$$\alpha = \frac{h\nu}{m_o c^2} \quad (7a)$$

$$\text{vers } \varphi = 1 - \cos \varphi \quad (7b)$$

This relation is illustrated in figure 13 showing the energy and angular dependence on the scattering cross section.

This electron scattering cross section, when multiplied by the number of electrons per unit density of the scattering media gives the mass scattering cross section $(\frac{d\sigma}{d\Omega})$. For gases this is

$$\frac{d\sigma}{\sigma\Omega} = \frac{d_e\sigma}{d\Omega} \frac{NZ}{A} \quad (8)$$

For most gases the ratio of atomic weight to atomic power number, Z/A, is very close to two. The scattering cross section of gases is thus nearly independent of the gas composition.

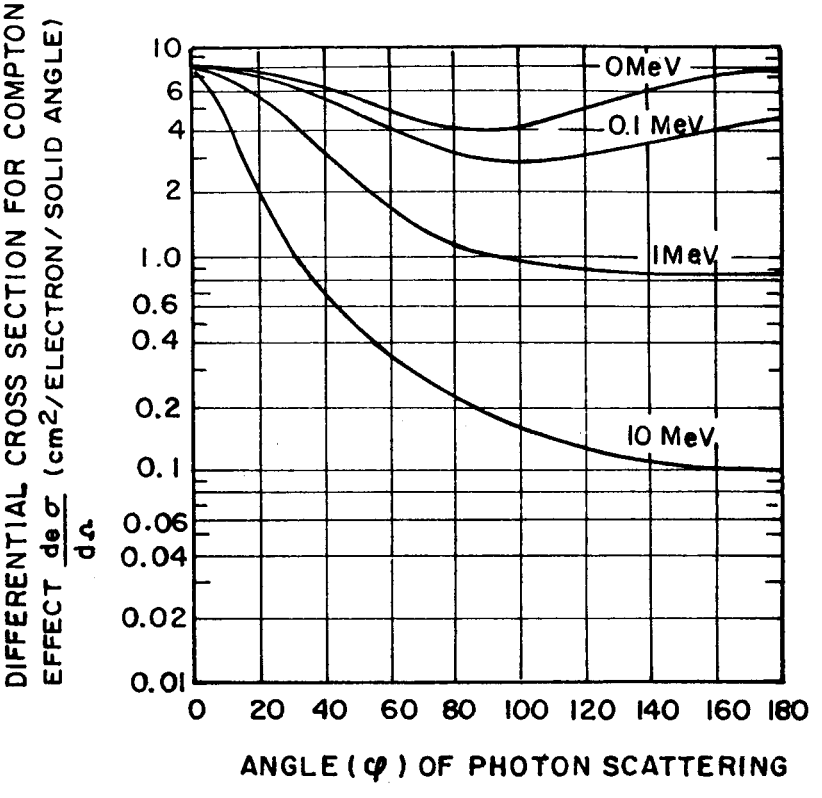


Figure 13 - Graphs Showing $\frac{d_e\sigma}{d\Omega}$ as a Function of the Angle of Photon Scattering for Several Photon Energies

A prediction of the system sensitivity in terms of photons scattered into the detector per unit time can be computed for a particular source strength, geometry, and air density from the above equations. This becomes quite involved when the angular dependence of the scattering cross section is considered. For approximate prediction, the angular dependence will be assumed equal for all scattering angles. Referring to figure 13 and remembering that the energy is low and the scattering angles are small, it is seen that the assumption of equal angular dependence does not modify the result to a large extent. A single scattering coefficient will be assumed as the differential cross section $\frac{d\sigma}{d\Omega}$ integrated over angles from 0 to 180 degrees. The resultant scattering coefficient as a function of photon energy is shown in figure 14. This coefficient, when multiplied by the density of the scattering medium and a differential length, gives the ratio of photons scattered to the number incident.

The energy of the scattered photons is less than the energy of the incident photon and dependent on the scattering angle and incident energy. This relationship is illustrated in figure 15 showing the fraction of energy given to the scattered photons as a function of the angle of photon scattering for various photon energies. Notice that at low incident energies and low scattering angles the photon loses very little energy.

## Source Characteristics

The Cerium-144 source used in the experiment has a series of gamma and beta emissions previously listed in figure 8. The beta particles as they are absorbed in the source capsule generate

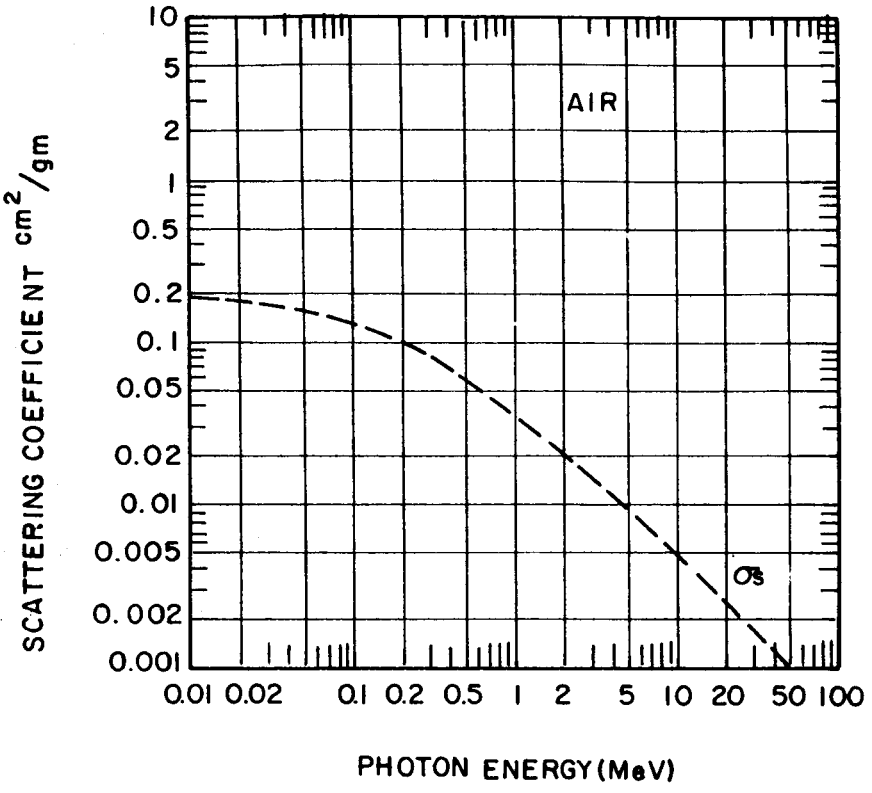


Figure 14 - Graph of Scattering Coefficient as a Function of Photon Energy for Air

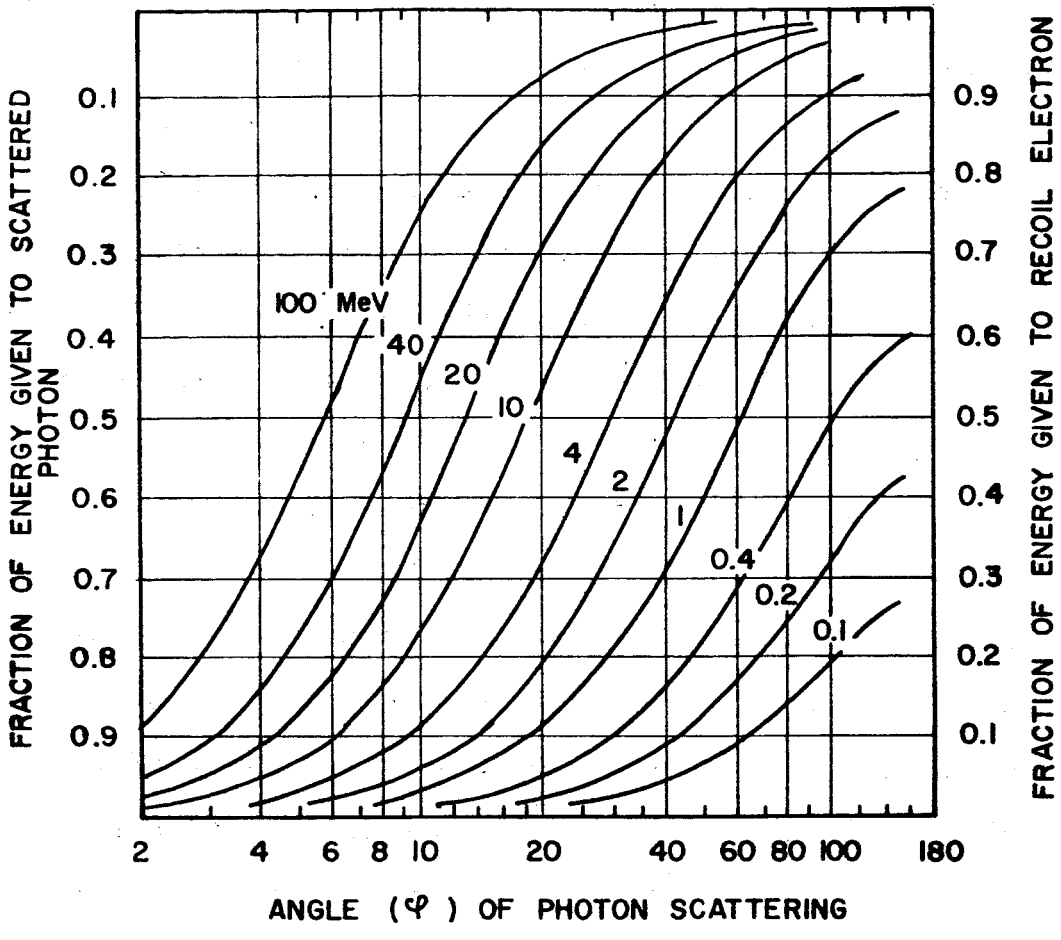


Figure 15 - Graphs of the Fraction of Energy Given to Scattered Photons versus the Angle of Photon Scattering for Various Energies

additional bremsstrahlung radiation. The total spectrum of gamma energy from the source is discussed in Appendix A. The predominant energy for scattering purposes is the 134 keV line. Referring to figure 8, the abundance, a, of this line is 30%, i.e., thirty 134 keV emission per one hundred disintegrations of the source. A fraction of these photons is absorbed as they leave the vehicle. The absorption takes place in the source material itself, in the capsule walls, and in the vehicle skin. The expression describing this absorption is:

$$K_a = e^{-\mu\rho x} \tag{9}$$

where $K_a$ is the fraction of initial photons transmitted without absorption, $\mu$ is the mass absorption coefficient for the material and energy being considered, $\rho$ is the density of the material, and x is the thickness of the material. With the ring source illustrated in figure 7, the length of the absorption path depends on the angle at which the photon leaves the source. Those leaving the source radially away from the center line are attenuated by a factor of 45%. Those leaving the source radially toward the center line are attenuated by a factor of 90.3%. Those leaving radially at an angle of 45 degrees away from the center line are attenuated by a factor of 57%.

The forward and rear angular limits are established by the location of the tungsten shields. It is estimated that within the limits of the shields, absorption effects reduce the available 134 keV photons by a factor of 0.90, i.e., $K_a = 0.10$.

## Source Modulator

When the tungsten cup of the source modulator covers the

source capsule it attenuates the source output flux severely. The tungsten cup is 0.317 cm thick and exhibits a density of approximately 17 $gm/cm^3$. The resultant transmission as a function of photon energy is shown in figure 16. The photon energy spectrum after attenuation is discussed in Appendix A.

## Detection

The thallium activated sodium iodide crystals employed in the sensor are highly efficient for the detection of the 134 keV gamma photons. The detection area was maximized by using a large diameter crystal, approximately 8.5 cm. This was done at the sacrifice of energy resolution since only a 5 $cm^2$ photomultiplier tube window is employed with each 28 $cm^2$ half crystal face, thus providing relatively poor light collection. The detection sensitivity to incident photons is modified by the absorption of the skin and crystal housing and the detector area "seen" by the incident photons. This sensitivity ($S_d$) can be described mathematically as follows:

$$S_d = A_d K_d \sin\theta \qquad (10)$$

where $A_d$ ($\sin\theta$) is the area presented to the photon entering at angle $\theta$ from the roll axis, and $K_d$ is the transmission through the skin and detector housing. For the 134 keV gamma photons, $K_d = 0.75$.

The time response of the detector is limited by the scintillator decay constant. For sodium iodide this is 0.25 $\mu$ second. To insure counting losses of less than one percent, it is necessary to operate at counting rates under 20,000 pulses per second.

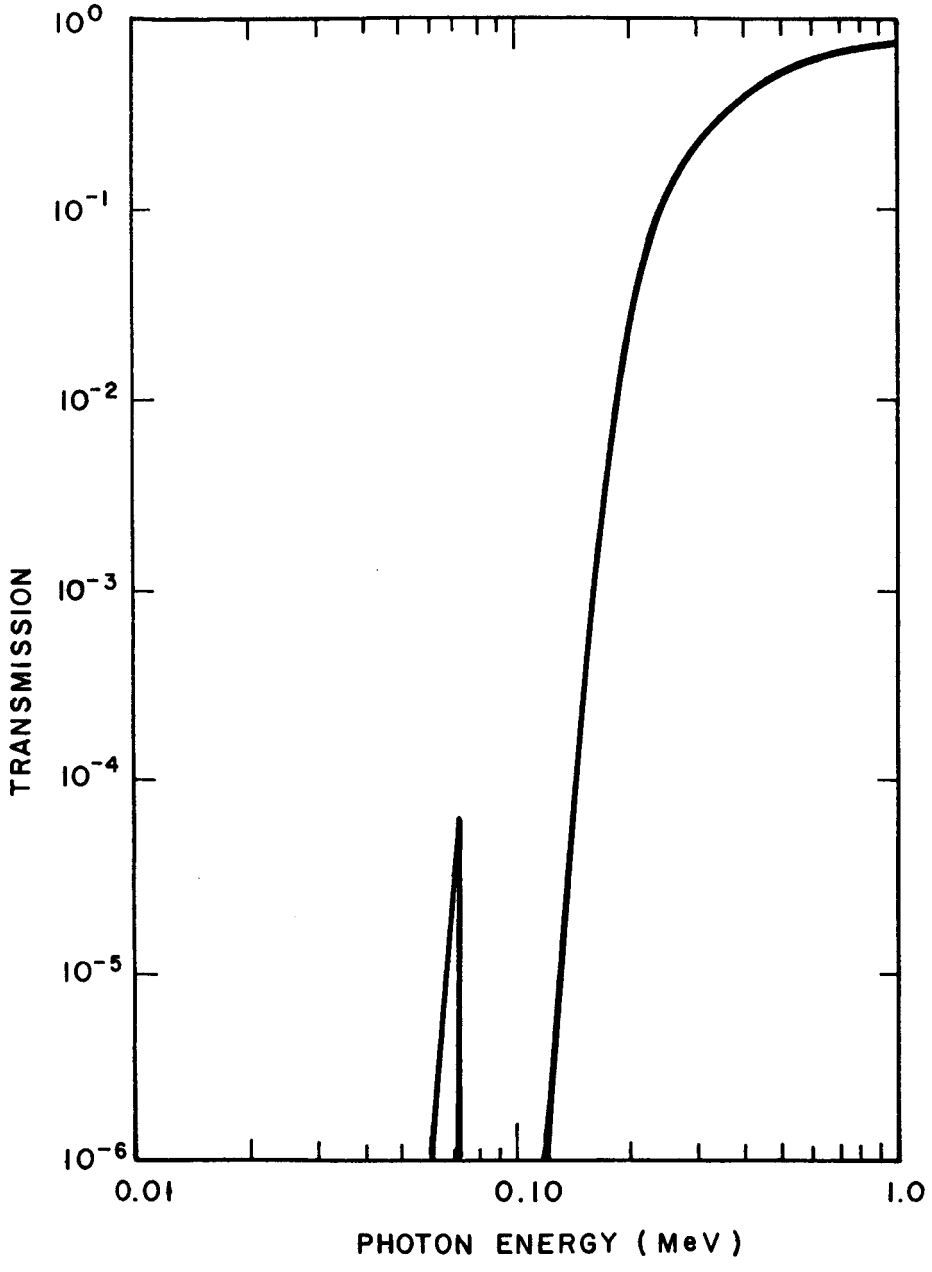


Figure 16 - Curve of Transmission Versus Photon Energy for the 0.317 cm Thick Source Modulating Shield

## Mathematical Model

A mathematical model of the sensor has been derived to predict the system response to the measured air density.

Referring to the geometries indicated in figure 17, the following relations are derived

$$dI_s = \frac{I_o \; a \; K_a \; \sigma_s \; \rho \; \sin \psi}{4\pi} \; d\varphi \; d\psi \; ds \qquad (11)$$

Each scattering center is assumed a differential source, $dI_s$, whose strength is proportional to the flux passing through a differential volume of air with a thickness ds, a density $\rho$ and a scattering cross section $\sigma_s$.

The amount of flux reaching the differential volume of air is equal to the effective source strength, $I_o$ a $K_a$, times the solid angle encompassed by the differential volume, $\sin \psi \; d\varphi \; d\psi$, divided by the total solid angle, $4\pi$.

The amount of flux reaching the detector, $dI_d$, from this differential source is proportional to the strength, $dI_s$, the detector sensitivity, $S_d$, and inversely proportional to the square of the distance to the detector, t.

$$dI_d = \frac{dI_s \; S_d}{4\pi \; t^2} \qquad (12)$$

Equations 10, 11, and 12 may be combined and simplified using the geometrical relationships of figure 17 to give the following expression:

$$dI_d = \frac{I_o \; a \; K_a \; A_d \; K_d \; \sigma_s \; \rho \; \sin \theta}{(4\pi)^2 \; r} \; d\varphi \; d\theta \; d\psi \qquad (13)$$

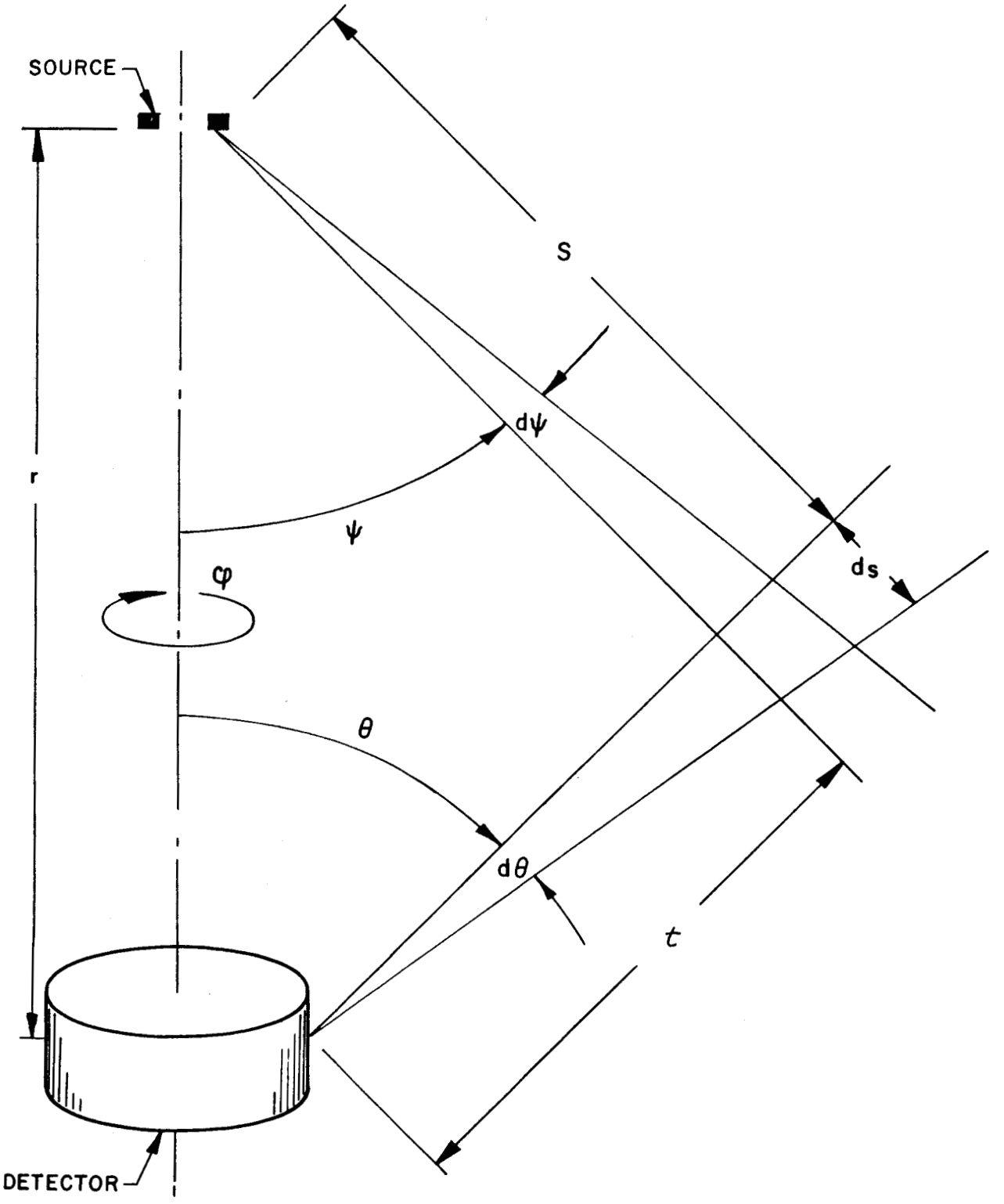


Figure 17 - Geometries for Math Model

This expression may be integrated through the angles $\varphi$, $\vartheta$, and $\psi$ to give the total flux $I_d$.

$$I_d = \frac{I_o \; a \; K_a \; A_d \; K_d \; \sigma_s \; \rho}{(4\pi)^2 \; r} \iiint \sin \; \theta \, d\varphi \, d\psi \, d\theta \qquad (14)$$

The limits of integration are

$$\varphi = 0 \longrightarrow 2\pi$$
$$\theta = 0 \longrightarrow \pi - \psi$$
$$\psi = \psi_1 \longrightarrow \psi_2$$

$\psi_1$ and $\psi_2$ are the limits of the source emission pattern established by the tungsten shields.

Performing the indicated integrations gives the following expression:

$$I_d = \frac{I_o \; a \; K_a \; A_d \; K_d \; \sigma_s \; \rho}{8\pi} \; G \qquad (15)$$

where G is the geometry factor

$$G = \sin \psi_2 - \sin \psi_1 + \psi_2 - \psi_1 \qquad (16)$$

For the source limits of $\psi_1 = 30°$ and $\psi_2 = 90°$,

$$G = 1.55$$

The scale factor per curie of Ce-144 source at the 134 keV energy is computed below.

$A_d = 34 \text{ cm}^2$

$K_d = 0.75$

$I_o = 3.7 \times 10^{10}$ protons/second

$a = 0.30$ abundance of 134 keV photons

$K_a = 0.10$

$\sigma_s$ = 0.12 $cm^2/gm$ from figure 14 for 134 keV photons

r = 43.0 cm separation of source and detector

Thus

$$I_d = K\rho$$

where

$$K = 4.85 \times 10^6 \text{ pulses-second}^{-1}\text{-gm}^{-1}\text{-cm}^3\text{-curie}^{-1}$$

Applying the scaling factor of 16 and changing density units gives

$$K = 304 \text{ pulses-second}^{-1}\text{-kgm}^{-1}\text{-m}^3\text{-curie}^{-1}$$

Background

In addition to the air scattered flux, a background level is detected. This background is composed of several elements. These are cosmic radiation, solar radiation, the direct transmission from the source to the detector through the radiation shield, multiple scattering from the source to the detector through the vehicle skin, and electrical noise.

Solar Radiation. - The solar radiation contribution to this flux consists of solar X-rays which are of low energy and contribute negligible background, and the proton flux from solar flares. A review of the solar flare activity (ref. 4) at the time of the 20 January 1966 flight test indicates that the background contribution from solar flares is negligible.

Cosmic Radiation. - Primary cosmic rays consist of extremely high energy charged particles which impinge on the earth's atmosphere from outer space. About 86% of the primaries are

protons, 12.7% are helium nuclei, and the remaining 0.3% are the nuclei of atoms of atomic number greater than 2. As these high energy particles enter the earth's atmosphere or impinge on a vehicle, they interact and produce secondary particles. This process tends to cascade and is often called a shower process. The resulting radiation is difficult to measure since the secondary effects in any detector tend to mask the nature of the radiation field acting on the detector. The best estimate of the noise background due to this primary cosmic radiation comes from measurements made with equipment similar to the density sensing system. Figure 18 illustrates the background count rates that were measured by a cesium iodide crystal detector, 5 cm in diameter and 5 cm long. This detector was carried about a Deacon-Arrow sounding rocket (Ref. 5). This data illustrates the altitude dependence of the background showing the maximum at about 15 km altitude. It also illustrates little change in background above 30 km altitude. Figure 19 illustrates the differential spectra measured in the various altitude regions. These data serve as a useful reference for the higher energies, but do not show the background in the 100 keV region.

Numerous balloon flights have been conducted for solar flare study in which measurement of this softer energy component has been made at 30 km altitude. Peterson has a particularly useful discussion in reference 6 which illustrates the differential photon spectra measured in May 1961 at energies from 30 keV to 3 MeV. Also shown are the data from several other

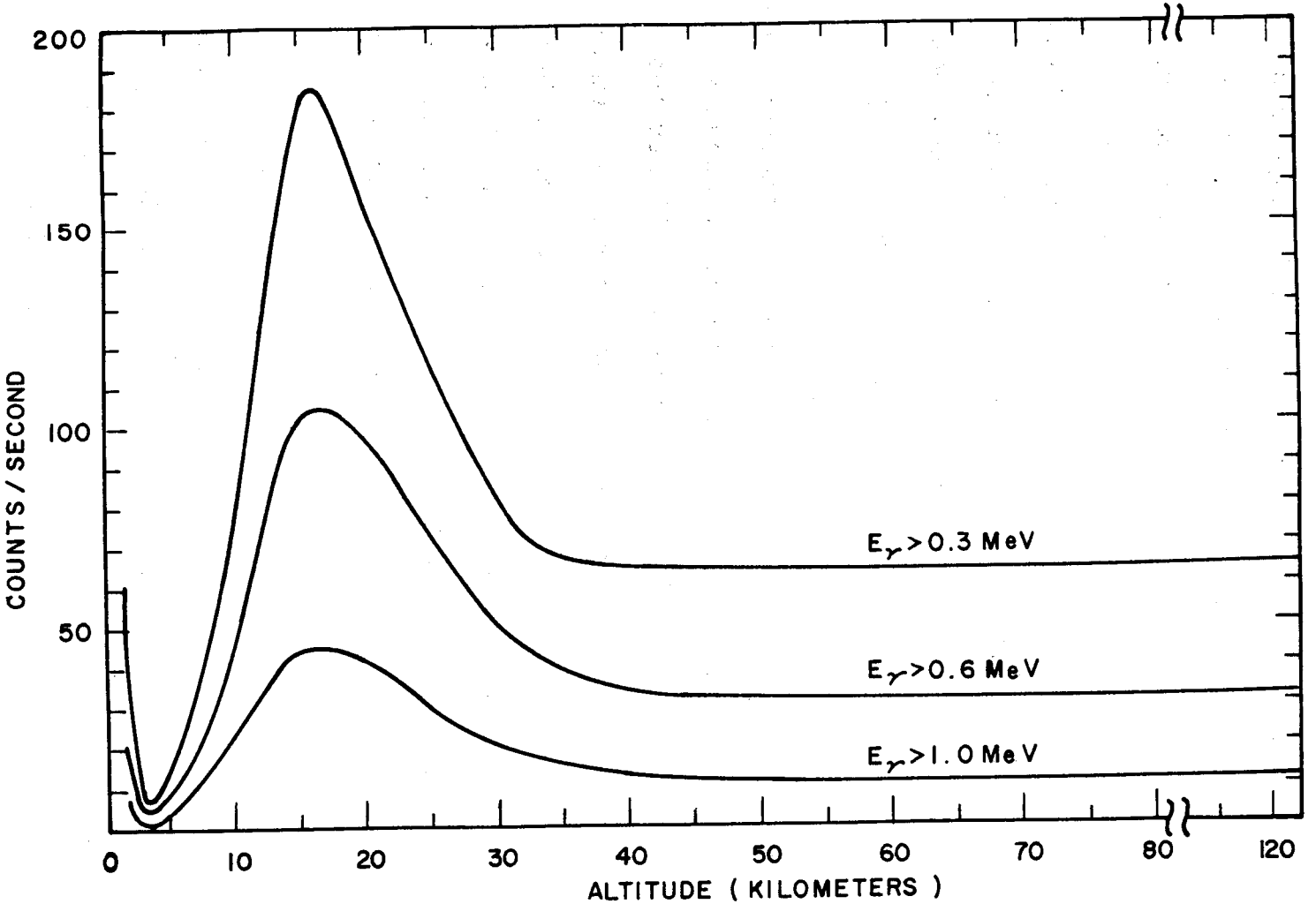


Figure 18 - Gamma Ray Background Measurements

From Deacon-Arrow Sounding Rocket

(Reference 5)

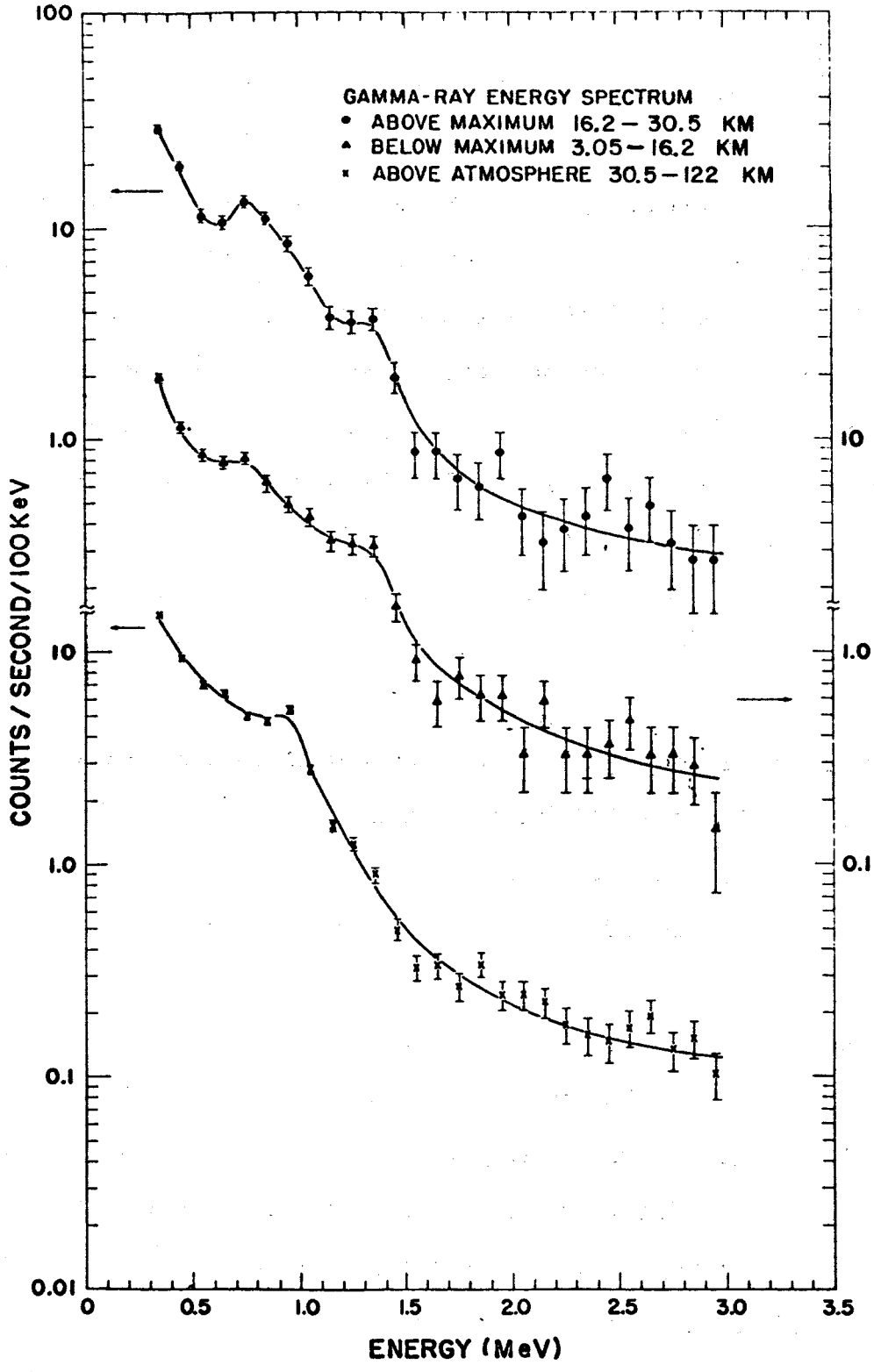


Figure 19 - Differential Spectra of Gamma Ray Background Measurements from Deacon-Arrow Sounding Rocket, (Ref 5)

investigators. This data is reproduced in figure 20. The integral spectra is shown in figure 21 for data from several other sources (ref. 5, 7, 8, 9, and 10). An approximation to these data is also shown drawn as the dashed line in figures 20 and 21. A spread of 10 to 1 about this line is also shown to encompass all the data points. Assuming a window setting in the payload of from 90 to 150 keV, the expected background flux above 90 keV is from 1.7 to 17 pulses per second per $cm^2$ and above 150 keV is 1.3 to 13 pulses per second per $cm^2$. The geometry factor $G_o$, for relating these fluxes to a particular detector dimension, is given in reference 6 as:

$$G_o = \frac{\pi}{4} LD \left(L + \frac{L}{2D}\right) \qquad (17)$$

where L is the detector thickness and D is the detector diameter. For the flight detector $G_o = 55\ cm^2$. The expected background fluxes are thus given as follows:

Expected Cosmic Background Count Rates

| | E > 90 keV | E > 150 keV | 90 < E < 150 keV |
|---|---|---|---|
| Minimum | 93.5 pps | 71.5 pps | 22 pps |
| Maximum | 935 pps | 715 pps | 220 pps |

The tungsten shielding near the detector limits the field of view of the detector significantly and would thus lower these estimates. However, high energy proton bombardment of the high Z material in the vicinity of the detector would tend to increase the background. It is felt that the above figures are a relatively accurate estimate of the cosmic contribution to the background.

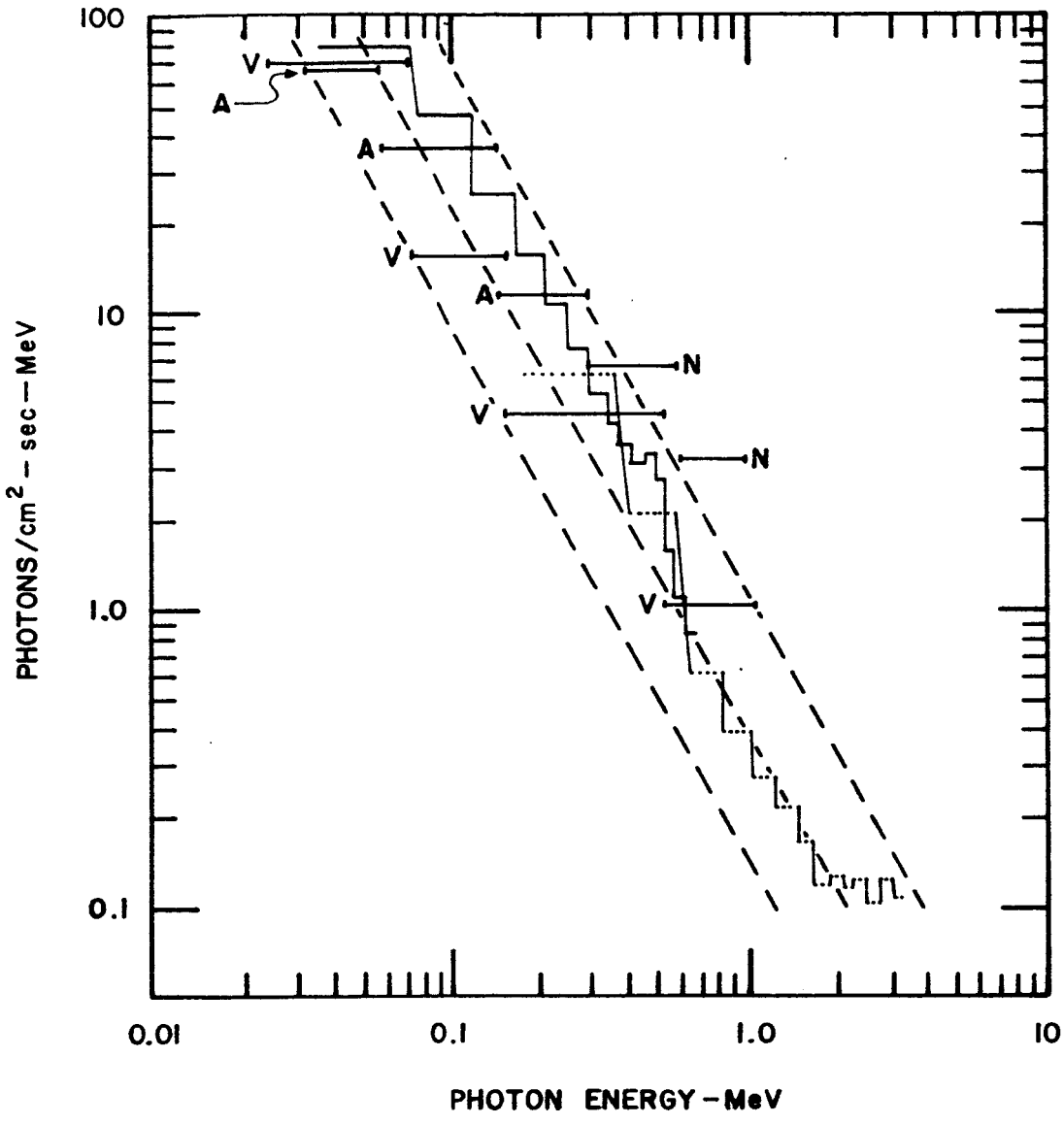


Figure 20 - Differential Photon Spectra Measured at the Top of the Atmosphere (Ref 6)

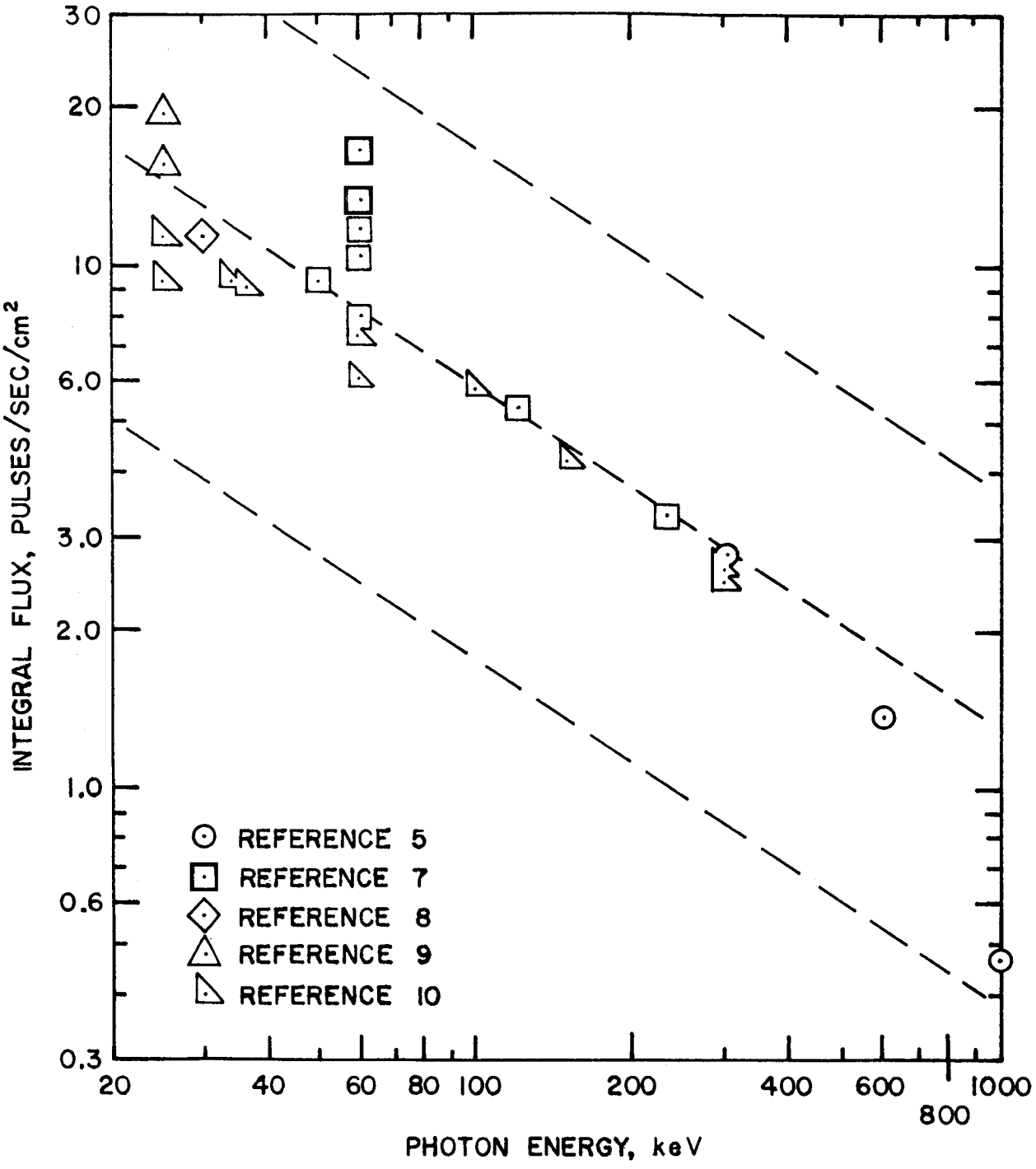


Figure 21 - Integral Photon Background Spectra Measured at the Top of the Atmosphere

Direct Transmission. - Direct transmission from the source to the detector is attenuated by the tungsten shield separating the two. This shield is 23.1 cm in length and greater than 17.7 $gm/cm^3$ density. The large amount of shielding is required to attenuate the high energy gammas from the source. The transmission expected, $I_t$, can be computed from the following relationship:

$$I_t = \frac{I_o a\ A_d}{4\pi\ r^2} De^{-\mu\rho x} \qquad (18)$$

where

$I_o$ = $1.85 \times 10^{12}$ disintegrations per second for 50 curie source

$a$ = 0.03 abundance of 2.185 MeV gammas

$A_D$ = 57 $cm^2$ detector area

$r$ = 43.0 cm separation of source and detector

$\mu\rho x = 0.043 \times 17.7 \times 23.1 = 17.6$

$D$ = 7.0 dose buildup factor for $\mu\rho x = 17.6$

From the above

$$I_t = 1.85 \times 10^{12} \times .03 \frac{57}{4\pi 43^2} 7e^{-17.6} = 21 \text{ pps}$$

giving a direct transmission of 21 pulses per second.

The contribution from the bremsstrahlung portion of the gamma spectrum is computed in appendix A and found to be small compared to this 21 pps countrate.

Multiple Skin Scatter. - As the gamma flux passes through the vehicle skin, a portion of the photons are scattered down the skin toward the detector. A portion of these undergo

secondary and ternary scattering events in the skin and ultimately reach the detector. Although the probability of these events occurring is extremely low, a finite number will reach the detector. Since the initial flux is very high, this number becomes significant. The number reaching the detector is calculated in appendix A, giving a multiple skin scatter count rate of 1450 pps. The high energy gammas produce the majority of this background. The low energy gammas are absorbed in the skin before they reach the detector.

Electrical noise. - The predominant electrical noise comes from the photomultiplier tube. Measurements of this noise on the operating payload have shown it to be small compared with radiation background at normal operating temperatures (a few pulses per second). The low level discriminator setting is adjusted to reject most of this photomultiplier tube noise.

## Shock Layer Effects

At high velocities, the density in the immediate vicinity of the vehicle is higher than the ambient atmosphere density. The scattering geometries of the sensor have been designed to minimize effects of this density increase by shielding against scattering events other than those at a distance from the vehicle. The source is shielded from radiating a conical volume of air with a 30° half angle. When the shock wave half cone angle is small, only scattering events outside the shock layer are detected. At Mach numbers below M = 5, the shock layer begins to extend into the scattering region, but the

density increase across the shock is decreasing. Figure 22 illustrates the results of a graphical analysis in which the error in density measurement due to the shock layer is determined. The maximum error is seen to be 0.4 percent.

## Calibration Techniques

Calibration of the sensor involves adjusting the discriminator levels and establishing the sensitivity of count rate to density. The discriminator level settings are established by measuring the detector output spectral response to the direct transmission from a small calibration source and the backscatter from the half curie test source in the flight position. These two spectra are illustrated in figure 23. The discriminator settings desired are those shown which encompass the air backscatter spectrum. Setting the discriminator levels is merely a matter of adjusting the levels until the count rates are equivalent to the integral of the calibrate spectrum above the low level setting and the upper level setting. The settings can be periodically checked by placing the calibration source in the same calibration position and monitoring the output count rates.

With the discriminator levels adjusted, the sensor is placed in a large altitude chamber with a test source of approximately 0.5 curie strength. The chamber is evacuated and count rates as a function of air density measured. With the chamber evacuated to a very low density, the wall scatter contribution is measured. This is then subtracted from the calibration points to give the air scatter calibration. The

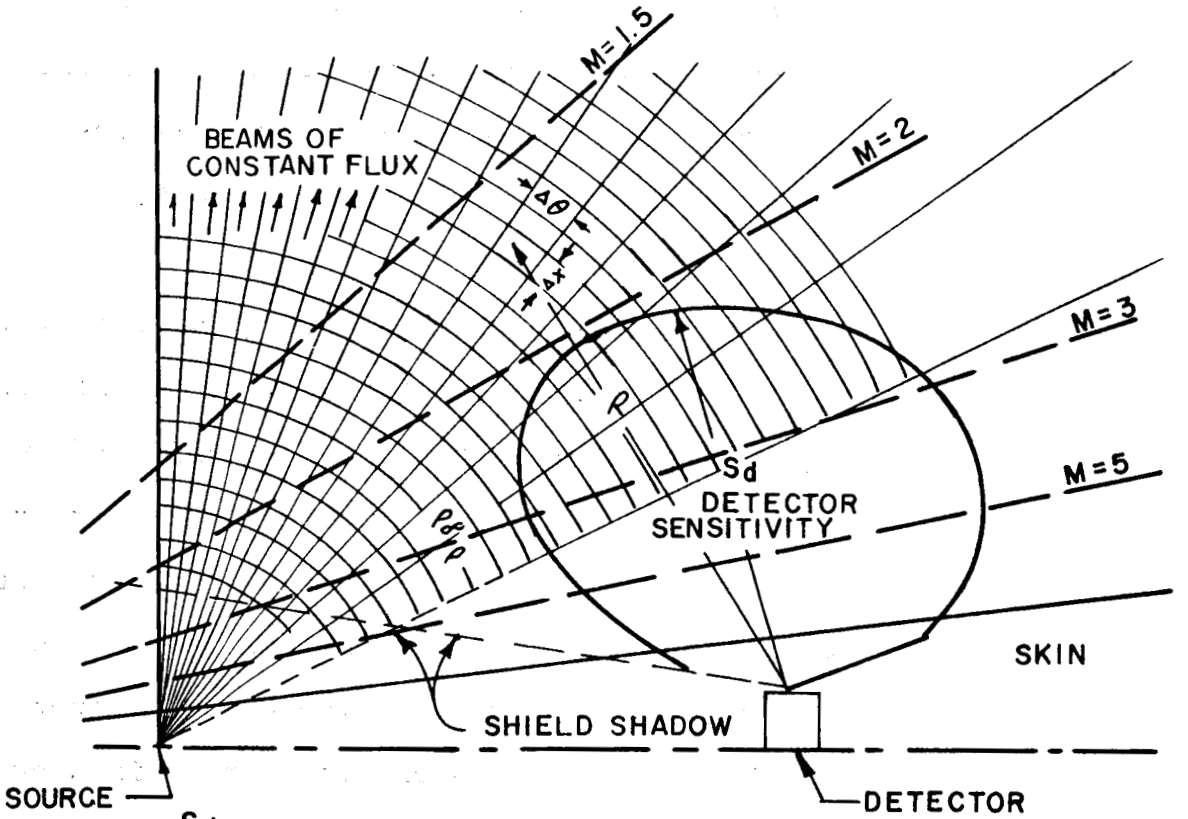


$$\varepsilon = \frac{\Sigma \frac{S_d}{R^2} \Delta x \Delta \theta_{\text{behind shock}}}{\Sigma \frac{S_d}{R^2} \Delta x \Delta \theta_{\text{total}}}$$

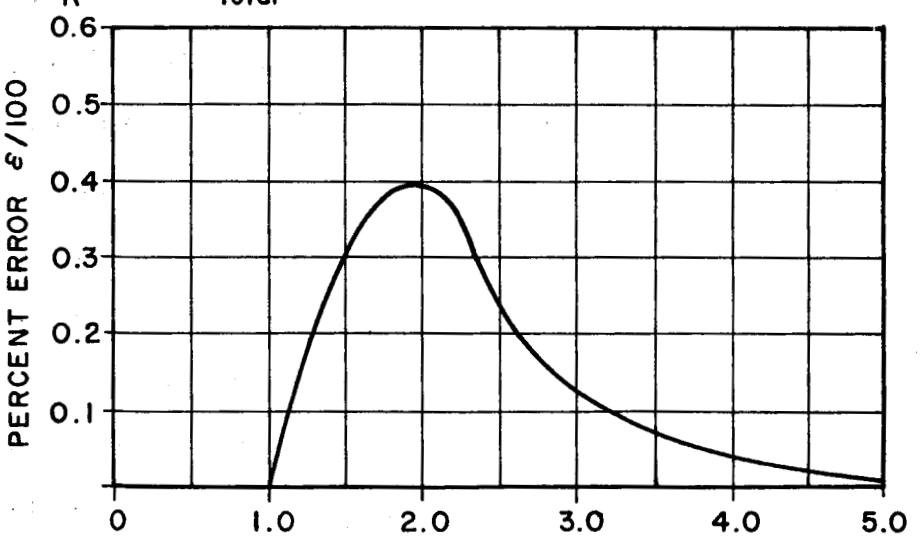


Figure 22 - Aerodynamic Effects on Sensor Accuracy

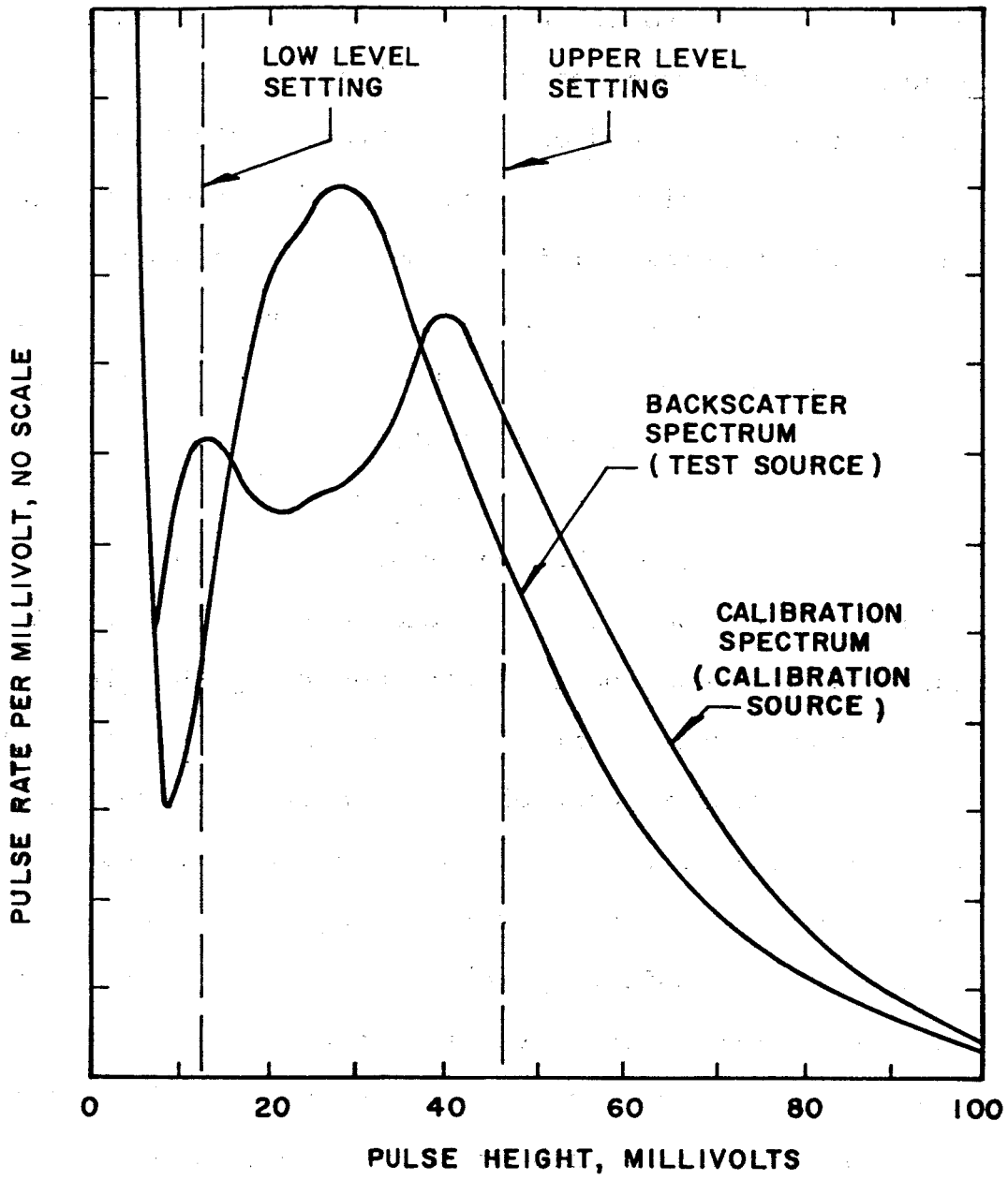


Figure 23 - Sensor Spectral Response

calibration also includes the ratio of strengths of the flight source and test source giving the flight calibration. Continual adjustment of this calibration constant is required to allow for source decay. Additional adjustment may be made to the flight calibration constant to correct for minor shifts in the electronics. This is done by performing a final check of the system with the calibration source in the calibration position. Any small shifts that are detected are used to adjust the system calibration constant.

## Density Measurement

Flight test of the sensor provides magnetic tape records of telemetered pulses and shield position as a function of time. Data reduction involves converting this information to pulse rate versus altitude for each shield position cycle. This conversion is done electronically using counters and printouts triggered by the shield position signal. The result is a tabulation of count rate averaged over one second intervals (one-half shield cycle) from the four pulse data channels (two detectors, upper level and lower level discriminator channels); time at the end of each one-second period; and vehicle altitude at each of these times. The upper level count rates are subtracted from the low level count rates, point for point, to give the count rate in the energy "window" as a function of altitude. This data is then analyzed to remove the background component and multiplied by the calibration constant to provide density as a function of altitude.

Several methods of data analysis have been considered to improve the statistical accuracy by averaging several data points. These are primarily curve-fitting techniques in which a curve is fitted to several data points and the values of background and density are determined which provide the best fit.

## PERFORMANCE TESTING

A comprehensive test program was completed on the flight hardware in preparation for the flight test. The testing included screening tests on all component parts, assurance testing of all assemblies, and flight acceptance testing of the completed payloads. All system elements were qualified prior to incorporation in the payload design. The environmental levels were established using flight history where available and dummy testing where the effects of mechanical interfaces were uncertain. A brief description of the tests performed and the testing levels employed on typical elements is given below.

### Component Screening

Screening tests were performed on system components such as resistors, capacitors, diodes, transistors, etc., before incorporation into modules and assemblies. Tests such as high temperature burn-in, over voltage, shock tests, leak test, etc., were performed to weed out marginal components, thus improving reliability.

### Qualification Testing

Environmental tests were performed on modules, subassemblies, and components whose designs had not previously been qualified to the required levels. Qualification levels were established as about 1.5 times the expected flight levels. A summary of the qualification environment is given below.

| | |
|---|---|
| Temperature. - | 150°F |
| Vacuum. - | 0 to 100 km altitude |

Vibration, Sine. - 1 sweep - 3 axes - 2.9 octaves per minute
20-90 cps .050 inch D.A. (44 sec)
90-2000 cps 20 g P (91 sec)

Shock, Longitudinal . - 90 g 11 msec 3 shocks

Shock, Transverse. - 45 g 11 msec 2 shocks each - ±2 axes

Acceleration, Longitudinal. - + 50 g -30 g

Acceleration, Transverse. - ± 10 g 2 axes

Assurance Testing

Environmental tests were performed on all modules, subassemblies, and components scheduled for use on the flight payloads including spares. Assurance levels were set approximately 10% higher than the anticipated flight levels. If specific resonances were known, the levels were increased to simulate these expected environments. A summary of the nominal assurance test levels is given below:

Temperature. - 130°F

Vacuum. - 0-100 km altitude

Vibration, Sine. - 1 sweep - 3 axes 5.8 octaves per minute
20-70 cps .030 inch D.A.
(18 seconds)
70-2000 cps 7.5 g P.
(50 seconds)

Shock, Longitudinal. - 65 g 11 msec 1 shock

Acceleration, Longitudinal. - +35 g -15 g

Additional vibration testing was performed on a mechanically equivalent structure to determine resonances. A severe resonance in the area of the detector was discovered and reduced using suitable pre-loading and damping materials. A spare detector assembly was vibration tested in the mechanically equivalent assembly to verify its ability to survive the remaining resonance conditions.

Flight Acceptance Testing

The completed payloads were subjected to the Flight Acceptance Tests. The environmental levels were those anticipated in flight and are summarized below.

| | |
|---|---|
| Temperature. - | Internal structure raised to 100°F |
| Vacuum. - | 0-100 km altitude |
| Vibration, Sine. - | 1 sweep - longitudinal axis |
| | 5.8 octaves per minute |
| | 70-2000 cps 5 g P. 50 sec |
| Vibration, Ramdon. - | 3 axes 60 seconds each |
| | 20-2000 cps 3.5 g rms flat spectrum |
| Shock, Longitudinal. - | +60 g 11 msec 1 shock |

Throughout these tests the operation of the payloads was monitored for failure or sensitivity shifts. One failure occurred during flight acceptance testing. This was a high voltage breakdown of a dc-dc converter under vacuum conditions. The failure was attributed to faulty insulation on a high voltage feedthrough. The converter was replaced with a spare unit and

the payload successfully passed a repeat vacuum test and all remaining tests. Some sensitivity shifts were noted during the tests, but none were severe.

## SYSTEM CALIBRATION

Final calibration of the two payloads was done in the 60-foot diameter altitude sphere at NASA-Langley Research Center. The following discussion pertains to payload LRC-1. This is the payload that was subsequently flight tested with the second, LRC-2, as a backup. The payload was suspended nose down in the center of the altitude sphere. The umbilicals were left attached to provide a means of switching the payloads from external to internal power and back. The test source was installed and the chamber was slowly evacuated. At several points during evacuation, the payload was switched to internal power and a telemeter record taken. The pressure and temperature inside the chambers were noted for each of the data points. This record was subsequently reduced to provide the scale factor of count rate versus density. A check of the sensor calibration was taken before and after the chamber run with the small calibration source in the calibration position. Also, a measure of the background level with no sources was taken before and after the chamber run.

The chamber calibration data is illustrated in figure 24 showing the count rate within the discriminator window divided by 16 as a function of chamber air density. Also shown is the background level measured before the source was installed. The slopes of the lines, $k_1$ and $k_2$, obtained from the data are 90.2 pps-$m^3$/kgm with the shield open and 30.0 pps-$m^3$/kgm with the shield closed.

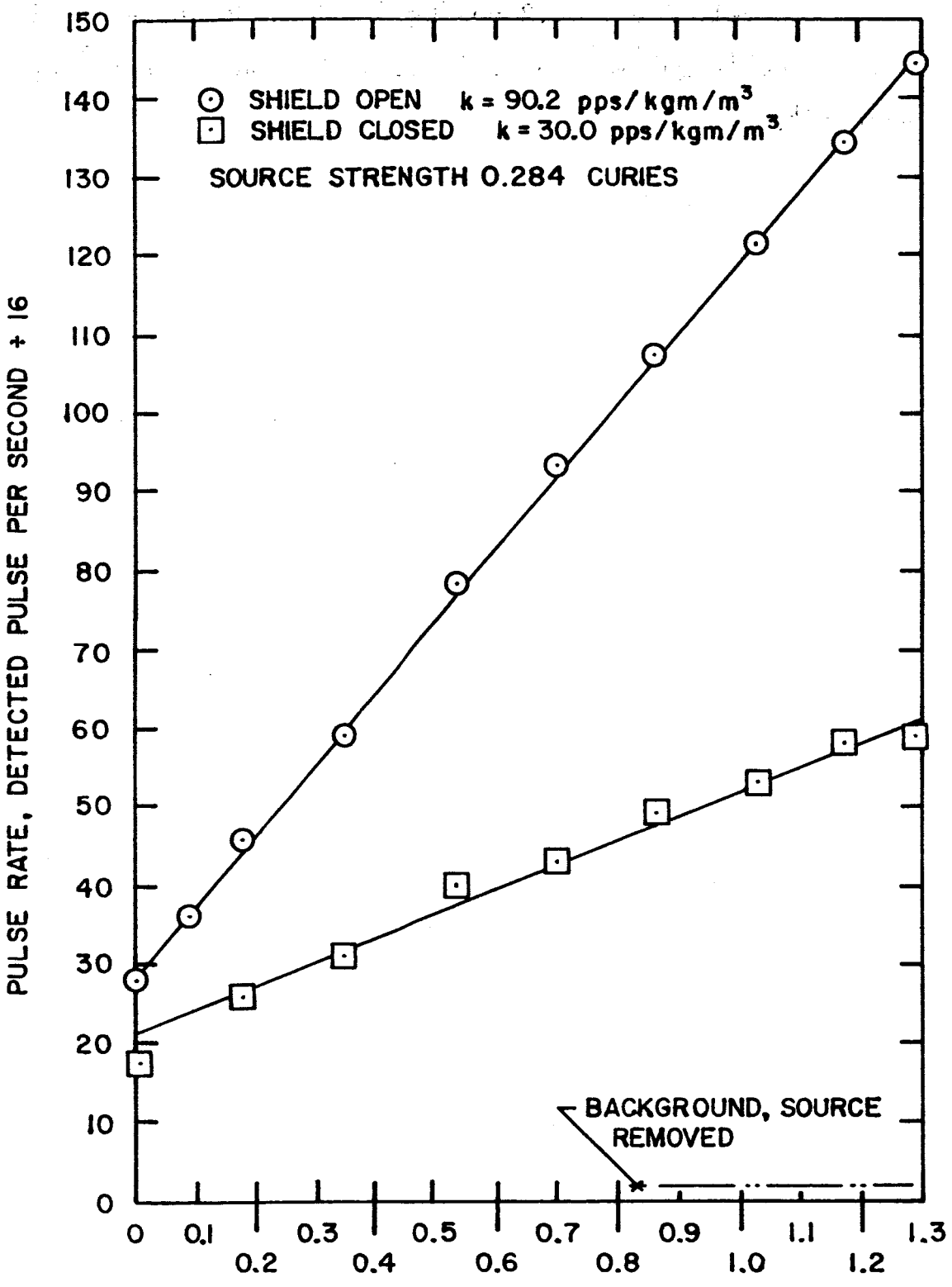


Figure 24 - Chamber Calibration Data for Payload LRC-1

This calibration constant agrees favorably with the mathematical model, i.e., 90.2 pps/kgm/$m^3$ ÷ 0.284 curies = 318 pulses-$sec^{-1}$-$kgm^{-1}$-$m^3$-$curie^{-1}$ versus 304 pulses-$sec^{-1}$-$kgm^{-1}$-$m^3$-$curie^{-1}$.

## FLIGHT TEST

Flight test of payload LRC-1 was conducted on 20 January 1966 from Wallops Island, Virginia. Figure 25 is a photograph of the assembled vehicle on the launcher ready for flight.

### Vehicle Performance

Launch occurred at 14:01:00 GMT after a smooth countdown. Second stage ignition occurred 20.6 seconds later. Both first and second stage boost acceleration profiles appeared normal. The modulating shield was held open by the boost accelerations, as expected. The apogee reached was 130.6 km. Impact occurred 348 seconds after launch at 73.82° longitude, 37.28° latitude. This was eight nautical miles from the predicted impact, well within the dispersion circle. The water depth at impact was 1,000 fathoms.

### Sensor Performance

All elements of the sensor performed properly throughout the flight. All pulse channels showed smooth changes with density throughout the flight. The accelerometer, temperature, and shield position indicator channels operated properly. The sensor internal temperature increased from 7.5°C at launch to 16°C at impact, showing the expected minimal aerodynamic heating.

### Supporting Tests

Several support measurements of the density profile were conducted before and after the sensor flight to provide density correlation. The performance of these flights is summarized below.

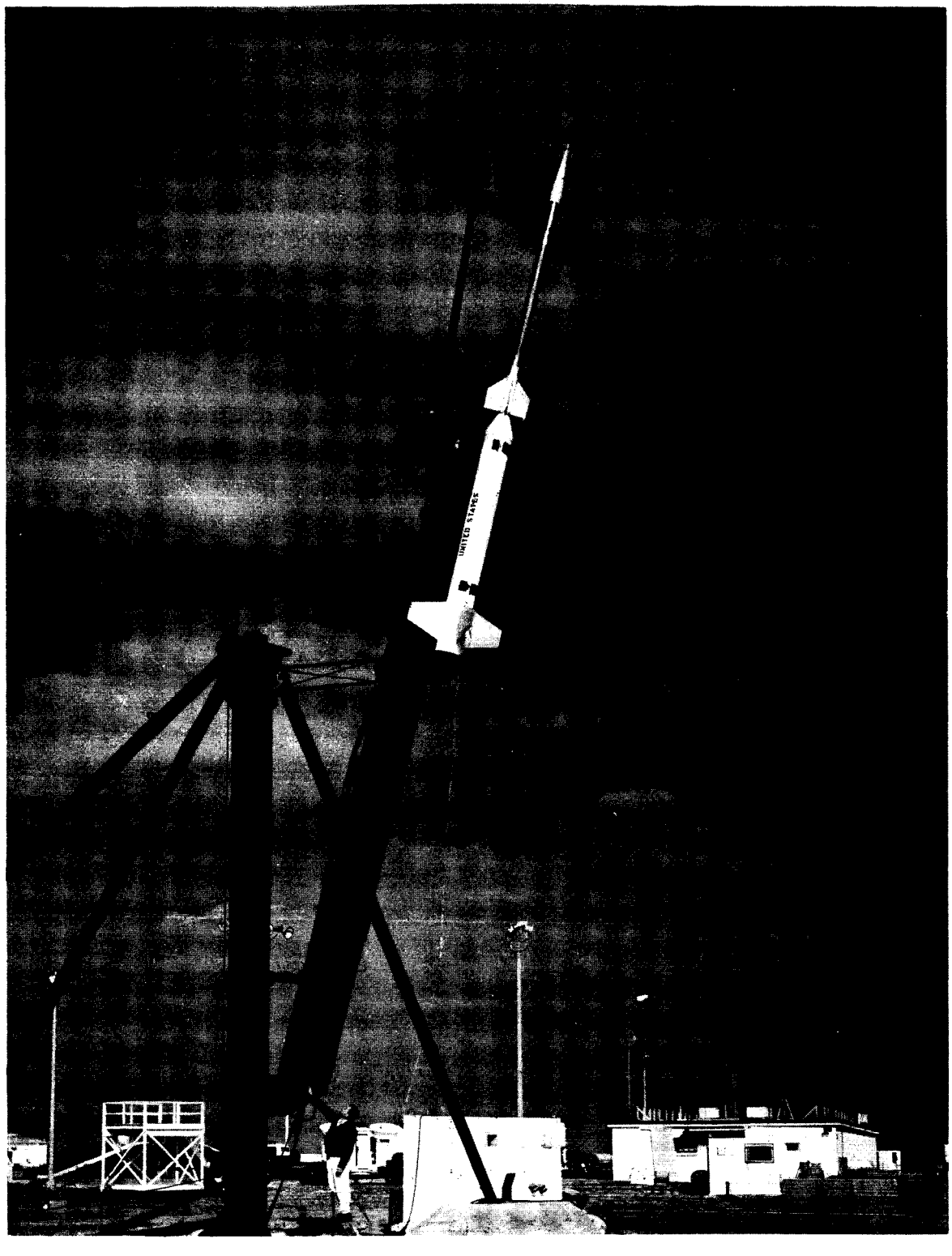


Figure 25 - Nike-Apache on Launcher

| Vehicle | Time (GMT) | Data Range (altitude) |
|---|---|---|
| Radiosonde Balloon | 11:15:00 | 0-31.8 km |
| Radiosonde Baloon | 18:00:00 | 0-29.3 km |
| Arcas Robin | | No data |
| Arcasonde | 15:43:00 | 20-46 km |

## Flight Test Data

The sensor pulse data is illustrated in figure 26, showing the pulse rate as a function of time with the shield open and closed. At low altitudes the pulse rates are high since the density is high. These pulse rates decrease as the density decreases until they reach the background level. At low altitudes where there is significant air scatter, the shield closed pulse rate is lower than the shield open pulse rate, as expected. At high altitude, where the signal is predominantly background, the shield closed pulse rate is higher than the shield open pulse rate. This unique behavior will be discussed in a later section. The altitude versus time profile is illustrated in figure 27.

The radiosonde and arcasonde data are shown plotted in figure 28, along with the 1962 IACO Standard Atmosphere. The density profile is seen to be slightly lower than the 1962 IACO Standard Atmosphere.

## Source Handling

The radioactive source used in this density measurement experiment was ~30 curies of Cerium-144. This source is of such a level as to require care in its handling and storage. Personnel at Giannini Controls Corporation were licensed by the U.S. Atomic

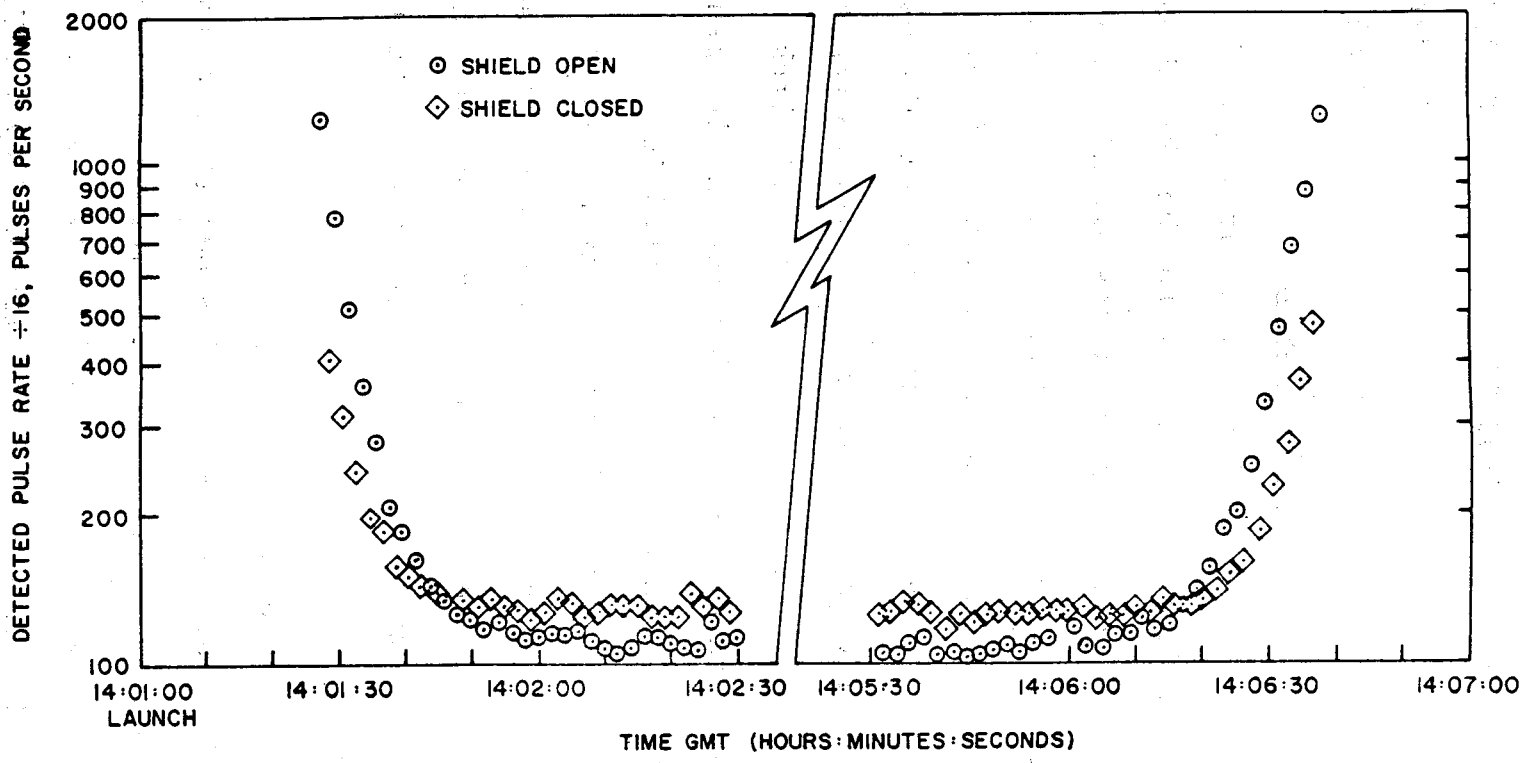


Figure 26 - Air Density Sensor Pulse Data

from 20 January 1966 Flight Test

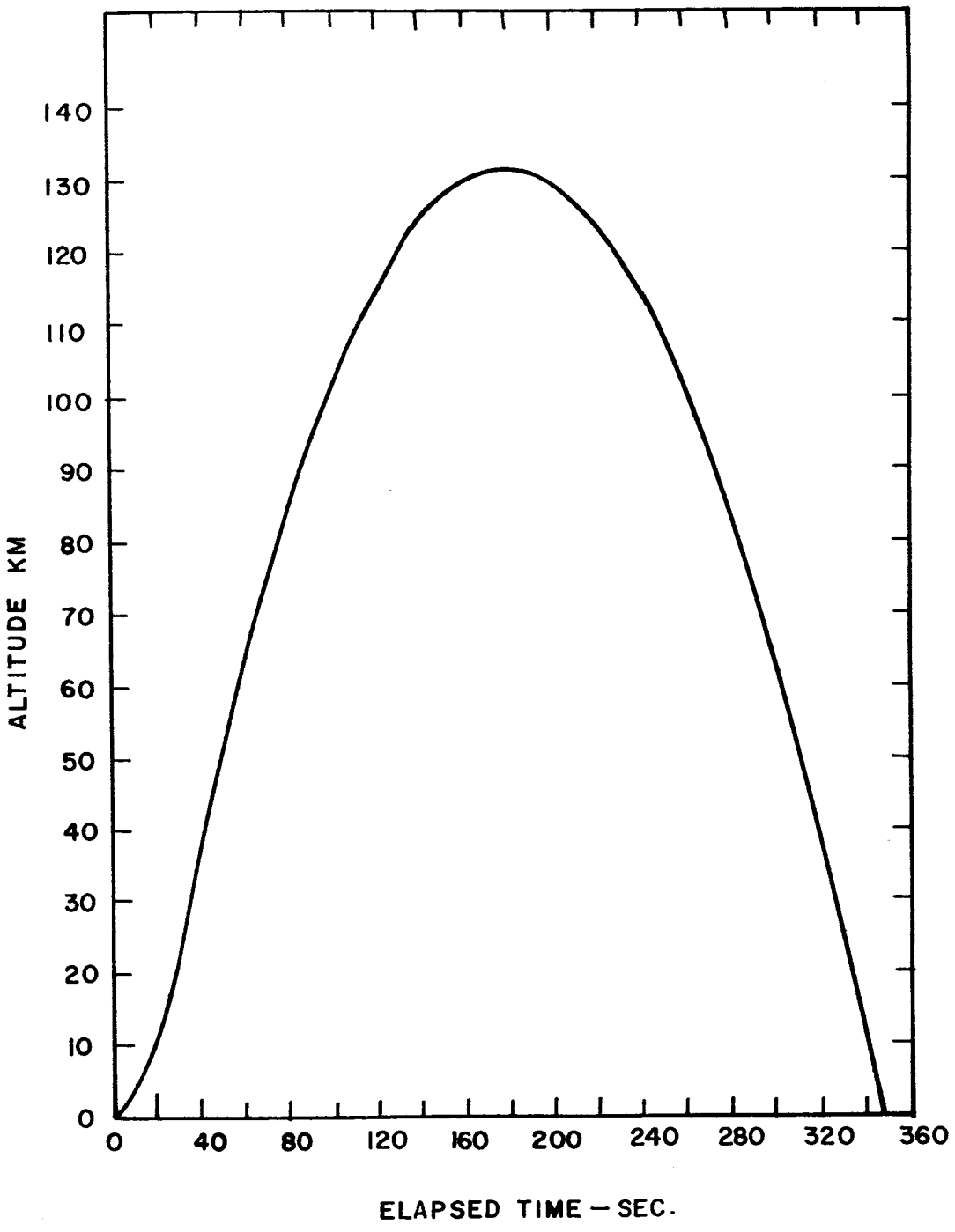


Figure 27 - Flight Trajectory

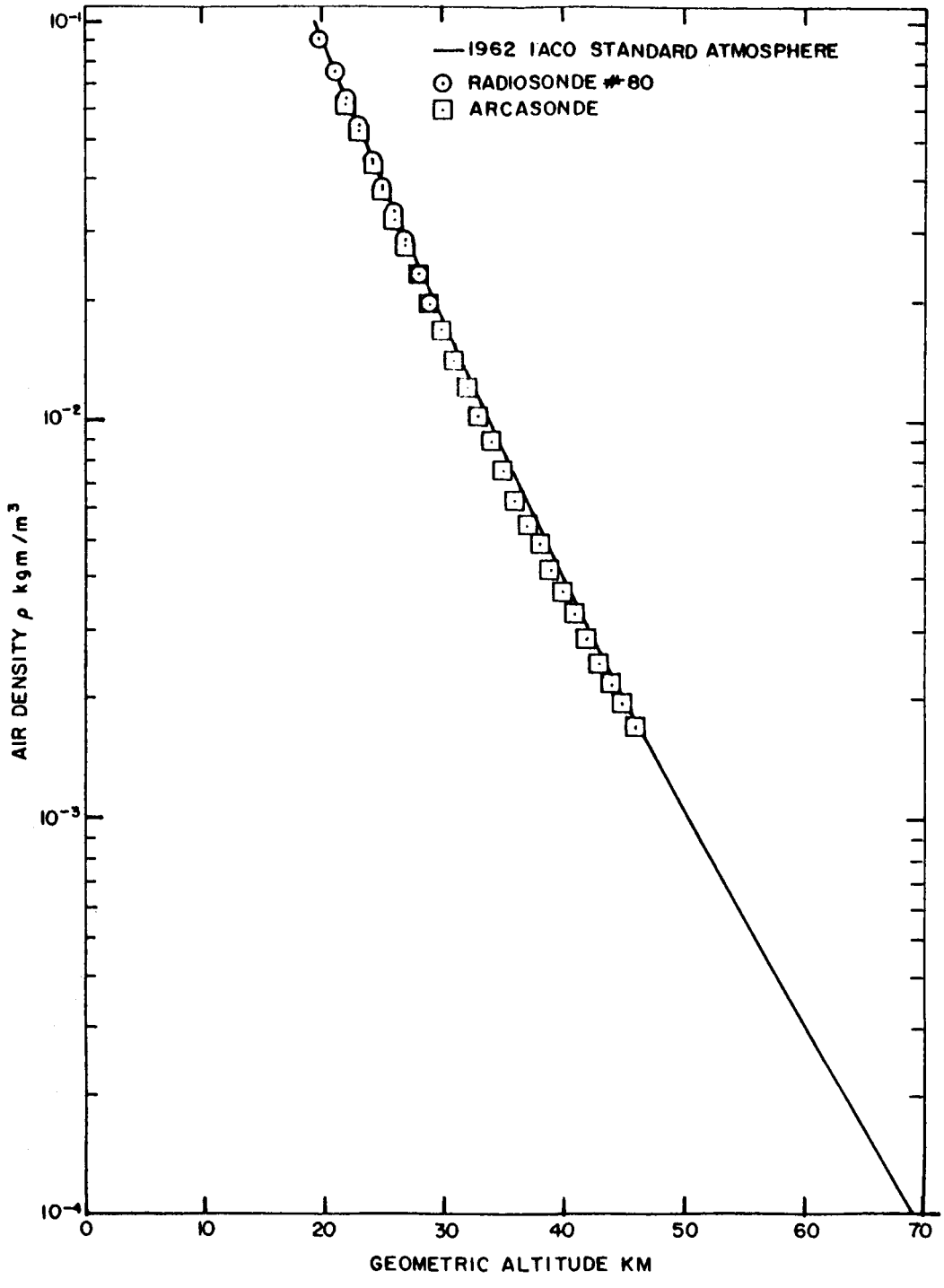


Figure 28 - Density Versus Altitude Profile,
Support Measurements for 20 January 1966 Flight Test

Energy Commission to possess and bear the responsibility for its proper and safe use. Procedures for safe handling and storage were established by Giannini Controls Corporation and approved by the AEC. Additional precautions were exercised by the Wallops Island range safety office, also licensed to store the source, to minimize the possibility of any dangerous incident. A brief summary of the major procedures followed is given below.

The Cerium-144 was doubly encapsulated in welded stainless steel capsules and leak tested by Oak Ridge National Laboratories. This source was mounted in the nose piece and shipped to Wallops Station in an approved shipping container for storage in a remote bunker.

On the launch date, the source in its shielding container was trucked to the launch site. After all preliminary checks of the payload were complete, the launch area was cleared to a distance of 100 feet. Two radioisotope technicians performed the installation illustrated in figure 29. The first technician unlocked and opened the shielded container and removed the source and nose tip with a pair of 6-foot tongs. The second technician gripped the nose tip with a specially designed 8-foot long pair of tongs and carried it a few steps to the nose of the vehicle. The Nike-Apache was mounted on the launcher in a horizontal position 6 feet above the ground. The second technician mounted a stepladder and lowered the source and handling tool into a V-shaped locating box propped at the nose of the vehicle. This box contained a lead liner providing some additional shielding.

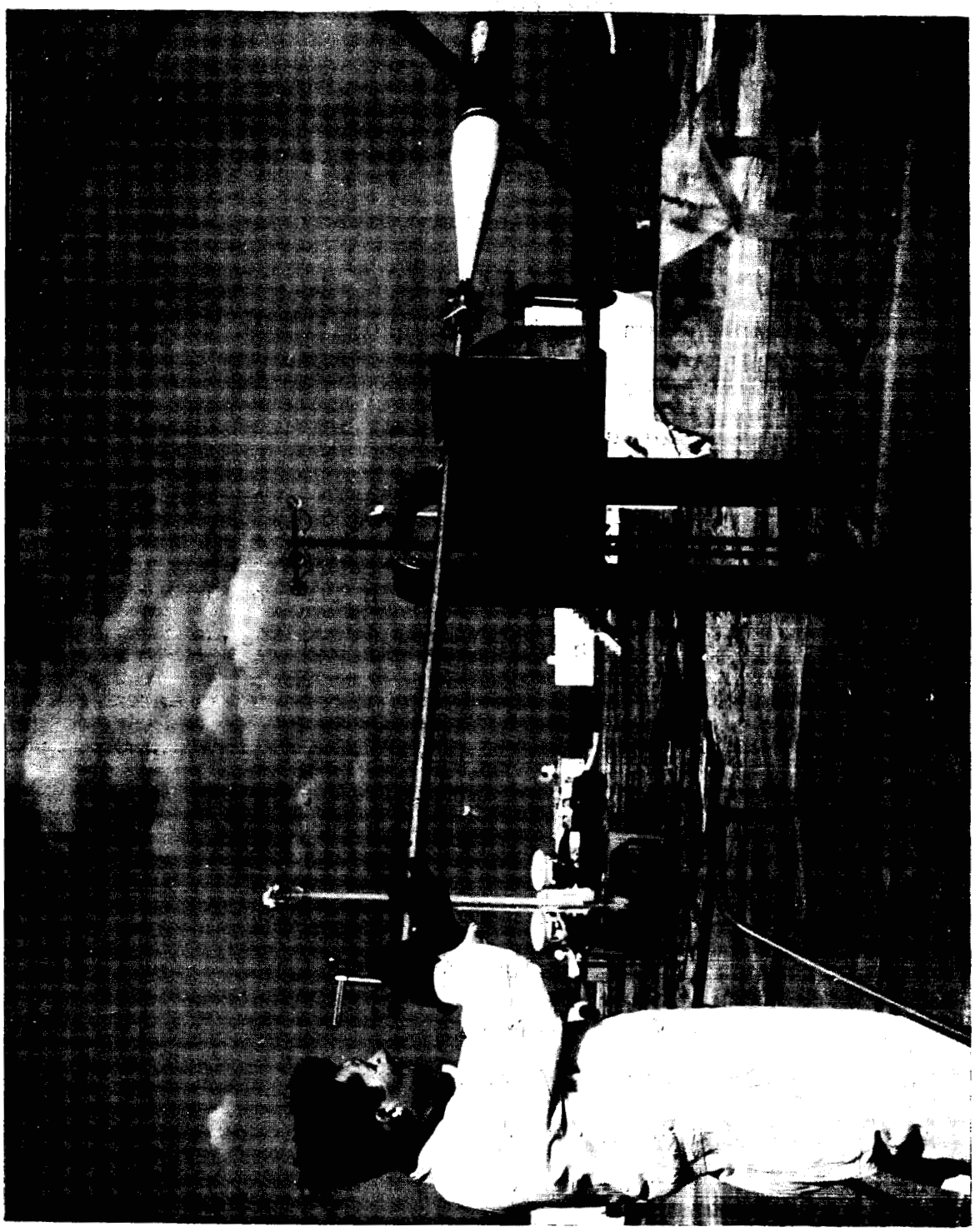

Figure 29 - Photograph Illustrating Source Installation

The source and nose piece were then inserted in the nose and screwed tight. The handling tool was released and the two technicians left the area. Pocket dosimeters and film badges monitored the dose received during the operations.

The launcher was then elevated remotely and the countdown proceeded to launch. The vehicle with source intact impacted at the desired range previously determined to have sufficient water depth to prevent accidental recovery and where the currents are such as to preclude the possibility of the source washing ashore.

In case of booster malfunction causing the payload to impact in the launch area or in shallow water, several recovery teams were available. Skin divers equipped with special sonar equipment and water-resistant geiger counters were located in recovery vessels. Several proven recovery methods were possible. Two helicopters were available to locate and guard the area of a possible land impact until the source could be recovered. None of these recovery operations was needed since the Nike-Apache boost system operated satisfactorily.

## FLIGHT TEST DATA ANALYSIS

This section describes the data analysis techniques used to obtain the measured density profile for comparison with the standard atmosphere profile and the measurements made by the radiosondes and arcasonde. Curve fitting techniques are discussed showing enhancement of the data at high altitudes.

### Description of the Data

A listing of the pulse data versus time and altitude is given in appendix B. The pulse count is that corresponding to the summation of pulses received during each shield half-cycle. The time given is the time at the end of each counting period. The altitude given is the vehicle altitude at the center of each counting period, one-half second earlier than the time shown. For each data point, the upper level pulses are subtracted from the lower level pulses from each detector. These are then summed giving the total counts from the two detectors where amplitude is between the lower and upper discriminator levels. All pulse data is referred to the telemeter output and thus is one-sixteenth the detected rates. This data of pulse rate versus altitude with the shield open and closed is shown in figures 30 and 31. At high altitudes, above 70 km, the pulse data is primarily background.

It is immediately evident that the background pulse rates are significantly higher than the anticipated cosmic background. The expected cosmic background rate after scaling by 16 is between 1.38 and 13.8 pulses per second. (See page 50). The

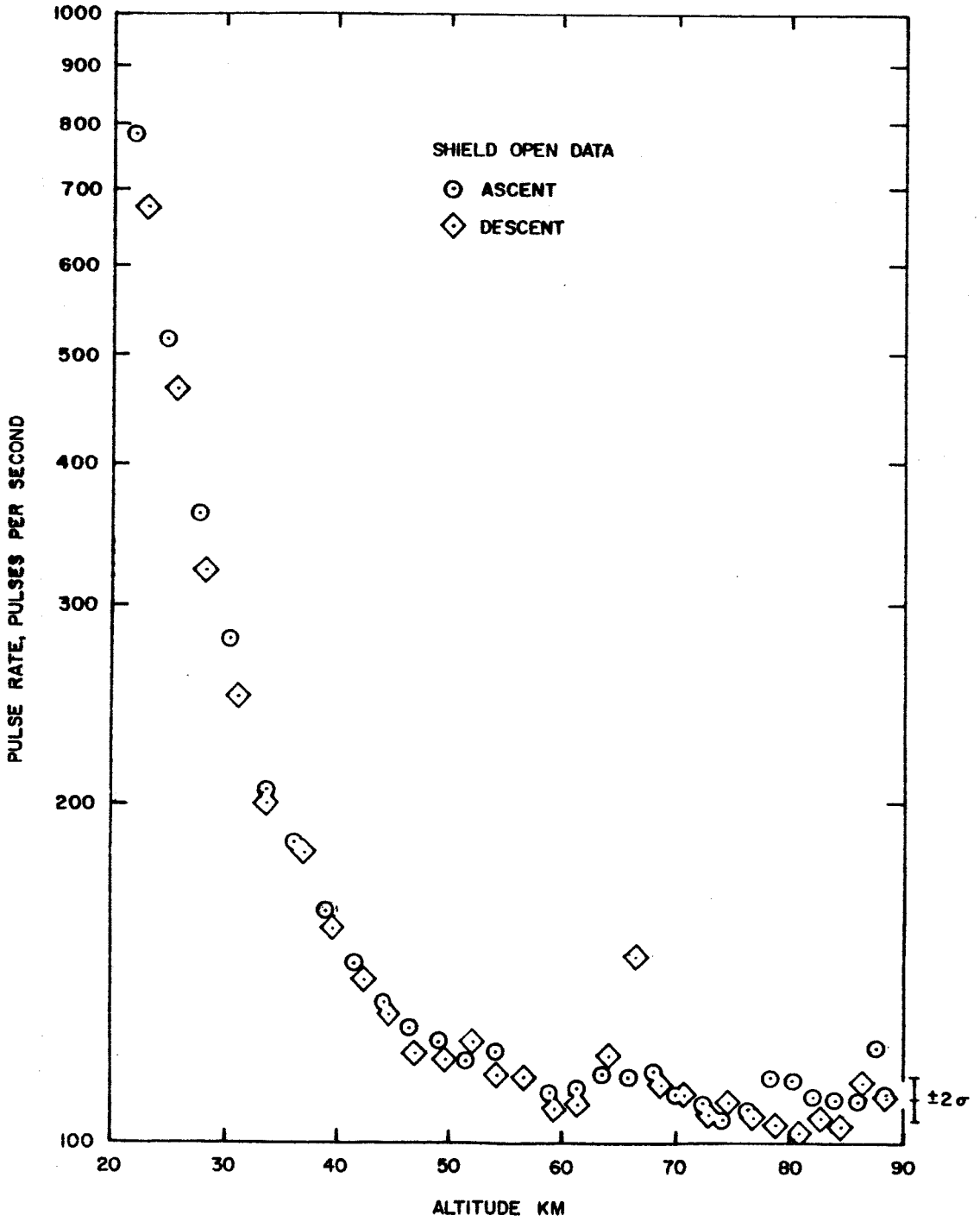


Figure 30 - Pulse Data Versus Altitude, Shield Open

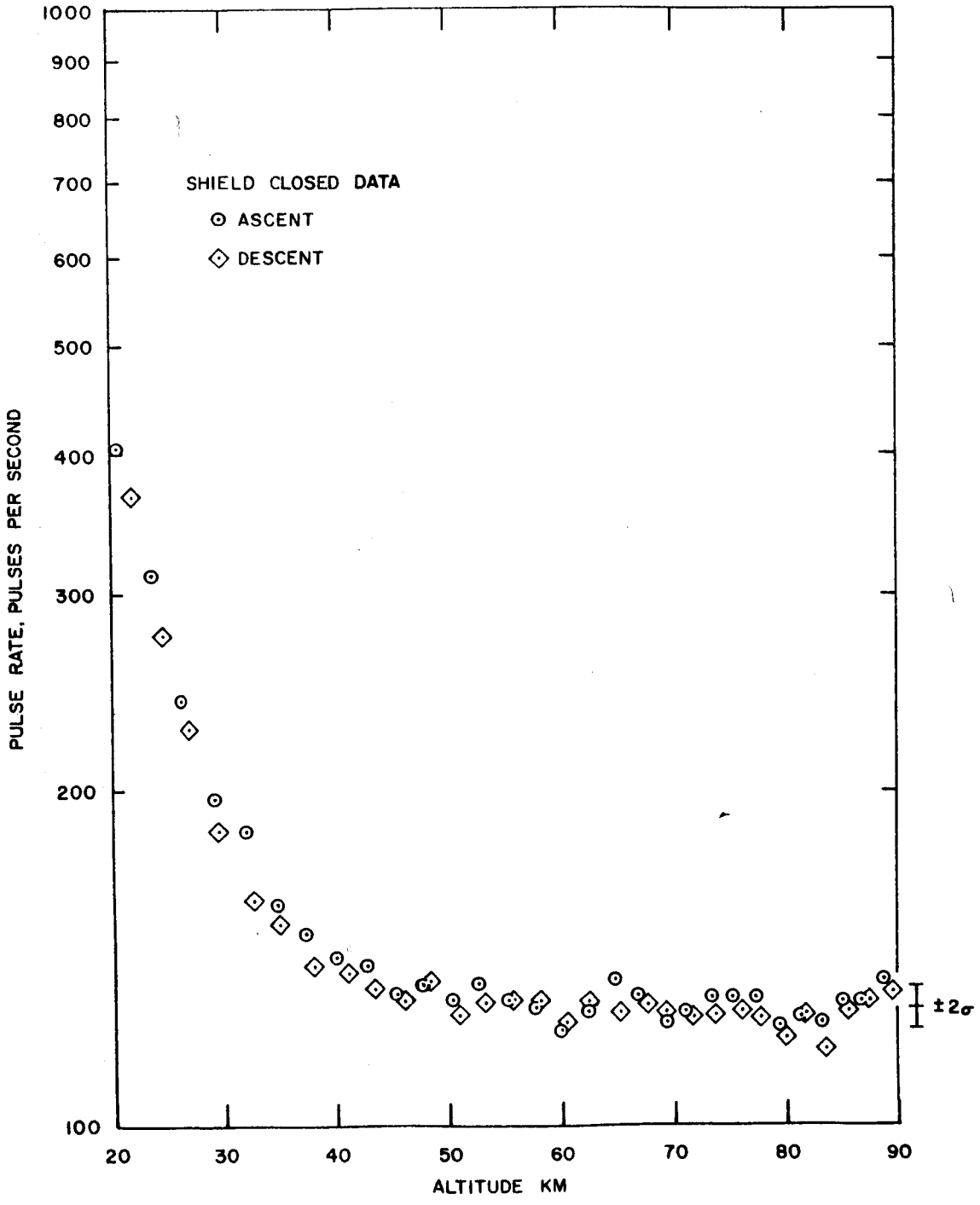


Figure 31 - Pulse Data Versus Altitude, Shield Closed

flight data shows more than 100 pulses per second background. Measured backgrounds at ground level without the source were approximately 3 pulses per second.

It is seen by comparing figures 30 and 31 that the background is lower with the shield open than with the shield closed by approximately 15 pulses per second. This indicates background sensitivity to the source and shield. Appendix A shows that this high background is the result of multiple scattering of high energy gammas from the source down the vehicle skin to the detector. These high energy gammas are primarily the bremsstrahlung radiation, some of which comes from beta interaction with the shield, thus explaining the higher background with the shield closed than with the shield open.

The air scattered count rate is determined by subtracting the background level. As a first cut, the background is assumed constant and equal to the average of background points from 70 to 90 km altitude. The pulse rate versus altitude with background subtracted is shown plotted in figures 32 and 33. The ratio of air scattered pulse rate with the shield open to that with the shield closed is seen to be 3.0:1. This ratio is lower than one might expect considering the attenuation properties of the tungsten shield to the 134 keV gammas. This ratio is justified, however, when the contribution of the high energy gammas are considered. (See appendix A) The statistical spread of the data points is seen to increase as the altitude increases and the air scattered pulse rate drops far below the background level.

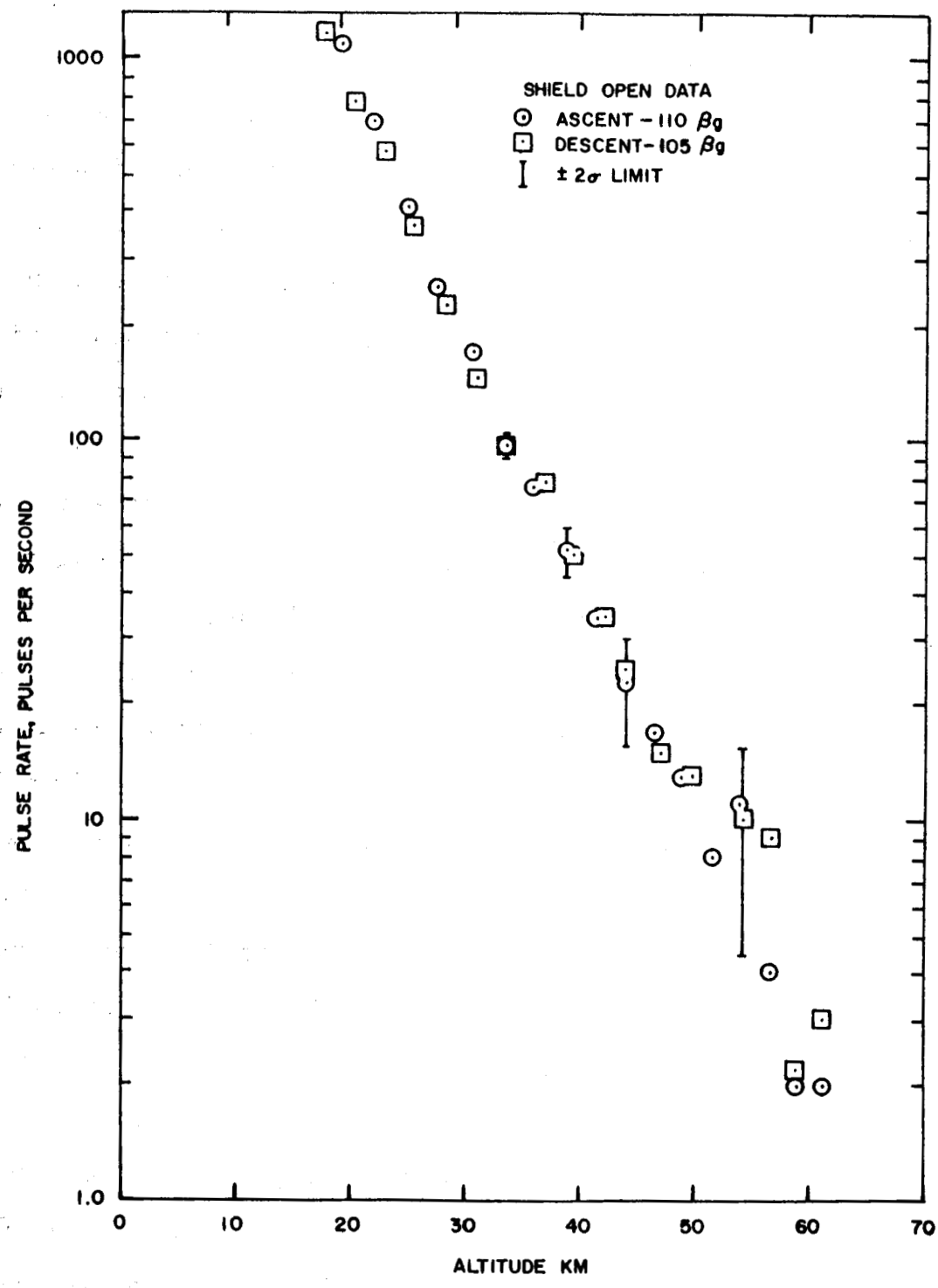


Figure 32 - Pulse Data Less Background Versus Altitude

Shield Open

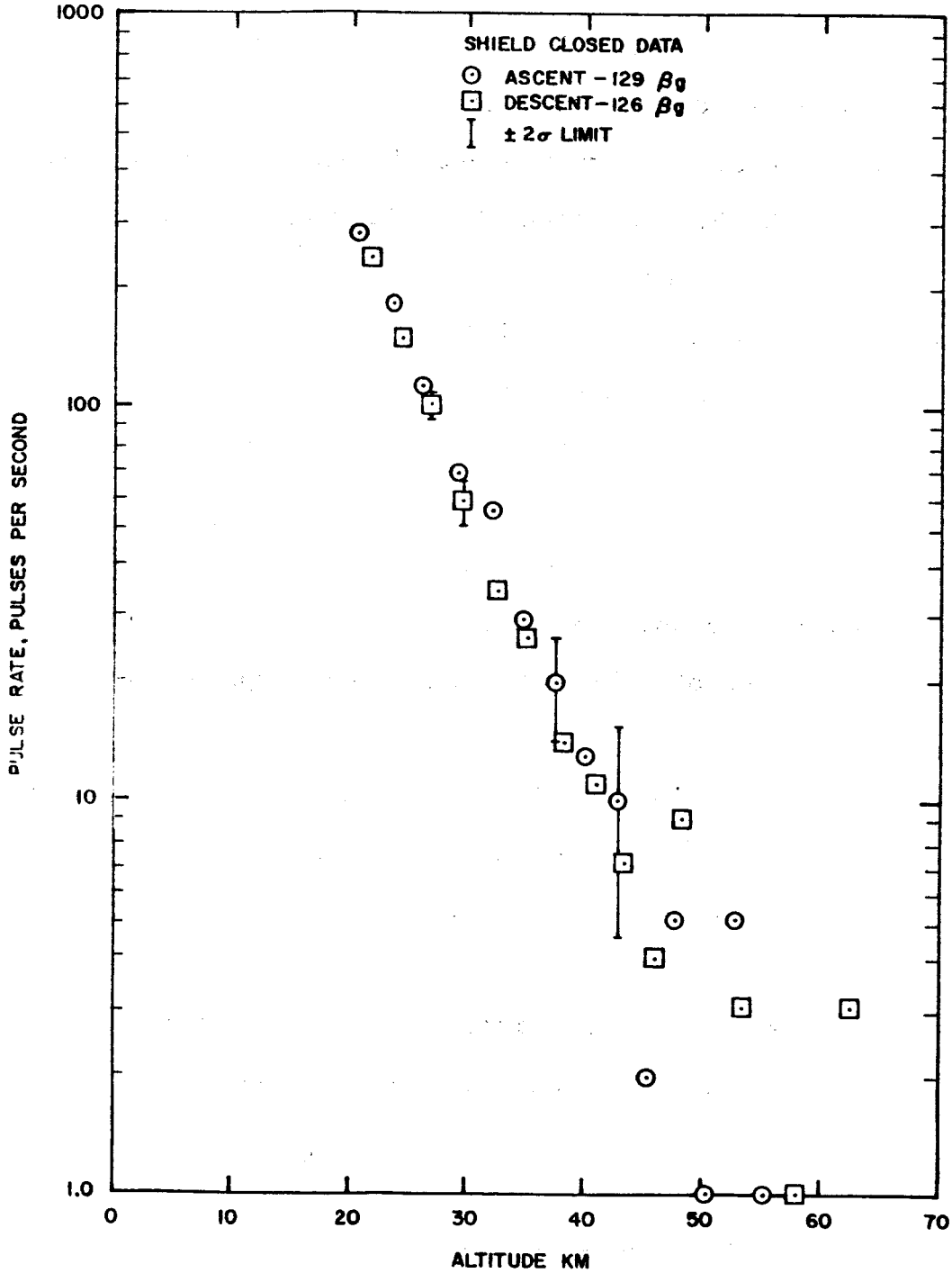


Figure 33 - Pulse Data Less Background Versus Altitude, Shield Closed

The theoretical ±2 sigma statistical limits are shown on a few data points.

## Density versus Altitude

The pulse data versus altitude is replotted in figure 34 with backgrounds subtracted and the shield closed data points multiplied by 3.0 to match the shield open calibration. The pulse rates are multiplied by the calibration factor (see page 66) to provide the measured density. The density profile established by the radiosonde and Arcasonde data is shown as a solid line and the 1962 IACO Standard Atmosphere profile shown as a dashed line at the higher altitudes. The agreement is excellent.

## Data Enhancement

Several techniques of curve fitting have been considered in order to smooth the data points and improve accuracy at high altitudes.

One method is described below which fits an exponential curve to groups of 10 consecutive data points using the "Method of Least Squares". The data of figure 34 is used for this analysis.

Over small altitude increments, the air density profile may be described mathematically as follows:

$$\rho_i = \rho_o \, e^{-\beta(h_i - h_o)} \tag{19}$$

where $\rho_o$ is the density at altitude $h_o$, $\rho_i$ is the density at altitude $h_i$, and $\beta$ is a constant. Let $\rho_i'$ be the data point value at altitude $h_i$ and let $v_i$ be the residual difference between the actual data point and estimated point.

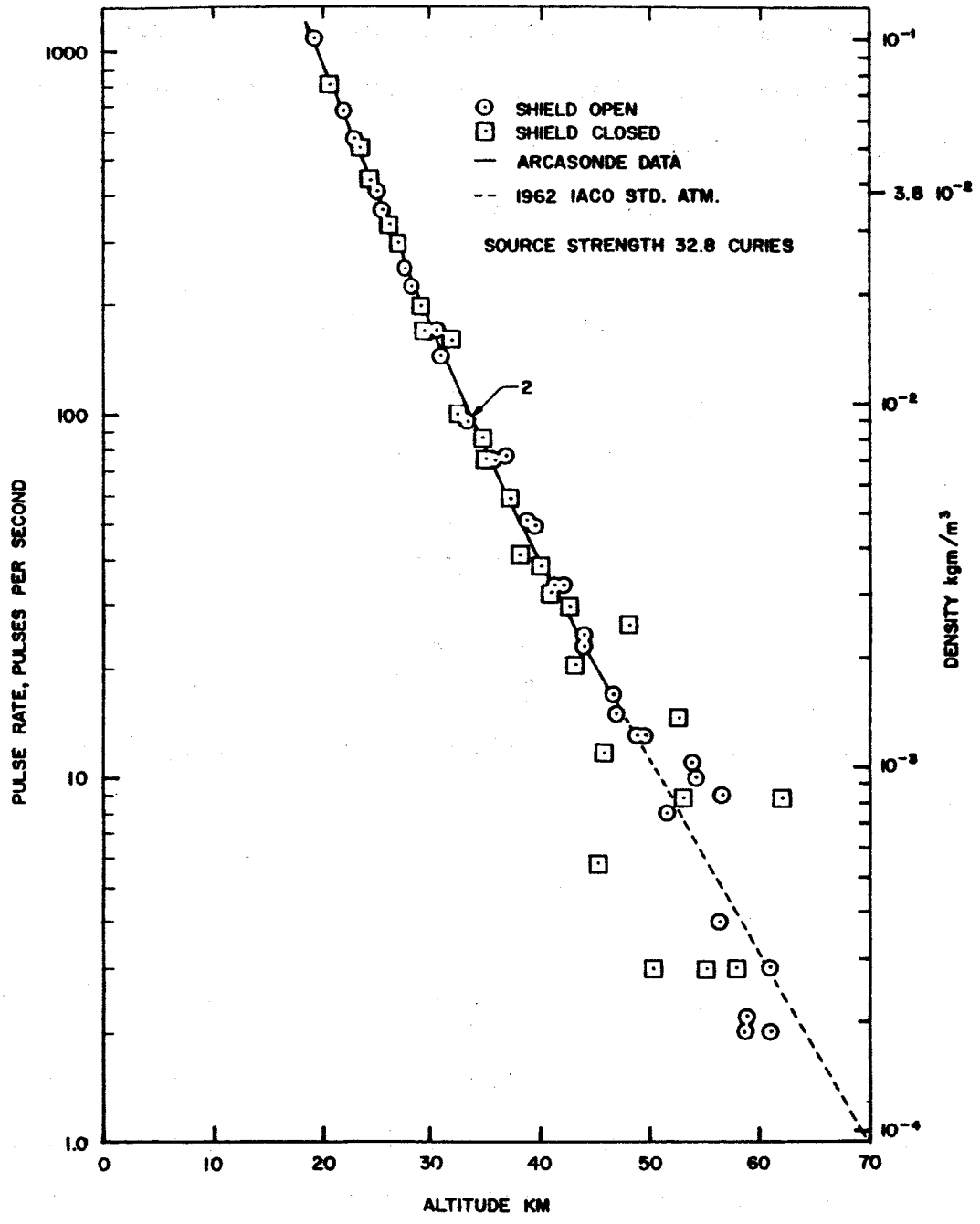


Figure 34 - Measured Density Versus Altitude

$$v_i = \rho_i - \rho_i' \tag{20}$$

The method of least squares will be used to find a value of $\rho_o$ and $\beta$ such that the sum of the squares of the residuals is minimum. In order to linearize the expression, equations 19 and 20 are modified to

$$\ln \rho_i = \ln\rho_o - \beta(h_i - h_o) \tag{21}$$

and

$$v_i = \ln\rho_i - \ln\rho_o' = \ln\rho_o - \beta(h_i - h_o) - \ln\rho_i' \tag{22}$$

The value of $\ln\rho_o$ and $\beta$ are determined by solution of the following normal equations:

$$\sum_1^n \frac{\partial v_i}{\partial \ln\rho_o} = 0 \tag{23a}$$

$$\sum_1^n v_i \frac{\partial v_i}{\partial \beta} = 0 \tag{23b}$$

Taking the indicated partials and substituting gives the following:

$$\ln\rho_o \sum_1^n 1 - \beta \sum_1^n (h_i - h_o) = \sum_1^n \ln\rho_i' \tag{24a}$$

$$\ln\rho_o \sum_1^n (h_i - h_o) - \beta \sum_1^n (h_i - h_o)^2 = \sum_1^n (h_i - h_o) \ln\rho_i' \tag{24b}$$

The value of $\rho_o$ at the highest altitude of each 10 data point segments was determined, giving the data points of figure 35.

Several other curve fitting techniques have been considered suitable for machine analysis and are discussed in the next section.

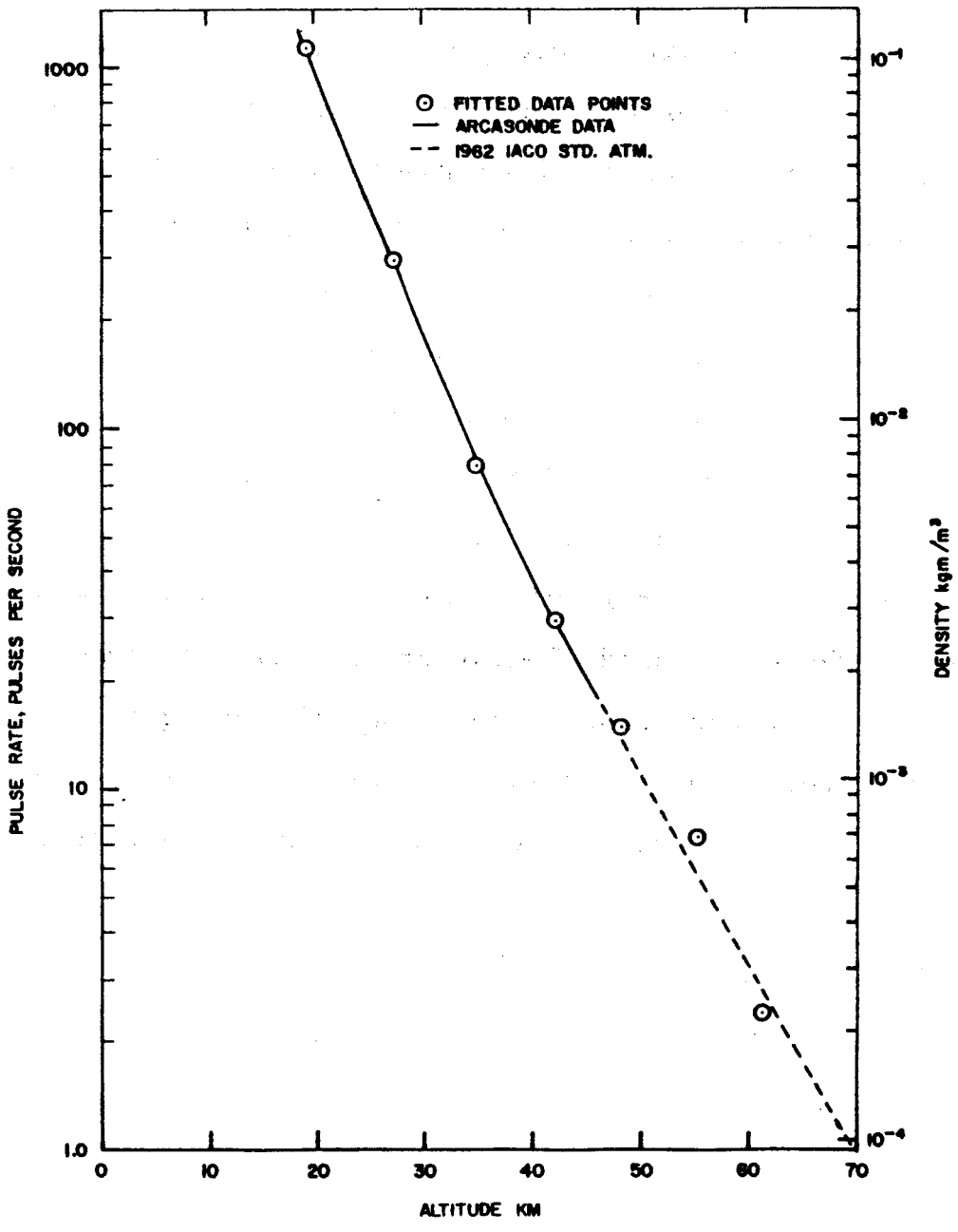


Figure 35 - Density Versus Altitude,

10 Point Curve Fit

## Background

The basic reason for including the modulating shield in the system was to provide a background measurement. Unfortunately, the attenuation provided by the shield was low so that except at very high altitudes the background is buried in the air scatter signal. Also, the change in background level with the shield position adds uncertainty to the background measurement. It is felt that the background is coming from the source via multiple scattering through the skin and the value at high altitude is indicative of what would be measured at lower altitudes. Searching for variations in the cosmic portion of the background does not promise much fruitful information. Appendix A discusses in detail the background element created by the source.

It is interesting to note that the background levels measured on the 17 December 1964 flight and the 20 January 1966 flight are different by the ratio of source strengths. This further substantiates the conclusion that the high background level is coming from the source.

## ERROR ANALYSIS

This error analysis applies to the 20 January 1966 flight test data obtained with payload LRC-1. Table I summarizes the sources of error and their effect on system performance.

### Calibration Errors

The calibration data may be represented by the following equation:

$$I_d = k\rho + I_w + I_b \tag{25}$$

where $I_d$ is the count rate detected at each calibration point, k is the constant of proportionality, $\rho$ is the air density in the chamber, $I_w$ is the scatter from the chamber walls, and $I_b$ is the background radiation level. Density is determined by pressure and temperature measurements as:

$$\rho = \rho_s \frac{P}{P} \frac{T_s}{T} \tag{26}$$

where $T_s$ is standard temperature, $P_s$ is standard pressure, and $\rho_s$ is standard density.

The flight calibration, K, is the product of the chamber proportionality constant, k; the ratio of the flight source strength, $I_{of}$, to the test source strength, $I_{ot}$, used in the chamber; and the stability of the sensor $S_d$.

$$K = k \frac{I_{of}}{I_{ot}} S_d \tag{27}$$

Combining equations (25), 26), and (27) and solving for K gives:

$$K = \frac{I_{ot}\ S_d\ P_s\ T}{I_{of}\ \rho_s\ P\ T_s} (I_d - I_w - I_b) \tag{28}$$

TABLE I

ERROR SUMMARY AT 20 km ALTITUDE

| Error Source | | Error Magnitude | RSS Total | |
|---|---|---|---|---|
| Calibration | | | | |
| Test Source Strength | $\frac{\Delta I_{ot}}{I_{ot}}$ | ±0.025 | | |
| Flight Source Strength | $\frac{\Delta I_{of}}{I_{of}}$ | ±0.025 | | |
| Sensor Stability | $\frac{\Delta S}{S}$ | ±0.064 | | |
| Chamber Pressure | $\frac{\Delta P}{P}$ | ±0.01 | | |
| Chamber Temperature | $\frac{\Delta T}{T}$ | ±0.01 | | |
| Statistical Variation, Maximum Density | $\frac{\Delta I_d}{I_d - I_w - I_b}$ | ±0.0047 | | |
| Statistical Variation, Minimum Density | $\frac{\Delta (I_w - I_b)}{I_d - I_w - I_b}$ | ±0.0031 | | |
| Total Calibration Error | $\frac{\Delta K}{K}$ | | 0.075 | |

TABLE I. - Continued

ERROR SUMMARY AT 20 km ALTITUDE

| Error Source | | Error Magnitude | RSS Total | |
|---|---|---|---|---|
| Flight Test | | | | |
| Shock Wave Effects | $\frac{\Delta S_s}{S_s}$ | ±0.004 | | |
| Stability Through Flight | $\frac{\Delta S_d}{S_d}$ | ±0.01 | | |
| Statistical Fluctuation* | $\frac{\Delta N_d}{\tau (I_d - I_b)}$ | ±0.0095 | | |
| Background* | $\frac{\Delta I_d}{I_d - I_b}$ | ±0.0006 | | |
| Shield Modulator Timing* | $\left(\frac{I_d}{I_d - I_b}\right)\frac{\Delta\tau}{\tau}$ | ±0.017 | | |
| Ablation Effect | $\frac{\Delta S_d}{S_d}$ | ±0.02 | | |
| Pulse Resolution* | $\frac{\Delta N_d}{\tau (I_d - I_s)}$ | ±0.0006 | | |
| Velocity Error | - | ±0.0008 | | |
| Total Flight Test Error | | | ±0.031 | |
| TOTAL DENSITY MEASUREMENT ERROR | | | | ±0.082 |

* Altitude dependent errors

Taking the logarithm of equation 28 gives

$$\ln K = \ln P_s - \ln\rho_s - \ln T_s + \ln I_{ot} - \ln I_{of} + \ln S_d - \ln \rho + \ln T + \ln (I_d - I_w - I_b) \quad (29)$$

Taking the derivative ot equation (29) gives

$$\frac{dK}{K} = \frac{d\rho_s}{\rho_s} - \frac{d\rho_s}{\rho_s} - \frac{dT_s}{T_3} + \frac{dI_{ot}}{I_{ot}} - \frac{dI_{of}}{I_{of}} + \frac{dS_d}{S_d} - \frac{d\rho}{\rho} + \frac{dT}{T} + \frac{dI_d}{I_d - I_w - I_b} - \frac{d(I_w + I_b)}{I_d - I_w - Ib} \quad (30)$$

Substituting small changes for the differential values of the error sources and zero for the constants gives

$$\frac{\Delta K}{K} = \frac{\Delta I_{ot}}{I_{ot}} - \frac{\Delta I_{of}}{I_{of}} + \frac{\Delta S_d}{S_d} - \frac{\Delta P}{P} + \frac{\Delta I_d}{I_d - I_w - I_b} - \frac{\Delta (I_w + I_b)}{I_d - I_w - I_b} \quad (31)$$

The source strengths are each known to be within ±5% two sigma of the stated value from manufacturer's data. The one sigma value of $\frac{\Delta I_{ot}}{I_{ot}}$ and $\frac{\Delta I_{of}}{I_{of}}$ are thus ±0.025.

The sensor stability, $\frac{\Delta S_d}{S_d}$, was estimated from measurements of count rate shifts during system Flight Acceptance Testing. The maximum shift of the poorest channel was considered a two sigma deviation from the nominal. For example, if one channel drifted a maximum of +4% through a longitudinal vibration run, the two sigma error band for that particular environment was considered ±4%. Each error band for all environmental tests was then summed on an RSS basis. The temperature band was established by comparing temperature ground test data and the measured flight temperatures, and using the maximum drift from the start of the

temperature test to the maximum flight temperature.

The resultant stability estimate $\frac{\Delta S_d}{S_d}$ is ±0.064.

The chamber pressure and temperature measurements are known to better than one percent; $\frac{\Delta P}{P} = 0.01$ and $\frac{\Delta T}{T} = 0.01$.

The statistical error associated with the data point is equal to the $\sqrt{N_d}$ where $N_d$ is the number of counts detected. At the maximum density the detected count rate, $I_d$, was 145 x 16 = 2320 pulses per second. Each data point was the average of 30 one-second intervals or 2320 x 30 = 69,600 pulses. The error, $\Delta I_d$, is thus $\sqrt{\frac{69,600}{30}} = 8.75$ pulses per second. The value of wall scatter plus background, $I_w + I_b$, was determined by measurement with the chamber nearly evacuated, giving $I_w + I_b$ = 28 x 16 = 448 pulses per second. The fractional error

$$\frac{\Delta I_d}{I_d - I_w - I_b} = \frac{8.75}{2320 - 448} = 0.0047.$$

The wall scatter and background, $I_w + I_b$, was also obtained from the average of 30 one-second data points or 448 x 30 = 13,440 pulses. The error in this measurement, $\Delta(I_w + I_b)$ is thus $\sqrt{\frac{13440}{30}} = 3.9$ pulses per second. The fractional error is

$$\frac{\Delta(_w + I_b)}{I_d - I_w - I_b} = \frac{3.9}{2320 - 448} = 0.0021$$

To obtain the total calibration error, these individual errors are summed on an RSS basis, giving the total calibration error $\frac{\Delta K}{K} = 0.075$ or ±7.5%

## Flight Environment

The flight data may be represented by the following equation:

$$N_d = I_d \tau = (S_s\ S_d\ K\ \rho + I_b)\ \tau \qquad (32)$$

where $N_d$ is the detected count in the time interval $\tau$ as a function of density, $\rho$, and background, $I_b$. $S_s$ and $S_d$ are stability factors associated with the shock layer and sensor drift. K is the calibration constant. Density is determined from

$$\rho = \left(\frac{N_d}{\tau} - I_b\right) \frac{1}{S_s\ S_d\ K} \qquad (33)$$

Taking the logarithm of equation 33 gives

$$\ln \rho = \ln \left(\frac{N_d}{\tau} - I_b\right) - \ln S_s - \ln S_d - \ln K \qquad (34)$$

The derivative of 34 is

$$\frac{d\rho}{\rho} = \frac{d\left(\frac{N_d}{\tau} - I_b\right)}{I_d - I_b} - \frac{dS_s}{S_s} - \frac{dS_d}{S_d} - \frac{dK}{K} \qquad (35)$$

$$\left(\frac{N_D}{\tau} - I_b\right) = \frac{dN_d}{\tau} - \frac{N_d\ d\tau}{\tau^2} - dI_b \qquad (35a)$$

Substituting small changes for the differential values gives

$$\frac{\Delta\rho}{\rho} = \frac{\Delta N_d}{\tau(I_d - I_b)} - \frac{I_d}{I_d - I_b}\frac{\Delta\tau}{\tau} - \frac{\Delta I_b}{I_d - I_b} - \frac{\Delta S_s}{S_s} - \frac{\Delta S_d}{S_d} - \frac{dK}{K} \qquad (36)$$

The effect of shock layer on sensor accuracy has been previously discussed. The graphical analysis shown in figure 22 resulted in an error, $\frac{\Delta S_s}{S_s}$, of 0.004.

The stability through the flight, $\frac{\Delta S_d}{S_d}$, is determined by comparison of ascent data with descent data showing a drift of ±0.01.

The source statistical fluctuation causes uncertainty in the pulse count. $N_d$. This uncertainty is equal to the square root of the number of pulses detected:

$$\Delta N_d = \frac{\sqrt{N_d \times 16}}{16}$$

At 20 km altitude, where $N_d$ = 1010 pulses, $I_d$ = 1010 pulses per second, and $I_b$ = 110 pulses per second

$$\frac{\Delta N_d}{\tau(I_d - I_b)} = \frac{\sqrt{1010 \times 16}}{16\ (1010-110)} = 0.0095$$

The background count rate $I_b$ was determined by averaging 24 one-second background measurements taking from 70 t0 90 km altitude. The error in this measurement, $\Delta I_b$, is equal to the square root of the total number of pulses detected.

$$\Delta I_b = \frac{\sqrt{110 \times 16 \times 24}}{16 \times 24} = 0.53 \text{ pulse per second}$$

At 20 km altitude the error caused by uncertainty of the background estimate is

$$\frac{\Delta I_b}{I_d - I_b} = \frac{.053}{1010-110} = 0.0006$$

The stability of the shield modulator timing was established by comparing the time cycles during the sphere calibration with the source modulator cycles during the ascent and descent portions of the flight. The maximum timing variation was ±.015 second. The difference in shield movement delay during ascent and descent was ±.005 second. The total error in timing is thus

$$\frac{\Delta\tau}{\tau} + 0.015$$

At 20 km this results in a density error of

$$\frac{I_d}{I_d - I_b} \frac{\Delta\tau}{\tau} = \frac{1010}{1010-110} 0.015 = 0.017$$

The teflin ablating coat on the nose cone is 0.3 cm thick. The two-way attenuation of 134 keV gammas by this coat is approximately 8%. The two sigma error introduced by total ablation of this layer is considered ±4%. The resulting one-sigma sensor drift is thus

$$\frac{\Delta S_d}{S_d} = 0.02$$

The data reduction counters resolve one output pulse. The error in any single count may be ±0.5 pulse. At high altitudes where there are few total pulses, this error becomes significant. At 20 km altitude this pulse resolution error is

$$\frac{\Delta N_d}{\tau(I_d - I_b)} = \frac{0.5}{1\ (1010-110)} = 0.0006$$

The velocity error is caused by assuming a linear density change over the altitude range traveled during one-second sampling period. The maximum vertical travel in one-second time was 1500 meters. The maximum deviation of density from linear over a 1500 meter range is 0.8%. The average density over a one-second interval is thus no more than 0.8% in error from the actual density at a time half way through the one-second interval.

## Total Error

These errors are all summed on an RSS basis in table I, giving a total one-sigma system error at 20 km altitude of ±8.2%.

The altitude dependent errors are summed and plotted versus altitude in figure 36. The 10 point curve fit improves accuracy as shown.

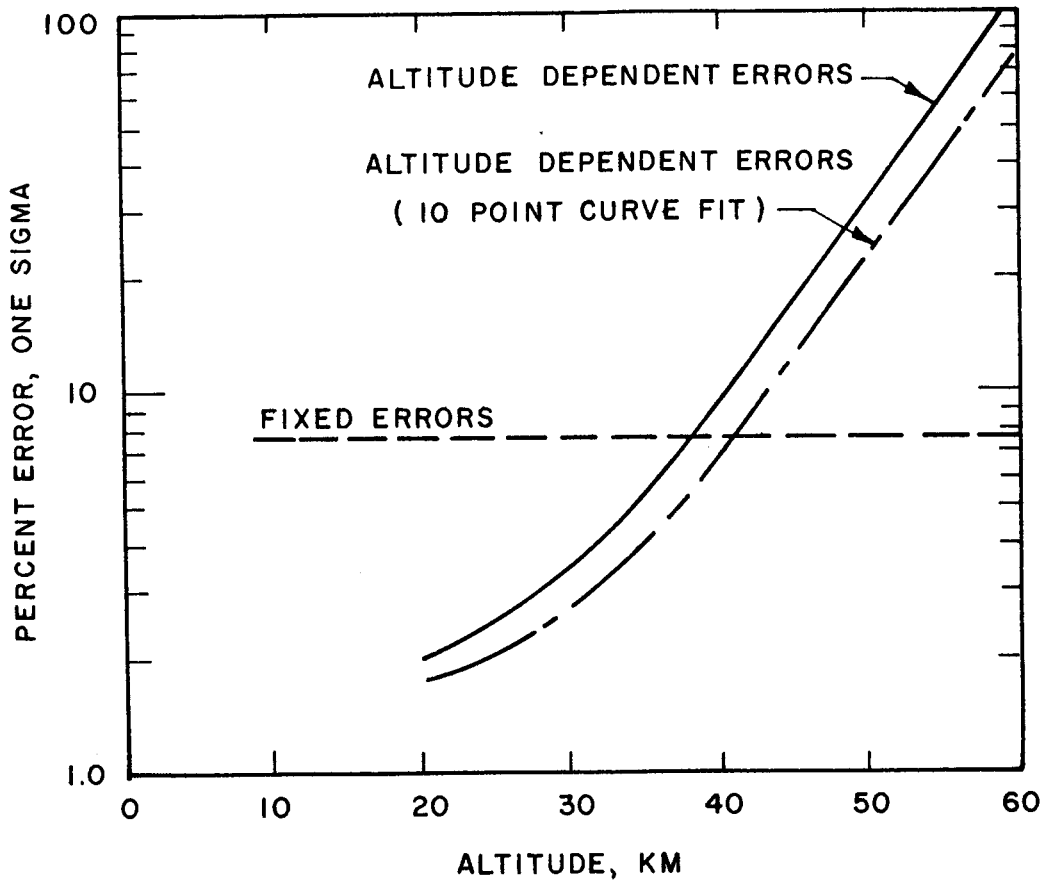


Figure 36 - Error Band Versus Altitude

## FURTHER DATA ANALYSIS RECOMMENDATIONS

The data analysis techniques used in the previous section were of a minimal nature amenable to hand analysis. The use of involved computer programs was beyond the scope of this effort. Some thought was given to possible analysis methods. The techniques considered were to fit the data points with analytical expressions solving for the unknown parameters of density and background. There is considerable freedom in selecting the best method. The number of data points can be small to provide good density resolution with altitutde but then the smoothing action of many points is diminished. The data points may be weighted as to their accuracy, but this may tend to merely extrapolate the curve from a few accurate data points and not use data in the actual region of interest. Where the background and signals are of the same relative magnitude, curve fitting proves very useful in separating the two. When the background is high compared to the signal, accurate background information is obtained, but density data is of poor accuracy. At low altitudes, where air scatter count rates are high compared to the background, accurate density data is obtained but the background data extracted is of poor accuracy. The usefulness of curve fitting has been demonstrated by improving the accuracy of the density measurement using the 10 point curve fit method described earlier.

# CONCLUSIONS, RECOMMENDATIONS, AND APPLICATIONS

This program and the previous program, NAS1-2306, have proven the feasibility of measuring free air density at high altitudes from vehicles traveling at high velocity using gamma backscatter principles. The objective of this program, to extend the altitude range to 91.5 kilometers, was not achieved due to high levels of background. It is concluded that the high background level is not of cosmic origin but a direct result of the source characteristics, i.e., multiple scattering of high energy radiation from the source, both gamma-rays and X-rays produced from the bremsstrahlung interactions of the emitted betas, through the vehicle skin to the detector. The increased source strength increased this background proportionately over the previous tests. Postponements of the flight test date caused a significant decay of the strength of the flight source which somewhat reduced the altitude capability.

Very good measurement correlation was obtained between the gamma-ray backscatter measurement, arcasonde measurement, and radiosonde measurements of air density in the region of overlap. Although preflight tests indicated an accuracy capability of ±7.5%, much better correlation with these other measurements was found. Good correlation was also found between the calibration data and the estimated calibration constant obtained with the mathematical model. This analytical work improves confidence in the ability to design measurement systems having the desired characteristics.

The measurement system ruggedness was demonstrated by having performed properly in the flight acceptance tests and the flight environment of the Nike-Apache boost system. This speaks particularly well of normally fragile elements such as the sodium iodide crystal and the photomultiplier tube.

With the better understanding of the cause of the limiting background, it is recommended that an additional flight be performed using an isotope source that does not contain the high energy flux. Such sources are Gd-153 and Se-75. Use of such a source and the source modulating system will establish the cosmic and solar contribution to the background and establish the altitude capability of the flight configuration as a function of source strength and measurement geometry.

Application of this measurement technique can then be extended to critical requirements such as determining the density profile of planetary atmosphere. Of particular interest is the atmosphere of Mars. The X-ray or gamma backscatter approach is reliable, proven, unaffected by unknown aerodynamic environments, unaffected by high velocities, and provides a minimum of vehicle constraints.

GIANNINI CONTROLS CORPORATION
Duarte, California
13 September 1966

# APPENDIX A

# INVESTIGATION OF THE EFFECTS OF THE HIGH ENERGY GAMMA AND BETA COMPONENT ON SENSOR PERFORMANCE

## Purpose

The purpose of this investigation is to determine the effects of the Cerium-144 high energy gamma and beta component on the sensor source modulator open/closed ratio and background level. Flight data has shown a lower than expected shield open/closed ratio and a higher than expected background level. It is suspected that the backscattered high energy gammas contribute significantly to the total air scatter flux and are not sufficiently attenuated by the source modulating shield. It is also suspected that multiple scattering in the vehicle skin of the high energy gamma component contributes significantly to the background level.

## Scope

Theoretical estimates of the importance of the high energy gamma and beta flux relative to the 134 keV gamma flux on source modulator effectiveness are made. Experimental measurements of the source output and modulator effectiveness are provided as backup to the theoretical estimates. Theoretical estimates of the source contributed background flux are calculated. Experimental verification of the beta bremsstrahlung effects are shown. No practical method of experimentally measuring the source contributed background flux using laboratory facilities has yet been devised.

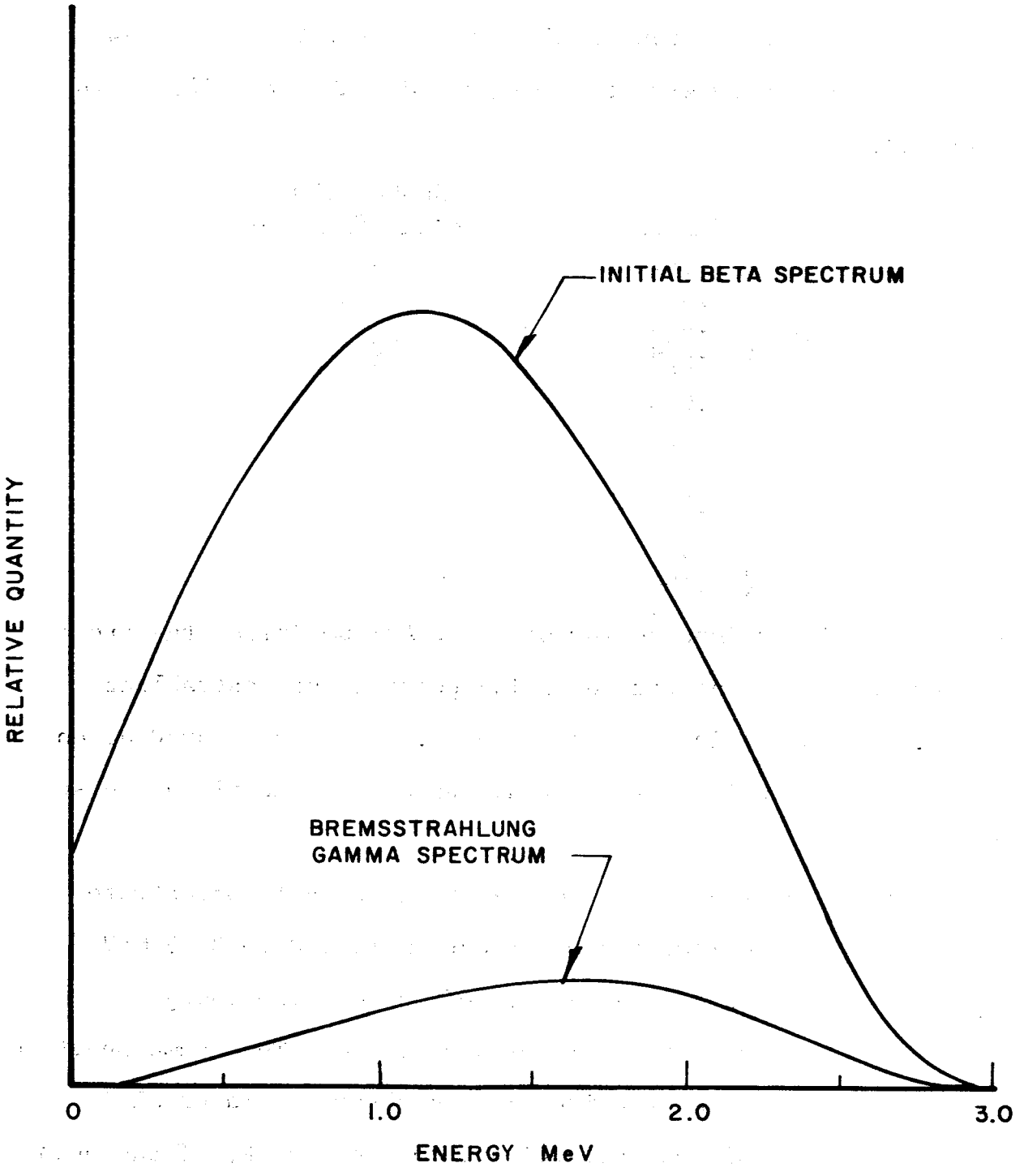


Figure 37 - Beta Bremsstrahlung Spectrum

## Source Spectrum

The theoretical output radiation from the Ce-144/Pr-144 source is given below with the energy and number per 100 disintegrations.

| | Energy (MeV) | Number/100 Disintegrations |
|---|---|---|
| gammas | 2.185 | 3 |
| | 1.480 | 1.2 |
| | .695 | 3 |
| | .134 | 30 |
| | .080 | 10 |
| | .036 | 30 |
| betas | 3.150 | 95 |
| | 2.450 | 3 |
| | .900 | 2 |
| | .320 | 60 |
| | .245 | 5 |
| | .184 | 30 |

The beta particles interacting with the Cerium Oxide, the steel capsules, and the tungsten shielding generate bremsstrahlung photons. The significant beta is the 3.15 MeV, 95% abundant one. The others are low in energy and abundance by comparison and so will be neglected.

The beta spectrum from the Ce-144 is not all concentrated at 3.15 MeV, but follows a broad spectrum from 0 to 3.15 MeV, with an average energy of about 0.4 of the maximum energy.

Figure 37 illustrates this beta spectrum. The gamma spectrum resulting from beta interaction with an absorbing material is a function of the Z of the material and the energy, E, of the beta particle. The ratio of radiation loss to ionization loss is given by

$$\frac{E\ Z}{800}$$

For tungsten with a Z of 74, the resultant energy spectrum of the radiation loss is shown in figure 37. The bremsstrahlung spectrum will be shifted to lower energies but for conservatism in this analysis it is assumed that this curve is the resultant bremsstrahlung spectrum. The number of bremsstrahlung photons generated per 100 disintegrations is the ratio of the area under the bremsstrahlung spectrum to the beta spectrum times the 3.15 MeV beta abundance. This computation gives a bremsstrahlung photon abundance of 11.2 photons/100 disintegrations.

Source Spectrum after Capsule and Skin Attenuation

The attenuation provided by the steel capsule and skin is computed from the following equation:

$$K_a = e^{-\mu_c \rho_c x_c - \mu_s \rho_s x_x} \tag{37}$$

where $\mu_c$, $\rho_c$, and $x_c$ are the mass absorption coefficient, density, and thickness of the steel capsule; and $\mu_s$, $\rho_s$, and $x_s$ are the mass absorption coefficient, density, and thickness of the fiberglass skin. The following table II shows the attenuation of the various gamma components. The attenuation of the bremsstrahlung component is computed versus energy, and plotted in figure 38. The value of $K_a$ is the ratio of the areas under curves 1 and 2.

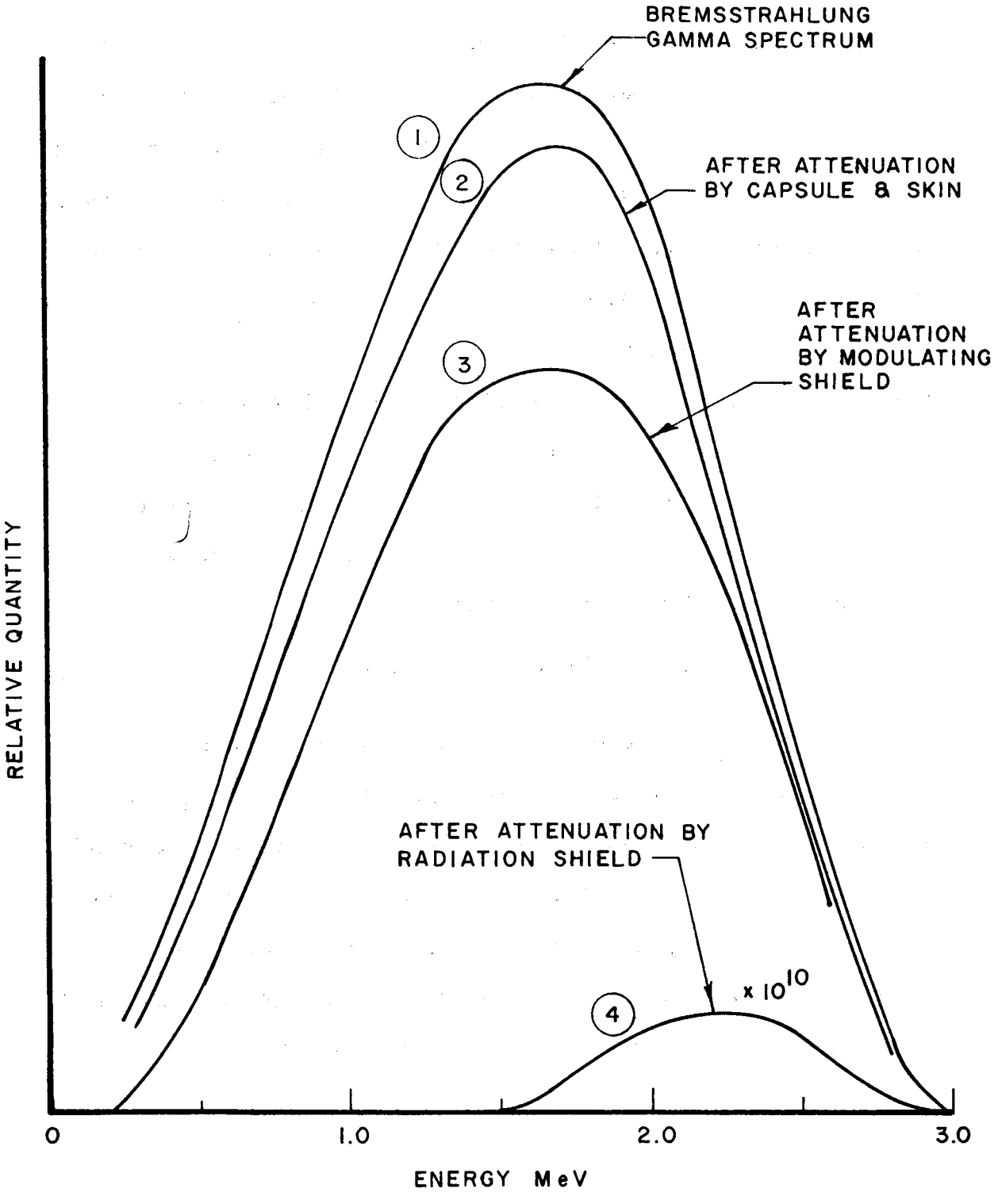


Figure 38 - Attenuation of Bremsstrahlung Radiation

TABLE II

ATTENUATION BY CAPSULE AND SKIN

| Energy MeV | Number per 100 Disintegrations before Attenuation | Attenuation Factor, $K_a$ | Number per 100 Disintegrations after Attenuation |
|---|---|---|---|
| .134 | 30 | .69 | 20.7 |
| .695 | 3 | .86 | 2.6 |
| 1.48 | 1.2 | .90 | 1.1 |
| 2.18 | 3 | .92 | 2.8 |
| bremsstrahlung | 11.2 | .90 | 10.1 |

Attenuation by Modulating Shield

The attenuation by the modulating shield is computed from the equation

$$K_a = e^{-\mu_m \rho_m x_m} \tag{38}$$

where $\mu_m$, $\rho_m$, and $x_m$ are the mass absorption coefficient, density, and thickness of the tungsten modulating shield, respectively. Table III shows the attenuation of the various gamma components. The bremsstrahlung attenuation factor is determined by the ratio of the areas under curves 2 and 3 of figure 38.

TABLE III

ATTENUATION BY MODULATING SHIELD

| Energy MeV | Number per 100 Disintegrations before Attenuation | Attenuation Factor, $K_a$ | Number per 100 Disintegrations after Attenuation |
|---|---|---|---|
| .134 | 20.7 | $2 \times 10^{-5}$ | .0004 |
| .695 | 2.6 | .614 | 1.6 |
| 1.48 | 1.1 | .763 | 0.8 |
| 2.18 | 2.8 | .793 | 2.2 |
| bremsstrahlung | 10.1 | .73 | 7.4 |
| TOTALS | 37.3 | | 12.0 |

Ratio of Shield Open to Shield Closed

Referring to table III, it is evident that per 100 disintegrations there are 37.3 photons available for scattering with the shield open and 12.0 available with the shield closed, giving an open/closed ratio of 3.1 to 1.

Experimental measurements of the spectrum from the test source mounted in the nose cone were taken with the shield open and closed to verify this ratio. The results are illustrated in figure 39, showing the spectrum measured perpendicular to the vehicle axis and at an angle of 45 degrees from the vehicle axis. The ratio of areas under the spectra above 100 keV was measured and compared, giving actual ratios of 6 to 1 at 90 degrees and 3 to 1 at 45 degrees.

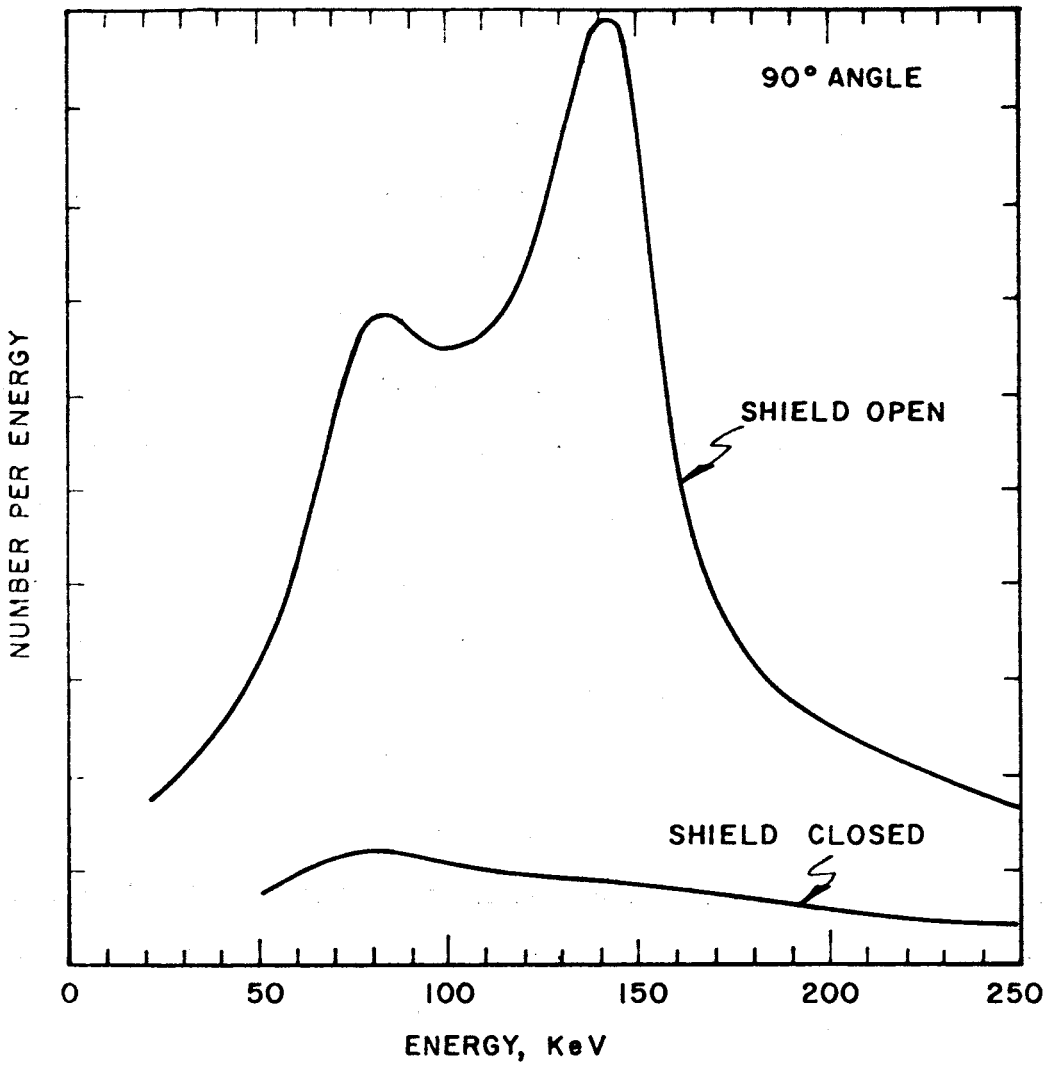


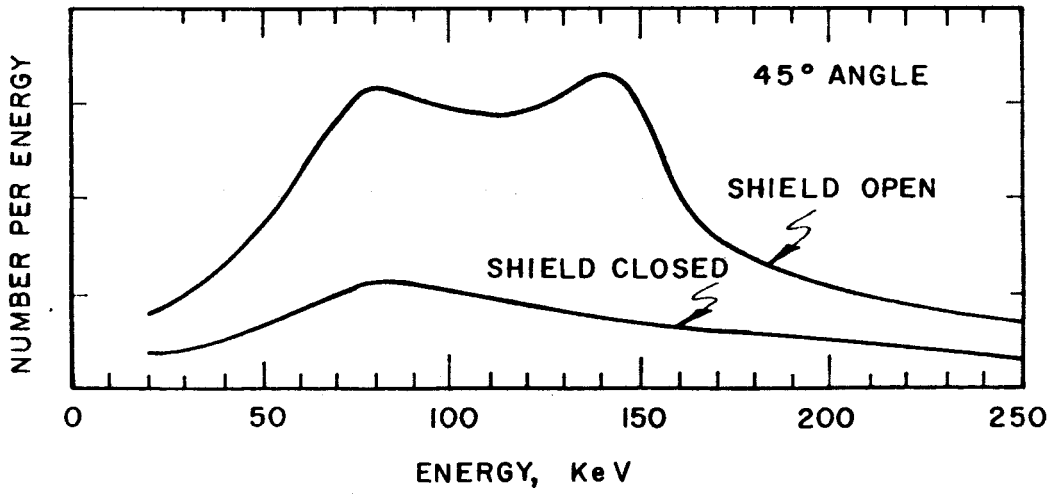


Figure 39 - Measured Spectrum of Test Source in Nose Cone

The theoretical prediction of a 3:1 ratio at a 90° angle compares with the 6:1 ratio obtained experimentally. The factor of two difference is probably due to the fact that the bremsstrahlung radiation spectrum is actually lower in energy than assumed in the theoretical analysis and is thus more effectively attenuated by the shield. Also, the bremsstrahlung is not all generated by interaction with tungsten but some by interaction with Cerium Oxide and steel, lower Z materials. This reduces the relative amount of high energy gammas, making the modulating shield more effective.

The angular effect is seen to be very pronounced, comparing the 90° test data and the 45° test data. At 45° all the attenuation paths are 1.4 times longer, reducing the low energy component available for scatter. This consequently reduces the shield open/closed ratio to 3 to 1. This experimental data agrees well with the 3 to 1 ratio obtained in the flight.

## Background Estimate

The direct transmission from the source to the detector through the 23.1 cm tungsten shield is estimated by considering the 2.18 MeV gammas and the bremsstrahlung gammas. All lower energies are negligible by comparision after attenuation. The attenuation of the 2.18 MeV gammas is given as

$$K_1 = De^{-\mu\rho x} = De^{-.043x17.7x23.1} = De^{-17.6} \qquad (39)$$

The dose buildup factor, D, is 7.0 for a $\mu\rho x$ of 17.6, giving

$$K_1 = 7.0\ e^{-17.6} = 1.54x10^{-7}$$

The absorption of the bremsstrahlung component is determined by the ratio of areas under curves 1 and 4 of figure 38, giving $K_2 = 1.17 \times 10^{-9}$. The total direct transmission, $I_t$, from a 50 curie source is found from the following

$$I_t = \frac{I_o A_d}{4\pi r^2} (a_1 K_1 + a_2 K_2) \qquad (40)$$

where:

$I_o$ = Source strength = 50 curies x $3.7 \times 10^{10}$ disintegrations/sec/curie

$A_d$ = Detector area = 57 $cm^2$

$r$ = Distance from source to detector = 43 cm

$a_1$ = Abundance of 2.18 MeV gammas = .03 per disintegration

$a_2$ = Abundance of bremsstrahlung gammas = .112 per disintegration

$$I_t = \frac{50 \times 3.7 \times 10^{10} \times 57 \ (.03 \times 1.54 \times 10^{-7} + .112 \times 17 \times 10^{-9})}{4\pi 43^2} = .21 \text{ pps}$$

The bremsstrahlung component is small compared to the 2.18 MeV gamma.

The background due to multiple skin scatter from the source to detector is estimated with the following assumptions:

1. Gammas available given in Table II.
2. Ten percent of these available gammas reach the skin with the modulating shield open.
3. Scatter takes place in skin.
4. Transmission takes place down the skin with absorption.

5. Second scatter takes place in the vicinity of the detector.

6. Twenty-five percent of these secondary scattered gammas reach the detector and are counted.

The following table IV shows the calculation of multiple skin scatter. $\sigma_s$, $x_1$, and $\rho_s$ are the scattering cross section, thickness, and density of the skin near the source. $\mu_a$, $\rho_s$, and r are the absorption cross section, density, and distance for absorption in the skin from the region of the source to the region of the detector. $\sigma_s$, $\rho_s$, and $x_2$ are the scattering cross section, density, and length of the skin in the vicinity of the detector available for a second scattering event. These quantities are combined as follows:

$$I_{ss} = I_o\, G_1\, G_2\, G_3\, \sigma_s\, \rho_s\, x_1\, e^{-\mu \rho_s r}\, \sigma_s\, \rho_s x_2 \qquad (41)$$

where

$I_{ss}$ = skin scattered radiation to the detector

$I_o$ = source strength = 50 curies x 3.7 x $10^{10}$ disintegrations/sec

$G_1$ = fraction of gammas reaching skin = 0.10

$G_2$ = inverse square loss from first scatter to second scatter

$$G_2 = \frac{\text{Skin cross sectional area}}{4\pi\ (\text{distance from first to second scatter})}$$

$$= \frac{.62\ \pi\ 14.5}{4\pi(43)^2} = 1.23 \times 10^{-3}$$

$G_3$ = fraction of second scattered gammas reaching detector = 0.25

Let

$$K = I_o\ G_1\ G_2\ G_3$$

$$K = 3.7 \times 10^{10} \times 50 \times .1 \times 1.23 \times 10^{-3} \times .25$$

$$= 5.7 \times 10^{7}$$

TABLE IV

CALCULATION OF MULTIPLE SKIN SCATTER

| | # per Disinteg. | $\sigma_s$ $cm^2/gm$ | $\sigma_s \rho_s x_1$ | $\mu_a$ $cm^2/gm$ | $\mu_a \rho_s r$ | $e^{-\mu_a \rho_s r}$ | $\sigma_s \rho_s x_2$ | $I_{ss}$ pps |
|---|---|---|---|---|---|---|---|---|
| Brems.gammas | .111 | .025* | .027 | .05 | 3.8 | .022 | .22 | 825 |
| 2.18 MeV " | .030 | .018 | .02 | .04 | 3.0 | .05 | .16 | 275 |
| 1.48 MeV " | .012 | .025 | .027 | .05 | 3.8 | .022 | .22 | 89 |
| .695 MeV " | .030 | .05 | .055 | .07 | 5.2 | .0054 | .53 | 220 |
| .134 MeV | .300 | .12 | .132 | .15 | 11.0 | $1.7 \times 10^{-5}$ | 1.04 | 40 |
| | | | | | | | TOTAL - | 1449 pps |

* Assuming 1.5 Mev

The resultant count rate is 1449 pps. Dividing by 16 gives 91 pps, which is the same order of magnitude as the background measured during the flight at apogee (110 pps). Notice that the major contributor is from the beta bremsstrahlung.

When the modulator shield is open there is less tungsten interrupting the beta particles and thus less resultant bremsstrahlung.

### Experimental Verification of Bremsstrahlung Component

The presence of the beta bremsstrahlung component of gamma radiation was verified by measuring the radiation spectrum from the test source with various lead absorber thicknesses placed between it and the detector. The actual attenuation was compared with the theoretical attenuation at several energies. A typical curve is shown in figure 40. This data was compiled at several energies and the percent bremsstrahlung generation determined as a function of absorber thickness. This data is shown in figure 41. The equivalent tungsten thickness is shown for reference. This data verifies a significant generation of bremsstrahlung radiation.

## Conclusions

It is concluded that the effectiveness of the source modulator is hampered by the significant amount of high energy gammas and bremsstrahlung gammas from the Cerium-144 source, thus lowering the source modulator open/closed ratio.

It is concluded that the large background at apogee is due to multiple skin scatter of the high energy gamma flux from the

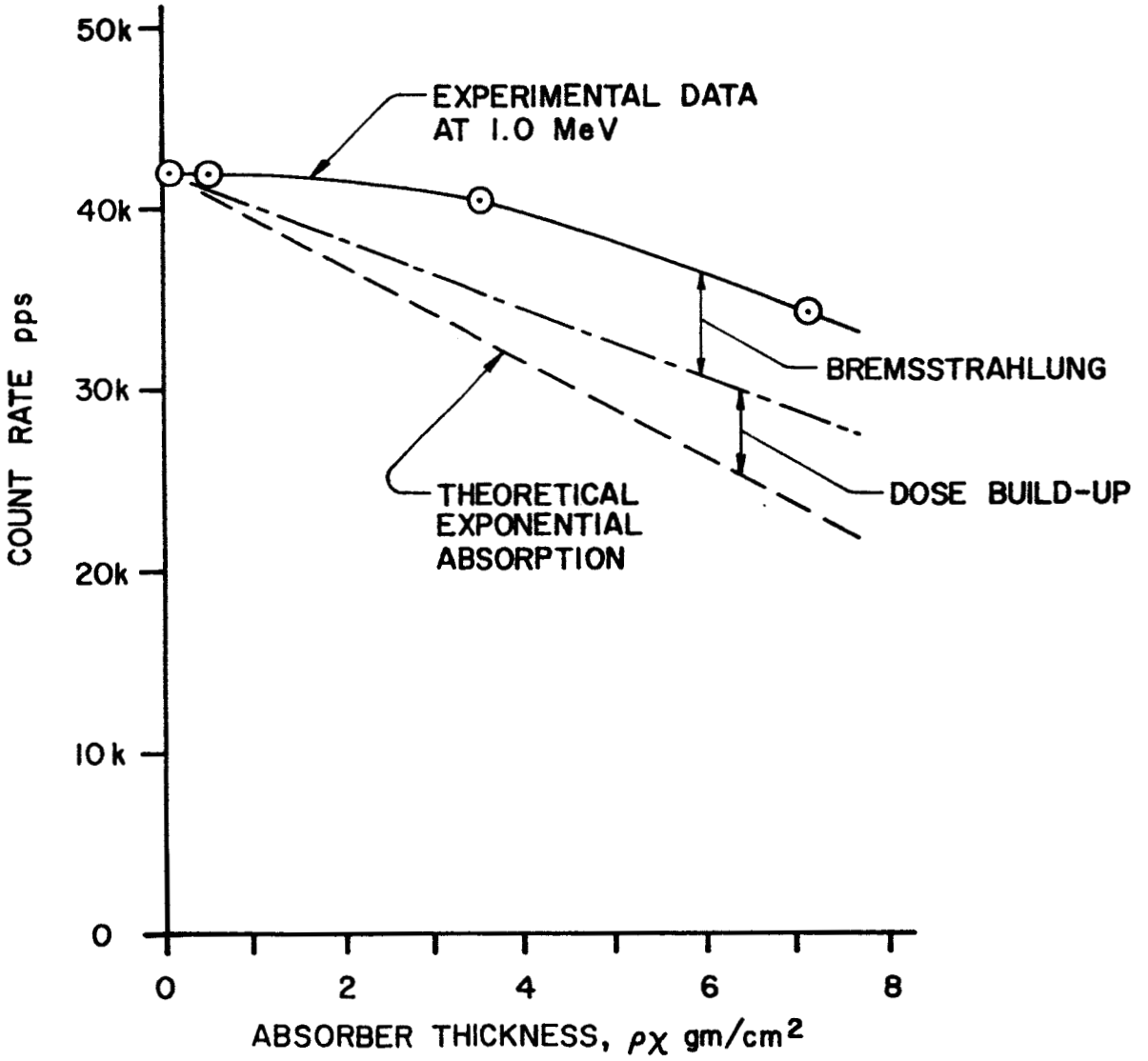


Figure 40 - Typical Absorber Characteristics
Illustrating Bremsstrahlung Radiation

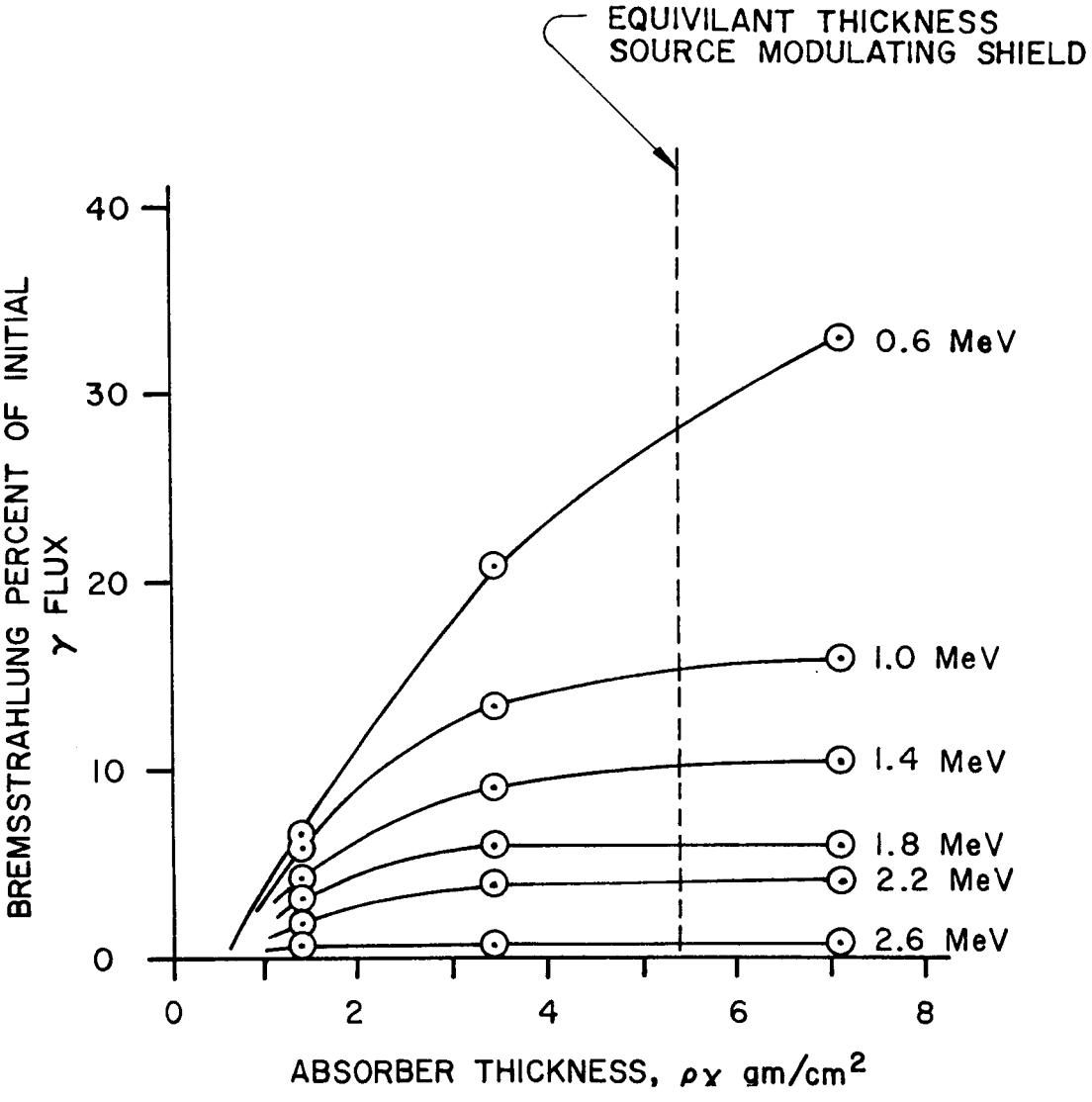


Figure 41 - Percent Bremsstrahlung Generation Versus Absorber Thickness at Several Energies

source to the detector. The presence of high energy bremsstrahlung gammas has been verified experimentally.

APPENDIX B

FLIGHT TEST DATA, TEST DATE 20 JANUARY 1966

| | Time (hr:min:sec) | Output Pulse Rates (Pulses per Second) | | | | | | | Altitude (km) |
|---|---|---|---|---|---|---|---|---|---|
| | | E | A | I E-A | C | 12 | II C-12 | I+II | |
| + | 14:01:27.6 | 1172 | 352 | 820 | 658 | 255 | 403 | 1223 | 18.96 |
| | 28.6 | 450 | 202 | 248 | 311 | 154 | 157 | 405 | 20.42 |
| + | 29.6 | 774 | 266 | 508 | 469 | 194 | 275 | 783 | 21.9 |
| | 30.6 | 339 | 158 | 181 | 251 | 120 | 131 | 312 | 23.4 |
| + | 31.6 | 522 | 197 | 325 | 328 | 137 | 191 | 516 | 24.8 |
| | 32.6 | 288 | 141 | 147 | 196 | 102 | 94 | 241 | 26.2 |
| + | 33.6 | 376 | 155 | 221 | 254 | 114 | 140 | 361 | 27.6 |
| | 34.7 | 242 | 121 | 121 | 169 | 93 | 76 | 197 | 29.2 |
| + | 35.7 | 291 | 124 | 167 | 202 | 89 | 113 | 280 | 30.6 |
| | 36.7 | 228 | 114 | 114 | 152 | 82 | 70 | 184 | 32.0 |
| + | 37.7 | 234 | 109 | 125 | 163 | 82 | 81 | 206 | 33.4 |
| | 38.7 | 200 | 104 | 96 | 133 | 71 | 62 | 158 | 34.7 |
| + | 39.7 | 211 | 96 | 115 | 138 | 68 | 70 | 185 | 36.1 |
| | 40.7 | 193 | 100 | 93 | 130 | 74 | 56 | 149 | 37.4 |
| + | 41.7 | 195 | 95 | 100 | 131 | 70 | 61 | 161 | 38.7 |
| | 42.7 | 186 | 97 | 89 | 121 | 68 | 53 | 142 | 40.0 |
| + | 43.7 | 178 | 86 | 92 | 117 | 65 | 52 | 144 | 41.3 |
| | 44.8 | 188 | 100 | 88 | 121 | 70 | 51 | 139 | 42.7 |
| + | 45.8 | 171 | 89 | 82 | 115 | 64 | 51 | 133 | 44.1 |
| | 46.8 | 169 | 88 | 81 | 118 | 68 | 50 | 131 | 45.3 |
| + | 47.8 | 159 | 82 | 77 | 109 | 59 | 50 | 127 | 46.5 |
| | 48.8 | 178 | 94 | 84 | 113 | 63 | 50 | 134 | 47.8 |
| + | 49.8 | 169 | 90 | 79 | 102 | 58 | 44 | 123 | 49.1 |
| | 50.8 | 178 | 97 | 81 | 116 | 67 | 49 | 130 | 50.3 |
| + | 51.8 | 154 | 80 | 74 | 104 | 60 | 44 | 118 | 51.5 |
| | 52.9 | 184 | 96 | 88 | 111 | 65 | 46 | 134 | 52.8 |
| + | 53.9 | 156 | 84 | 72 | 108 | 59 | 49 | 121 | 54.1 |
| | 54.9 | 168 | 89 | 79 | 118 | 67 | 51 | 130 | 55.3 |
| + | 55.9 | 145 | 77 | 68 | 104 | 58 | 46 | 114 | 56.5 |
| | 56.9 | 173 | 94 | 79 | 118 | 69 | 49 | 128 | 57.6 |
| + | 57.9 | 148 | 77 | 71 | 98 | 57 | 41 | 112 | 58.8 |
| | 58.9 | 175 | 99 | 76 | 114 | 68 | 46 | 122 | 59.9 |
| + | 59.9 | 147 | 75 | 72 | 96 | 56 | 40 | 112 | 61.2 |
| | 14:02:00.9 | 171 | 94 | 77 | 114 | 64 | 50 | 127 | 62.2 |
| + | 01.9 | 150 | 76 | 74 | 95 | 54 | 41 | 115 | 63.4 |
| | 03.0 | 179 | 92 | 87 | 112 | 63 | 49 | 136 | 64.6 |
| + | 04.0 | 153 | 79 | 74 | 95 | 55 | 40 | 114 | 65.7 |
| | 05.0 | 176 | 92 | 84 | 112 | 64 | 48 | 132 | 66.8 |
| + | 06.0 | 146 | 75 | 71 | 104 | 59 | 45 | 116 | 67.9 |
| | 07.0 | 172 | 94 | 78 | 112 | 67 | 45 | 123 | 69.1 |
| + | 08.0 | 150 | 81 | 69 | 95 | 53 | 42 | 111 | 70.0 |
| | 09.0 | 170 | 92 | 78 | 119 | 70 | 49 | 127 | 71.1 |
| + | 10.0 | 142 | 75 | 67 | 98 | 57 | 41 | 108 | 72.2 |
| | 11.0 | 173 | 91 | 82 | 116 | 67 | 49 | 131 | 73.2 |
| + | 12.0 | 147 | 80 | 67 | 94 | 56 | 38 | 105 | 74.1 |
| | 13.1 | 172 | 91 | 81 | 117 | 67 | 50 | 131 | 75.2 |
| + | 14.1 | 143 | 78 | 65 | 100 | 58 | 42 | 107 | 76.3 |
| | 15.1 | 180 | 96 | 84 | 117 | 70 | 47 | 131 | 77.3 |
| + | 16.1 | 150 | 78 | 72 | 97 | 55 | 42 | 114 | 78.3 |
| | 17.1 | 167 | 91 | 76 | 112 | 65 | 47 | 123 | 79.3 |

(+ denotes shield open)

FLIGHT TEST DATA, TEST DATE 20 JANUARY 1966

| | Time (hr:min:sec) | Output Pulse Rates (Pulses per Second | | | | | | | Altitude (km) |
|---|---|---|---|---|---|---|---|---|---|
| | | E | A | I E-A | C | 12 | II C-12 | I+II | |
| + | 14:02:18.1 | 151 | 80 | 71 | 101 | 59 | 42 | 113 | 80.2 |
| | 19.1 | 170 | 95 | 75 | 116 | 66 | 50 | 125 | 81.2 |
| + | 20.1 | 149 | 77 | 72 | 94 | 56 | 38 | 110 | 82.1 |
| | 21.2 | 166 | 90 | 76 | 112 | 64 | 48 | 124 | 83.1 |
| + | 22.2 | 143 | 79 | 64 | 103 | 58 | 45 | 109 | 84.0 |
| | 23.2 | 182 | 94 | 88 | 118 | 68 | 50 | 138 | 85.0 |
| + | 24.2 | 139 | 74 | 65 | 97 | 54 | 43 | 108 | 85.9 |
| | 25.2 | 173 | 93 | 80 | 118 | 68 | 50 | 130 | 86.8 |
| + | 26.2 | 156 | 78 | 78 | 99 | 55 | 44 | 122 | 87.6 |
| | 27.2 | 177 | 94 | 83 | 118 | 65 | 53 | 136 | 88.5 |
| + | 28.2 | 143 | 74 | 69 | 101 | 59 | 42 | 111 | 89.4 |
| | 29.3 | 178 | 100 | 78 | 117 | 68 | 49 | 127 | 90.6 |
| + | 30.3 | 149 | 80 | 69 | 101 | 58 | 43 | 112 | 91.6 |

(+ denotes shield open)

FLIGHT TEST DATA, TEST DATE 20 JANUARY 1966

| | Time (hr:min:sec) | Output Pulse Rates (Pulses per Second) | | | | | | | Altitude (km) |
|---|---|---|---|---|---|---|---|---|---|
| | | E | A | I E-A | C | 12 | II C-12 | I+II | |
| | 14:05:31.1 | 169 | 91 | 78 | 115 | 67 | 48 | 126 | 93.0 |
| + | 32.1 | 145 | 79 | 66 | 99 | 60 | 39 | 105 | 92.1 |
| | 33.1 | 177 | 95 | 82 | 111 | 65 | 46 | 128 | 91.2 |
| + | 34.2 | 143 | 78 | 65 | 100 | 57 | 43 | 103 | 90.4 |
| | 35.2 | 173 | 91 | 82 | 116 | 66 | 50 | 132 | 89.5 |
| + | 36.2 | 143 | 78 | 65 | 104 | 59 | 45 | 110 | 88.5 |
| | 37.3 | 176 | 96 | 80 | 117 | 67 | 50 | 130 | 87.3 |
| + | 38.3 | 154 | 88 | 66 | 107 | 60 | 47 | 113 | 86.4 |
| | 39.3 | 172 | 96 | 76 | 120 | 69 | 51 | 127 | 85.4 |
| + | 40.3 | 143 | 80 | 63 | 100 | 60 | 40 | 103 | 84.5 |
| | 41.4 | 160 | 87 | 73 | 109 | 65 | 44 | 117 | 83.5 |
| + | 42.4 | 145 | 77 | 68 | 96 | 59 | 37 | 105 | 82.6 |
| | 43.4 | 181 | 109 | 72 | 124 | 70 | 54 | 126 | 81.7 |
| + | 44.4 | 144 | 79 | 65 | 97 | 60 | 37 | 102 | 80.8 |
| | 45.4 | 170 | 92 | 78 | 111 | 68 | 43 | 121 | 79.8 |
| + | 46.4 | 140 | 76 | 64 | 99 | 60 | 39 | 103 | 78.8 |
| | 47.5 | 173 | 96 | 77 | 115 | 67 | 48 | 125 | 77.7 |
| + | 48.5 | 138 | 75 | 63 | 102 | 59 | 43 | 106 | 76.8 |
| | 49.5 | 179 | 101 | 78 | 117 | 68 | 49 | 127 | 75.9 |
| + | 50.5 | 146 | 79 | 67 | 100 | 58 | 42 | 109 | 74.7 |
| | 51.6 | 173 | 99 | 74 | 123 | 71 | 52 | 126 | 73.7 |
| + | 52.6 | 147 | 83 | 64 | 98 | 56 | 42 | 106 | 72.7 |
| | 53.6 | 173 | 92 | 81 | 114 | 69 | 45 | 126 | 71.8 |
| + | 54.6 | 151 | 81 | 70 | 102 | 62 | 40 | 110 | 70.6 |
| | 55.7 | 176 | 93 | 83 | 111 | 67 | 44 | 127 | 69.6 |
| + | 56.7 | 146 | 78 | 68 | 109 | 64 | 45 | 113 | 68.5 |
| | 57.7 | 169 | 91 | 78 | 122 | 72 | 50 | 128 | 67.5 |
| + | 58.7 | 188 | 87 | 101 | 106 | 60 | 46 | 147 | 66.3 |
| | 59.7 | 177 | 95 | 82 | 113 | 68 | 45 | 127 | 65.2 |
| + | 14:06:00.7 | 158 | 83 | 75 | 107 | 63 | 44 | 119 | 64.2 |
| | 01.8 | 173 | 95 | 78 | 124 | 73 | 51 | 129 | 62.5 |
| + | 02.8 | 148 | 79 | 69 | 97 | 58 | 39 | 108 | 61.3 |
| | 03.8 | 164 | 98 | 66 | 113 | 66 | 57 | 123 | 60.2 |
| + | 04.8 | 147 | 83 | 64 | 103 | 60 | 43 | 107 | 59.1 |
| | 05.9 | 176 | 95 | 81 | 117 | 71 | 46 | 127 | 57.9 |
| + | 06.9 | 159 | 86 | 73 | 100 | 59 | 41 | 114 | 56.7 |
| | 07.9 | 181 | 93 | 88 | 121 | 84 | 37 | 125 | 55.6 |
| + | 08.9 | 151 | 80 | 71 | 106 | 62 | 44 | 115 | 54.3 |
| | 10.0 | 169 | 90 | 79 | 118 | 68 | 50 | 129 | 53.2 |
| + | 11.0 | 164 | 86 | 78 | 108 | 63 | 45 | 123 | 52.0 |
| | 12.0 | 173 | 95 | 78 | 120 | 72 | 48 | 126 | 50.8 |
| + | 13.0 | 157 | 87 | 70 | 110 | 62 | 48 | 118 | 49.6 |
| | 14.1 | 173 | 93 | 80 | 127 | 72 | 55 | 135 | 48.3 |
| + | 15.1 | 165 | 90 | 75 | 109 | 64 | 45 | 120 | 47.1 |
| | 16.1 | 176 | 95 | 81 | 120 | 71 | 49 | 130 | 45.9 |
| + | 17.1 | 168 | 89 | 79 | 113 | 62 | 51 | 130 | 44.6 |
| | 18.1 | 178 | 98 | 80 | 121 | 68 | 53 | 133 | 43.3 |
| + | 19.1 | 177 | 90 | 87 | 117 | 65 | 52 | 139 | 42.1 |
| | 20.2 | 187 | 100 | 87 | 124 | 74 | 50 | 137 | 40.8 |

(+ denotes shield open)

APPENDIX B - Continued

FLIGHT TEST DATA, TEST DATE 20 JANUARY 1966

| | Time (hr:min:sec) | Output Pulse Rates (Pulses per Second) | | | | | | | Altitude (km) |
|---|---|---|---|---|---|---|---|---|---|
| | | E | A | I E-A | C | 12 | II C-12 | I+II | |
| + | 14:06:21.2 | 189 | 91 | 98 | 126 | 69 | 57 | 155 | 39.5 |
| | 22.2 | 192 | 107 | 85 | 132 | 77 | 55 | 140 | 38.2 |
| + | 23.2 | 213 | 101 | 112 | 148 | 78 | 70 | 182 | 37.0 |
| | 24.3 | 195 | 101 | 94 | 132 | 74 | 58 | 152 | 35.0 |
| + | 25.3 | 237 | 114 | 123 | 156 | 79 | 77 | 200 | 33.6 |
| | 26.3 | 219 | 115 | 104 | 148 | 92 | 56 | 160 | 32.4 |
| + | 27.3 | 276 | 122 | 154 | 187 | 93 | 94 | 248 | 31.1 |
| | 28.4 | 234 | 120 | 114 | 164 | 94 | 70 | 184 | 29.6 |
| + | 29.4 | 359 | 156 | 203 | 248 | 119 | 129 | 332 | 28.35 |
| | 30.4 | 282 | 135 | 147 | 194 | 114 | 80 | 227 | 27.0 |
| + | 31.4 | 492 | 192 | 300 | 310 | 144 | 166 | 466 | 25.65 |
| | 32.5 | 332 | 165 | 167 | 234 | 125 | 109 | 276 | 24.3 |
| + | 33.5 | 680 | 252 | 428 | 429 | 182 | 247 | 675 | 22.95 |
| | 34.5 | 420 | 199 | 221 | 302 | 155 | 147 | 368 | 21.6 |
| + | 35.5 | 948 | 429 | 519 | 590 | 240 | 350 | 869 | 20.25 |
| | 36.5 | 1547 | 263 | 1284 | 384 | 194 | 190 | 1474 | 18.9 |
| + | 37.5 | 1287 | 427 | 860 | 750 | 374 | 376 | 1236 | 17.5 |

(+ denotes shield open)

## REFERENCES


1. Hakewessell, D. B.: Investigation of the Use of Radio-isotopes for Extremely High Altitude Measurement. ASD-TDR-62-880, Giannini Controls Corporation, November 1962.
2. Johnson, D. L.: X-ray Air Density Determination (X-RADD). FDL-TDR-64-29, Giannini Controls Corporation, May 1964.
3. Report of the International Commission on Radiological Units and Measurements (ICRU). Handbook 78, United States Department of Commerce, National Bureau of Standards, 1959.
4. Solar Geophysical Data. CRPL-FB-28, Space Disturbances Laboratory, February 1966.
5. Northrop, J. A.: Gamma-Ray Measurements In and Above the Atmosphere. LA-2507, Los Alamos Scientific Laboratory, University of California, June 1961.
6. Peterson, L. E.: The 0.5 MeV Gamma-Ray and the Low-Energy Gamma-Ray Spectrum to 6 Grams per Square Centimeter over Minneapolis. J. Geophys. Res., vol. 68, no. 4, February 1963, pp. 979-987.
7. Hofmann, D. J.; and Wenckler, J.R.: Simultaneous Balloon Observations at Fort Churchill and Minneapolis during the Solar Cosmic Ray Events of July 1961. J. Geophys. Res., vol. 68, no. 8, April 1963, pp. 2067-2098.
8. Anderson, K. A.: and Milton, D.W.: Balloon Observations of X-rays in the Auroral Zone. J. Geophys. Res., vol. 69, no. 21, November 1964, pp. 4457-4479.

9. Anger, C. D.; Barcus, J. R.; Brown, R. R.; and Evans, D. S.: Auroral Zone X-ray Pulsations in the 1- to 15-Second Period Range. J. Geophys. Res., vol. 68, no. 4, February 1963, pp. 1023-1030.

10. Anderson, K. A.; and Enemark, D. C.: Balloon Observations of X-rays in the Auroral Zone II. J. Geophys. Res., vol. 65, no. 11, November 1960, pp. 3521-3538.

11. Brown, R. R.; Barcus, J. R.; and Parsons, N. R.: Balloon Observations of Auroral Zone X-rays in Conjugate Regions. J. Geophys. Res., vol. 70, no. 11, June 1965, pp. 2599-2612.